Proceedings of the

4TH INTERNATIONAL INTERDISCIPLINARY 3D CONFERENCE

Engineering Section

Pécs, Hungary, October 5-6, 2018

University of Pécs
2018

SZÉCHENYI 2020
HUNGARIAN GOVERNMENT
European Union
European Regional Development Fund
INVESTING IN YOUR FUTURE

Proceedings of the 4th International Interdisciplinary 3D Conference

Engineering Section

Pécs, Hungary, October 5-6, 2018

University of Pécs

The First University in Hungary® 1367

Pécs, 2018

Proceedings of the 4th International Interdisciplinary 3D Conference

Engineering Section

Pécs, Hungary, October 5-6, 2018

Editors
István Ervin Háber, PhD
Csaba Bogdán, András Szőke

ISBN 978-963-429-267-8
This book is available only in digital format

This page is intentionally left blank

Table of Contents

Preface

The 4th International Interdisciplinary 3D Conference is a route leaving event in the series since this is the first time the conference is divided to sections which are held on separate locations. Our Faculty of IT and Engineering of University Pecs is proud to be organizer of the event, while the topic is fully intertwined with our goals. In March of 2018, the 3D Printing Center on the Faculty has been opened and the science of these cutting-edge technologies couldn't be closer to our daily life since then. Researchers, teachers, students can use devices, whose can scan 3D objects, or print their project works with technologies of SLS, polyjet, FDM, etc., which is a great experience especially for students who wants to materialize their final projects or a regular design study of a building or mechanism. These technologies are useful for all disciplines therefore it was also a must to make our projects transparent and show the achievements of this part of science. This is the aim which serves this conference and fair event, where the researchers, developers, makers can show up and change their knowledge, make new contacts.

It was hard during the organization, to fully separate biotechnology from engineering, while the topic of the conference assumes to be around the technologies of 3D visualization, 3D sensing (vision) and 3D printing. These technologies are utilized in engineering which have proved to could used in various parts of medicine, biotechnology since engineering can give and maintain the technical background for researchers from other disciplines. Although the other section biotechnology is only a tight area of medicine, it was hard not to include topics from the border areas. The proof of the closing areas is that a bioengineering curriculum is being developed and accredited in the cooperation of Medical and the Engineering Faculty.

The future plans are to keep up with the organization of the conference, widen the impact of the fair and involve more researchers worldwide.

In the name of the organizers I wish a nice and grateful experience on the conference and exhibition!

Pécs, 10/5/2018

Istvan Ervin Haber

Chief Organizer
Head of the Engineering Department
Institute of Smart Technologies, University of Pecs

4TH INTERNATIONAL INTERDISCIPLINARY 3D CONFERENCE

5TH OF OCTOBER

PROGRAMME OF THE 4TH INTERNATIONAL INTERDISCIPLINARY 3D CONFERENCE

TIME	1ST DAY (OCTOBER 5TH FRIDAY)		
08:00 – 09:30	Registration at the Szentágothai Research Centre		
09:30 – 10:00	Opening Ceremony at the Szentágothai Research Centre		
10:00 – 12:00	Keynote Presentations at the Szentágothai Research Centre		
12:00 – 13:00	Light refreshments at the Szentágothai Research Centre		
13:00 – 13:30	Buses carry the participants to the Faculty of Engineering and Information Technology		
13:30 – 13:45	Opening of the Engineering Section at the Faculty of Engineering and Information Technology		
13:50 – 14:10	**István Ervin Háber, PhD** 3D technologies in practice		
14:10 – 14:30	**István Hatos** *Part and material properties in DMLS/SLM*		
14:30 – 14:50	**Péter Ficzere, PhD** Design questions of the individual medical implants (in Hungarian language)		
14:50 – 15:10	**György Czifra, PhD** *Modern teaching methods in today's engineering education* (in Hungarian language)		
15:10 – 15:20	Coffee break		
	1ST SECTION ROOM	2ND SECTION ROOM	COMPANY STAGE
15:20 – 15:40	**Sándor Bodzás, PhD** *Analysis of the effect of the fillet radius of X-zero gear drives to the normal stress*	**István Ervin Háber, PhD** *Augmented reality in medical applications*	3DZ Franchising Ltd.
15:40 – 16:00	**Zsolt Bodnár, PhD** *Tensile strength analysis of 3d printer filaments*	**András Kriston, PhD** *Segmentation of multiple organs in CT measurements*	Basiliskus 3D Zrt.
16:00 – 16:20	**Katalin Gombos, PhD** *3D Genomics: miRNA expression analysis of spatial cancer organization field*	**Bence Németh, PhD** *Deep learning in medical applications*	eCon Engineering
16:20 – 16:40	**Dávid Csonka** *Renal artery and its surrounding*	**Petra Takács** *Brain Tumor Segmentation in MRI data*	Free Dee Printing Solutions
16:40 – 17:00	**Attila Bölcskei, PhD** *On visuo-spatial skills and their development*	**Balázs Tukora, PhD** *Volume visualization - challenges and tasks*	Varinex Zrt.

4TH INTERNATIONAL INTERDISCIPLINARY 3D CONFERENCE

6TH OF OCTOBER

PROGRAMME OF THE 4TH INTERNATIONAL INTERDISCIPLINARY 3D CONFERENCE

2ND DAY (OCTOBER 6TH SATURDAY)

TIME	1ST SECTION ROOM	COMPANY STAGE
08:30 – 19:00	Breakfast	
09:00 – 09:20	**Máté Deák** *The use of 3D technologies and tools in humanities*	Kvint-R Irodatechnika és 3D Nyomtatási Kft.
09:20 – 09:40	**Csaba Bogdán** *The moiré method and its application in scoliosis*	Hewlett-Packard
09:40 – 10:00	**Gergely Bencsik** *Designing measuring instrument for validation of city simulations*	-
10:00 – 10:20	**Balázs Tukora, PhD** *Automatic shaping of orthopaedic braces using 3D technology*	-
10:30 – 10:50	**Zoltán Meiszterics** *Additive manufacturing of metal component by CMT technology*	Dent-Art-Technik Kft.
10:50 – 11:10	**Géza Várady, PhD** *Optical depth estimation for object recognition and navigation*	-
11:10 – 11:30	**Zoltán Bereczki, PhD** *From parchment to 3D to HTML: the use of the 3D and the Web in architectural history research*	-
11:30 – 11:50	**Zoltán Vízvári** *3D Impedance tomography*	-

POSTER PRESENTATIONS

Gábor Szujó, Máté Farkas, Gábor Somodi
3D geometry editing for numerical modeling based on geosciences data
(in Hungarian language)

Csaba Bogdán
The Moiré Method and its Application in Scoliosis

PERMANENT EXHIBITION OF COMPANIES SPECIALISING IN 3D PRINTING AND VISUALISATION

3DZ

BASILISKUS 3D

DDD MANUFAKTÚRA

DENT-ART-TECHNIK KFT.

ECON ENGINEERING

E-NABLE HUNGARY

FREEDEE PRINTING SOLUTIONS

HERZ FILAMENT

HEWLETT-PACKARD

HONSA KFT.

KVINT-R KFT.

MATERIALISE

PHILAMENT

VARINEX INFORMATIKAI ZRT.

Z ELEKTRONIKA KFT.

Proceedings and Abstracts of the 1st Day (October 5th Friday)

Modern Teaching Methods in Today's Engineering Education

Gy. Czifra[*], B. Varga[+]

[*+]Óbuda University, Donát Bánki Faculty of Mechanical and Safety Engineering

Budapest, Hungary

Keywords: education, engineers, CAD/CAM technology, low cost, open source, modern methods

Abstract

Today, it is crucial for universities and colleges to educate engineers who know the tools and the computer-aided design well-known both in theory and practice. Schools should be encouraged to launch training courses that enable graduates to obtain a competitive degree and later they will stand in the labour market. Designing and manufacturing training courses always have the most modern tools and methods to apply for this. Additionally, modern-minded professionals should be involved in education who are capable and willing to develop and follow technological innovations.

Introduction

To qualify for university and college education to provide appropriate professional knowledge to graduates who can stand up in the labour market. However, the fact that graduates have only basic knowledge gains professional knowledge after being placed in the workplace. Specific professional experience cannot be replaced. That is why the educate for creative thinking is very important. Only then will someone be a successful engineer required by the companies if they have these qualities

The essence for the method

In technical education, it is difficult to keep up with the development of technology, always the most modern computer tools and programs are needed. But what can the instructor do if the school system faces a shortage of resources? Due to possible cuts in higher education it is becoming increasingly difficult to keep pace with technology advances.

It can be a solution to this problem if we are looking for programs that can provide the right technical conditions, but they can be accessed free of charge. Open Source systems have these features. Users were free to access if the registration conditions were accepted. Worth to be used systems if its reliable based on his professional past and the development was continuously.

Not an easy task to selection a CAD/CAM system. The main criterion is to select software that best suits the task to be solved. Our goal is to provide students with the basics of computer design and understand the logic of modern design processes. The other criterion is the practical application.

The following factors should be considered during the selection process:

- Free to use and distribute
- Continuous development and technical support
- Easy to use and user-friendly
- No need for a special computer
- Suitable for 3D modelling and 2D drawing

The following Open Source systems are available on the internet:

FreeCAD:

The program is available in several languages, including Hungarian and English, so learning is simple. In addition to solid modelling and assembly design, there are plenty of other modules in it. Finite element analysis, robot simulation, architectural application is also available to the user. A lot of tutorials also help the user. See this in the following pictures:

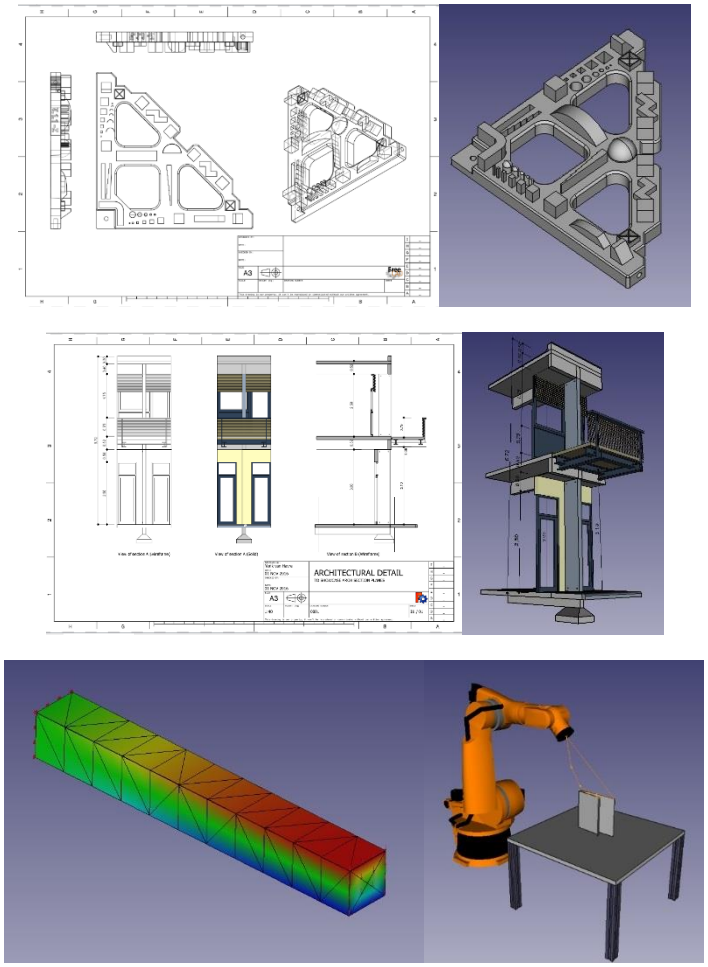

Fig. 1. FreeCAD modules / https://www.freecadweb.org/

LibreCAD:

The program is available in several languages, including Hungarian and English, which makes it easier to learn. It is most like Autodesk AutoCAD. It is primarily suitable for laser cutting and laser engraving, but you can also make 2D drawings with it. It is not very user friendly as the previous program, we cannot find built-in tutorials.

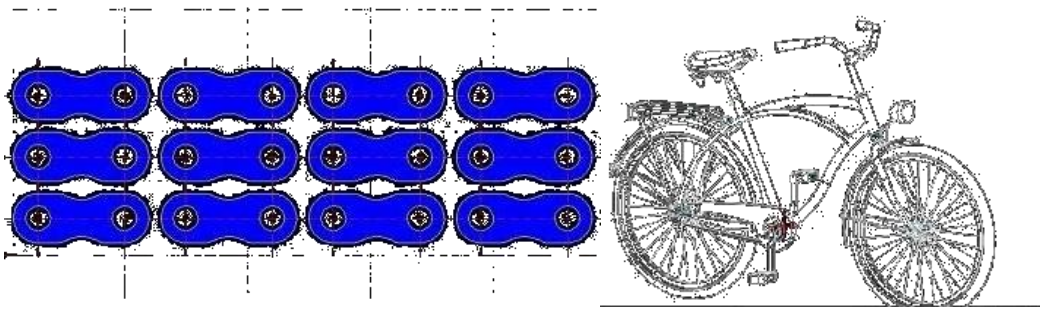

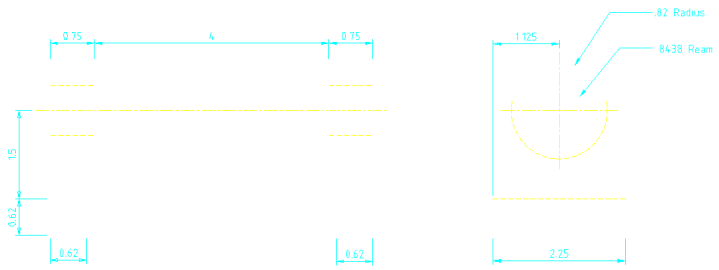

Fig. 2. LibreCAD modules / https://librecad.org/

PowerShape:

This program is available in multiple languages for the user. In addition to solid modelling, we also have the possibility of surface modelling. Creating assembly models is also possible, and we can also find a separate tool design module. The development of the program is continuous, and a new version is published annually. As Autodesk product, its support is also significant.

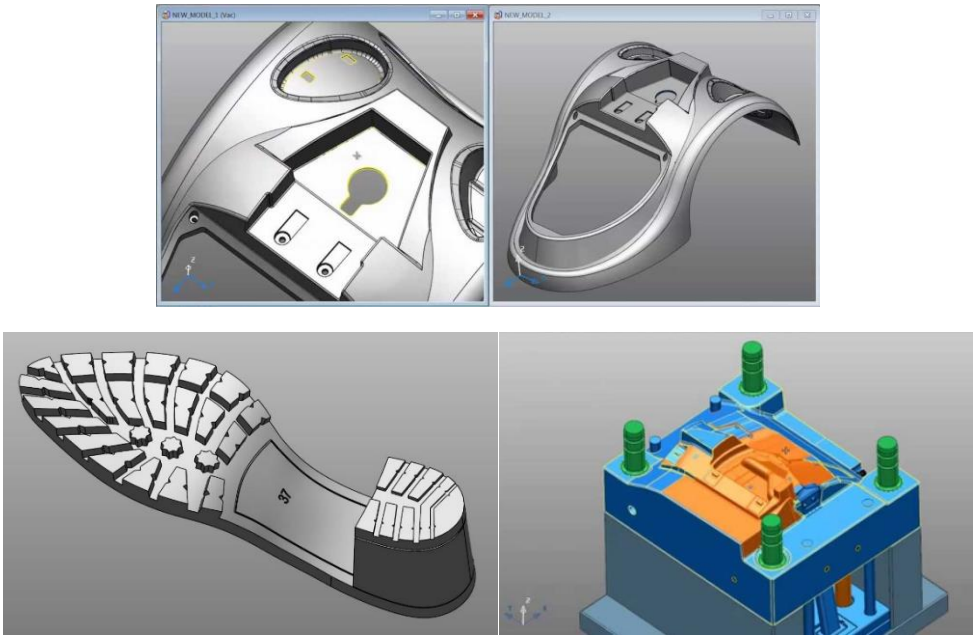

Fig. 3. PowerShape modules / https://www.autodesk.com/products/powershape/overview/

SolveSpace:

The program is in English, but unfortunately it is not available in other languages. Use is a bit difficult. In addition to the solid modelling, assembly modelling and kinematic models can be created with the program.

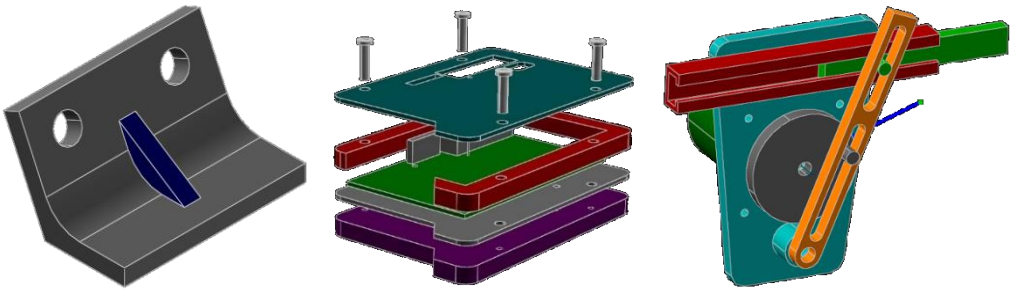

Fig. 4. SolveSpace modules / http://solvespace.com/

In addition to the software described so far, many free CAD programs can be found. The following table contains these softwares:

Table 1. Free CAD softwares

A9 CAD	http://www.a9tech.com/products/a9cad/
Blender	https://www.blender.org/
Draftsight	https://www.solidworks.com/product/draftsight
eCabinet	http://www.ecabinetsystems.com/
gCAD3d	http://www.cadcam.co.at/freiter/gCAD3D_en.htm
Google Sketchup	https://sketchup.google.com/
Fusion 360	https://www.autodesk.com/products/fusion-360/students-teachers-educators
GraphiteOne CAD	https://www.graphiteone-cad.com/
Minos	http://www.le-boite.com/minos.htm
nanoCAD	https://nanocad.com
OnShape	https://www.onshape.com/
Solid Edge Free 2Drafting	http://www.solidedge.com/free2d/
Wings 3D	https://www.wings3d.com/

Among the listed softwares, it is difficult to choose, almost all have the advantages and disadvantages. After examining several options, the PowerShape program proved to be appropriate. All the criteria listed in the beginning of this article are met. In addition to solid state modelling, surface modelling is also available, which is indispensable for the creation of complex geometry bodies. It is also possible to create assembly models and 2D drawings. Free trial is available, user-friendly and support is provided.

It should also be mentioned the software packages that can be used by students, in many instances, by educators - of course, for educational purposes - which are made available by large software vendors. They have a good business sense of policy, because when someone learns in education, they get used to the use of these programs, they can also motivate business users to buy. Just mentioning the biggest ones:

- Creo Free Student Edition
- Autodesk software for students, educators, and educational institutions
- Solid Edge Student Edition
- CATIA V5 STUDENT EDITION

For computer-aided engineering work, we also find software that has an educational version:

- ANSYS Free Student Software Downloads
- MathWorks Store

Like CAD software, we can find CAM software, which are mentioned only as a list. The following table contains:

CAM softwares:

Table 2. Free CAM softwares

Estlcam	http://www.estlcam.com/
Free Mill: 3D Milling from the makers of Visual Mill	http://www.mecsoft.com/freemill.shtml
DeskProto	https://www.deskproto.com/products/free-ed.php
HSMExpress	http://www.hsmworks.com/hsmxpress/
Fustion 360	https://www.autodesk.com/products/fusion-360/students-teachers-educators
G-Simple	https://www.gsimple.eu/
Heeks CAD/CAM	https://www.heeks.net/
PowerMill	https://www.autodesk.com/products/powermill/free-trial

Onshape:

This modern CAD system offers educators and students also to focus only on doing their work better. Unlike other CAD systems, Onshape combines modelling tools and design data management in a secure cloud workspace that is accessible on any device, never loses data and eliminates design gridlock. We have access to true top-down design with configurations, standard content libraries, multi-part modelling and in-context editing. Based on a secure cloud workspace we do not need download updates, installs, license keys, service packs or compatibility issues – we work with the latest version continually. We have possibility to save storing and sharing our CAD data in a secure cloud workspace and we can control and monitor access privileges and see who changed what and when.

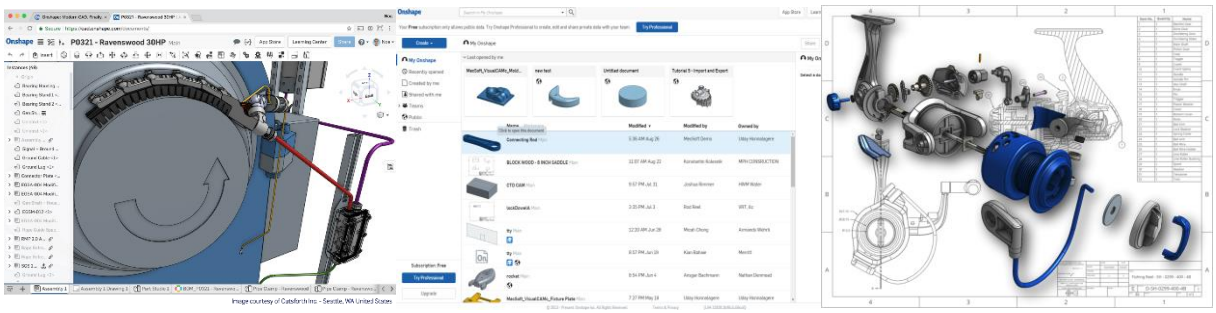

Fig.5. Onshape capabilities / https://www.onshape.com/

Unfortunately, for the purposes of this article we cannot describe in detail all available programs.

Other software packages for supporting the education process:

Open-Sankoré:

The next package, which we used during education, is more closely tied to the teaching methodology. The ***Open-Sankoré*** program is presented very shortly. It's actually a free-use interactive tablet that can be installed on any computer and a powerful interactive tool that effectively supports the teaching process. To use an LCD projector, the efficiency is greatly increased by a touch screen laptop or a Bluetooth enabled tablet. Before the lecture or practice, we can prepare our notes in advance. During the presentation, we can write and draw directly into the document. The notes are automatically saved by the software. The classic wallboard, ceramic table or other board can be completely ignored. The classic wallboard, ceramic board or other board can be completely ignored, because any smooth white surface can be used for display. Use it to avoid lengthy adjustment, calibration, and extremely mobile assistance.

Within the Open-Sankoré program, the operation of any program can be ensured. The program can create a snapshot that can be added to the presentation. It also allows the screening of movies and the use of the browser to support the most up-to-date information in the education process. Manage intuitive, easy to learn. The tablet or the already-mentioned touch-screen laptop - wireless image transmission - allows you to manage from any point in the auditorium, the desired program can be operated. Students with the tablet can be an active participant in the presentation because they can join the work at any moment, comment on the projected curriculum, change it, and even outline the right solution.

The curriculum can be saved in PDF format and given to the students. If the OS is installed on the students' own computer, they can record themselves at home, during repetition. The curriculum can be expanded and important parts can be highlighted.

The figure shows such a " scribbled" performance sheet. Of course, all options in one picture cannot be shown.

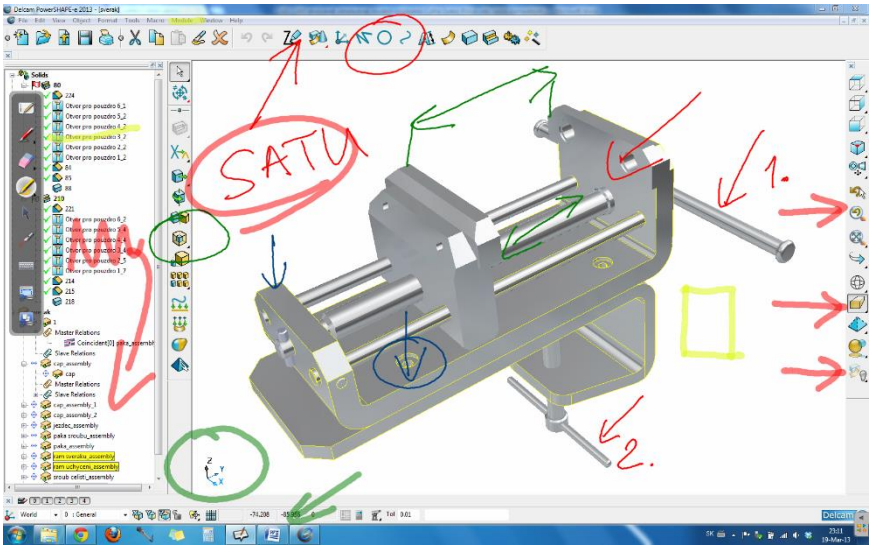

Fig. 6. PowerShape training / *https://www.autodesk.com/products/powershape/overview*

QuestBase:

The natural part of the educational process is accountability. Of course, there is an Open Source application for this task. ***QuestBase*** is the system that is available online from Chrome Web Store. For detailed reasons, this is not possible. Summarizing the gist: Test questions can be created. It can be multiple-choice, open-minded, yes-no-choice questions. A question bank can be created, from which the system generates random questions and answers. Each participant can solve different questions. Based on the experiences, participants select almost exclusively this type of exam.

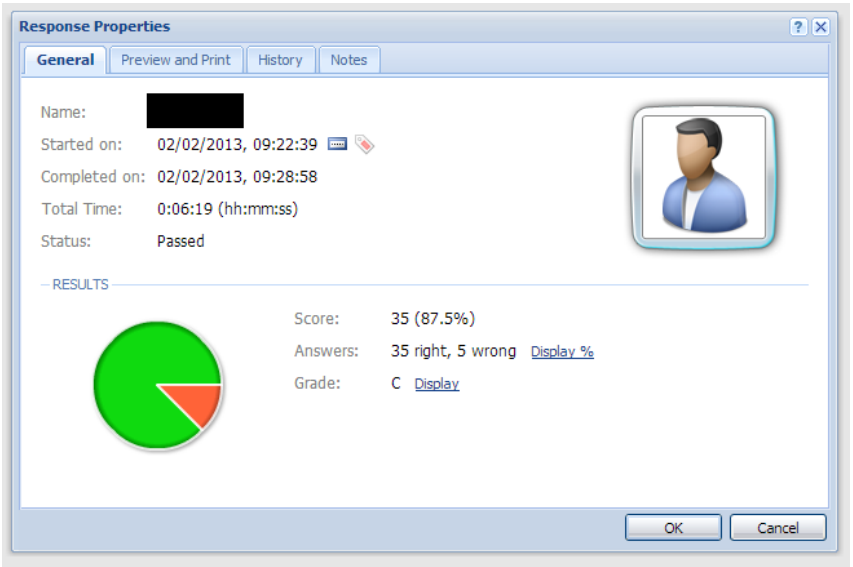

Fig. 7. QuestBase - Evaluation of the test / *http://my.questbase.com/*

Conclusions

If education is lacking in resources, it may still be possible to find a suitable solution to ensure modern conditions. Open Source Systems can provide these conditions. Both CAD and CAM software can be found, but other useful, free options can be found on the web.

REFERENCES

[1] https://www.autodesk.com/products/powershape/overview/, 2018-08-29
[2] http://my.questbase.com/, 2018-08-29
[3] http://open-sankore.org/, 2018-08-29
[4] http://www.estlcam.com/, 2018-08-29
[5] http://www.mecsoft.com/freemill.shtml, 2018-08-29
[6] https://www.deskproto.com/products/free-ed.php, 2018-08-29
[7] http://www.hsmworks.com/hsmxpress/, 2018-08-29
[8] https://www.autodesk.com/products/fusion-360/students-teachers-educators, 2018-08-29
[9] https://www.gsimple.eu/, 2018-08-29
[10] https://www.heeks.net/, 2018-08-29
[11] http://www.a9tech.com/products/a9cad/, 2018-08-29
[12] https://www.blender.org/, 2018-08-29
[13] https://www.solidworks.com/product/draftsight, 2018-08-29
[14] http://www.ecabinetsystems.com/, 2018-08-29
[15] http://www.cadcam.co.at/freiter/gCAD3D_en.htm, 2018-08-29
[16] https://sketchup.google.com/, 2018-08-29
[17] https://www.graphiteone-cad.com/, 2018-08-29
[18] http://www.le-boite.com/minos.htm, 2018-08-29
[19] https://nanocad.com, 2018-08-29
[20] https://www.onshape.com/, 2018-08-29
[21] http://www.solidedge.com/free2d/, 2018-08-29
[22] https://www.wings3d.com/, 2018-08-29
[23] https://www.autodesk.com/products/powermill/free-trial, 2018-08-30
[24] http://solvespace.com/, 2018-08-30
[25] https://www.freecadweb.org/, 2018-08-30

Analysis of the Modification of the Fillet Radius of X-Zero Gear Drives to the TCA Parameters

Sándor Bodzás, PhD
University of Debrecen, Department of Mechanical Engineering, Debrecen, Hungary

Keywords: fillet radius, TCA, CAD, normal stress, deformation, elastic strain, gear

Abstract: The aim of the publication is the analysis of the normal stress, normal deformation and normal elastic strain of the fillet radiuses of x-zero gear drives. For this TCA (Tooth Contact Analysis) analysis the designing and preparing of the CAD (Computer Aided Design) models of the gear drives are necessary. Because of the reduction of the calculations a computer aided software will be able to develop. Based on the received TCA results the function of the fillet radius values and the mechanical parameters could be determined. These analyses are important for finding of the appropriate geometry of the x-zero gear drive for a given load.

Introduction

The aim of the Tooth Contact Analysis (TCA) is the analysis of the connection zone of the different gears based on something mechanical characteristic [7, 8, 9, 14]. Based on the TCA results the geometry of the gear pairs could be optimized. The gear designing, manufacturing and measuring processes are very huge and complex tasks [2, 3, 4, 5, 6, 10, 12, 13]. The TCA analyses are belonged to the gear designing process (Fig. 1) [7, 8, 9].

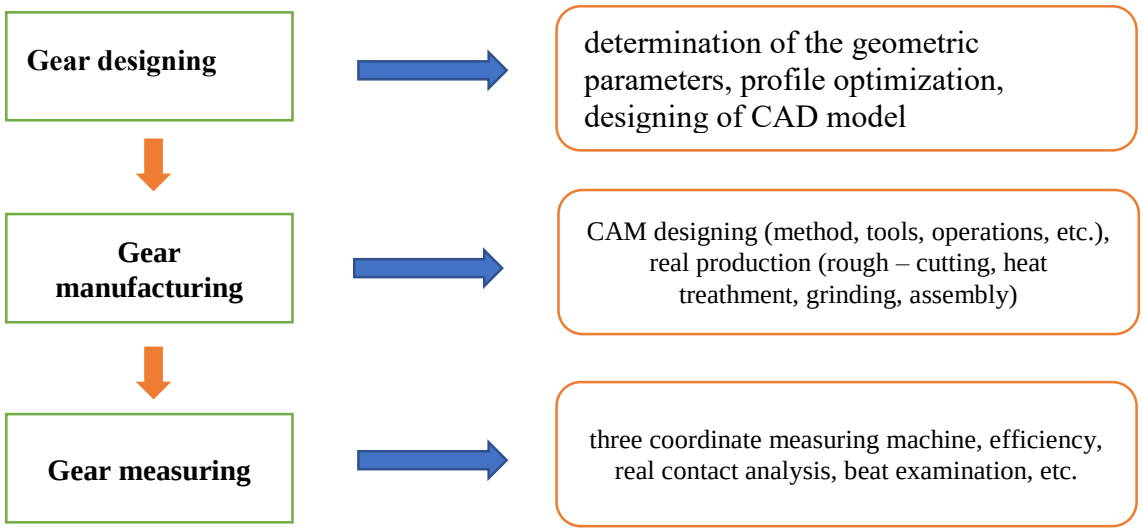

Fig. 1. Gear manufacturing process

The X – zero gear drive is an extreme case of the X – gear drive, when addendum modification is not used. That is why the tooth connection is on the pitch circles. These circles are the rolling circles [5, 6, 12, 13].

1. Adoption of the fillet radius of the gear pairs

Selection of the appropriate fillet radius is important in aspect of load and avoidance of the tooth break. Based on the geometric calculations the root circle diameter (d_f) and the evolvent base circle (d_{ak}) diameter are [12, 13]:

$$d_{f1,f2} = d_{1,2} - 2 \cdot h_f = \left(z_{1,2} - 2 - 2 \cdot c^*\right) \cdot m \qquad (1)$$

$$d_{ak1,ak2} = d_{1,2} \cdot \cos\alpha_0 \tag{2}$$

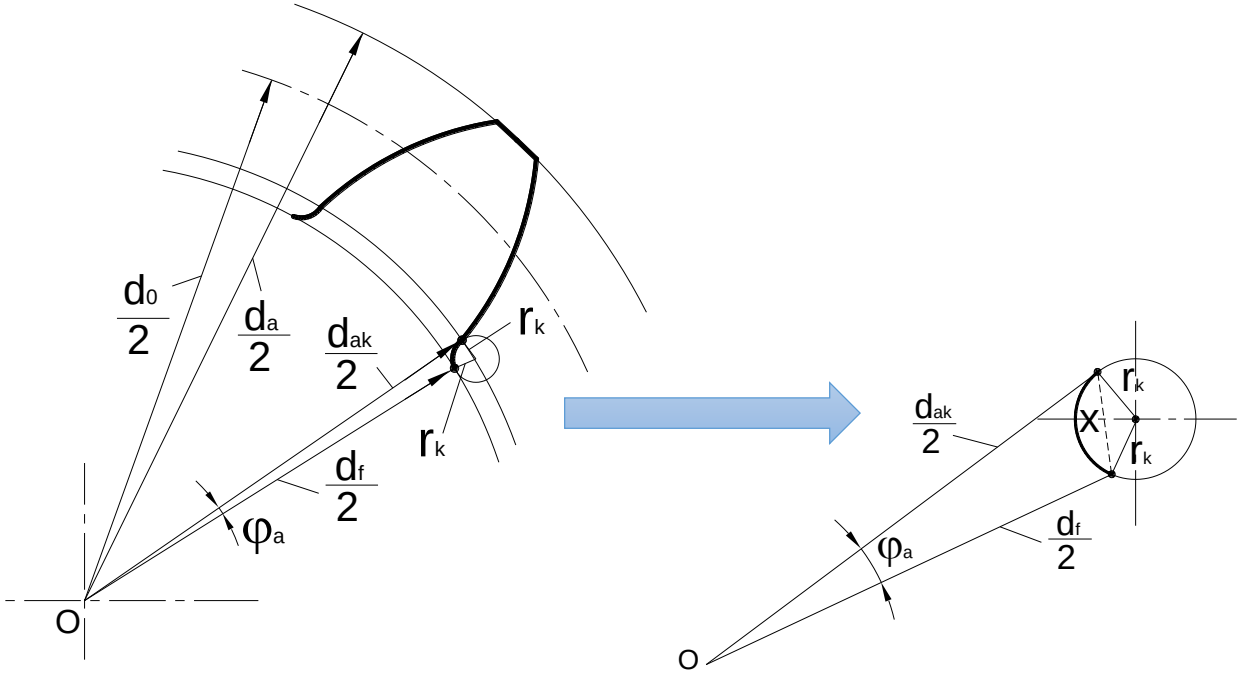

Fig. 2. Determination of the fillet radius of the gear

Beside on the constancy of the φ_a radius angle the necessary r_k fillet radius could be determined by the solution of the following equations by numerical way (Fig. 2):

$$\left.\begin{aligned} x &= \sqrt{\left(\frac{d_f^2}{2}\right) + \left(\frac{d_{ak}^2}{2}\right) - \frac{d_f \cdot d_{ak}}{2} \cdot cos\varphi_a} && (3)\\ \frac{x \cdot \sqrt{r_k^2 - \left(\frac{x}{2}\right)^2}}{2} &= \sqrt{s \cdot (s - r_k)^2 \cdot (s - x)} && (4)\\ s &= \frac{2 \cdot r_k + x}{2} && (5) \end{aligned}\right\}$$

2. Designing of the gear pairs

Knowing of the expressions of the gear parameters a computer aided software could be developed [1, 2, 12, 13]. The input parameters of the program are the *m* module and the z_1, z_2 number of teeth. The main dimensions of the gear drive (centre distance, main circles, etc.) are calculated and the toothed gears are drawn on the screen by the program (Fig. 3). The profile points of the toothed gear could be saved into *txt* format and imported into 3D SolidWorks designing software. Interpolating B spline surface is set on the received profile points. Body element is created from the received evolvent tooth profile by extrude. It is modelled along the perimeter of the given circle based on the gear number of teeth (Fig. 4).

Five types of x-zero gear drives are designed. All parameters of these drives are the equable excluding the fillet radius of the driven gear (Table 1). The object of the analysis is the changing fillet radius of the driven gear.

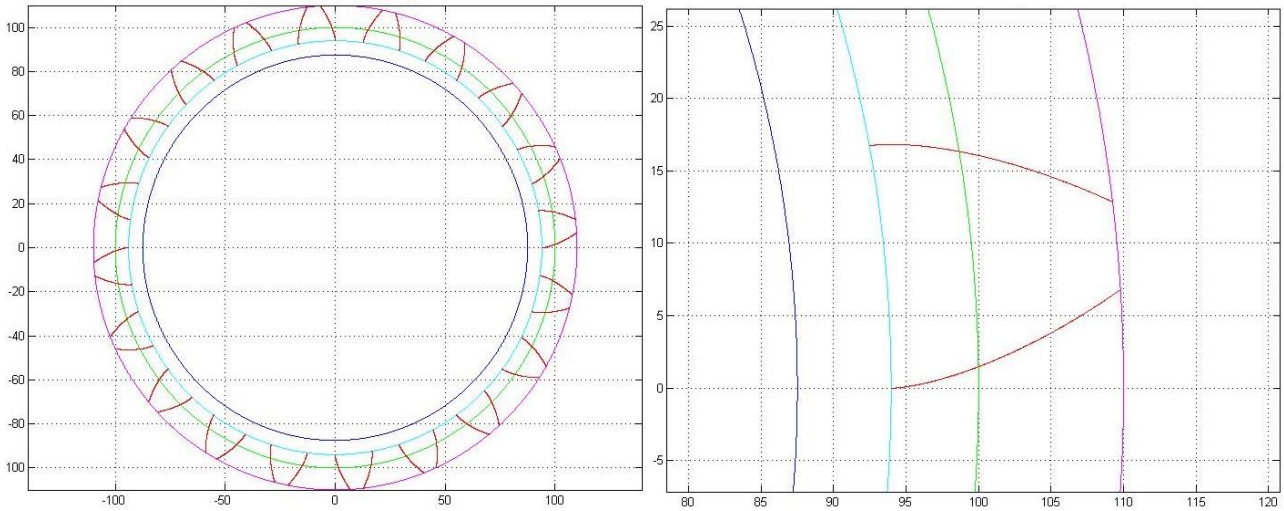

a) generation of the driving gear

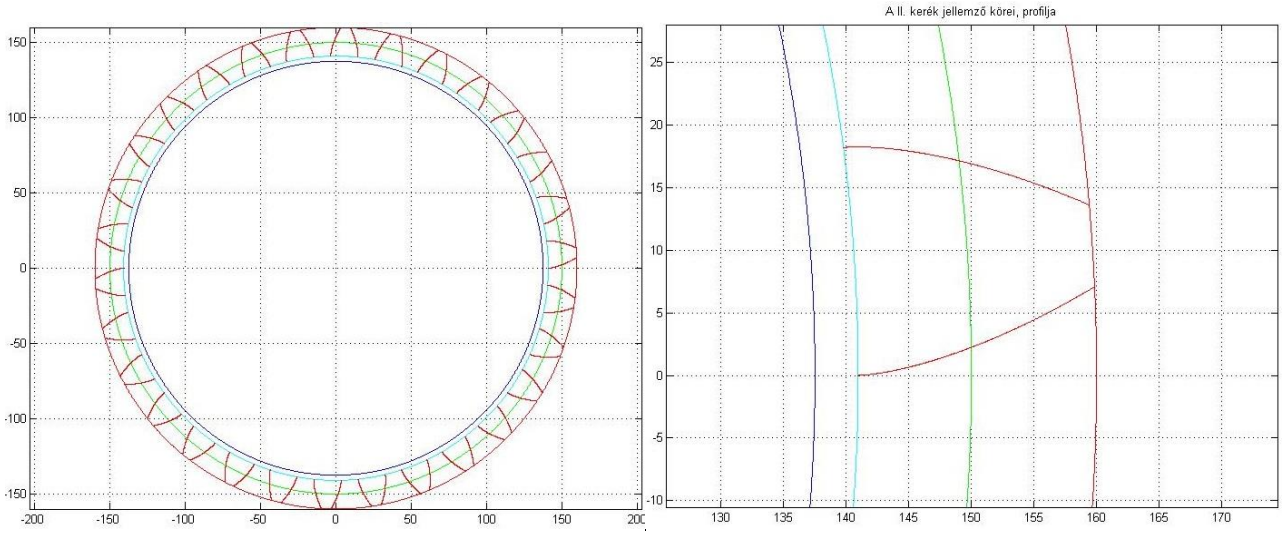

b) generation of the driven gear

Fig. 3. Generation of a concrete geometric X – zero gear drive

Table 1. The calculated gear parameters

Parameters		**Parameters**	
Axial module (m) [mm]	10	**Circular pitch (t_0)** [mm]	31.415
Number of tooth of the driving gear (z_1)	20	**Backlash (j_s)** [mm]	1.57
Number of tooth of the driven gear (z_2)	30	**Whole depth (h)** [mm]	22.5
Centre distance (a_0) [mm]	250	**Working depth (h_w)** [mm]	20
Addendum (h_a) [mm]	10	**Tooth thickness (S_{ax1})** [mm]	14.922
Dedendum (h_f) [mm]	12	**Pitch circle diameter of the driving gear (d_1)** [mm]	200
Bottom clearance (c) [mm]	2.5	**Pitch circle diameter of the driven gear (d_2)** [mm]	300

Tip circle diameter of the driving gear (d_{a1}) [mm]	220	**Tip circle diameter of the driven gear (d_{a2})** [mm]	320
Root circle diameter of the driving gear (d_{f1}) [mm]	175	**Root circle diameter of the driven gear (d_{f2})** [mm]	275
Basic circle diameter of the driving gear (d_{ak1}) [mm]	187.938	**Basic circle diameter of the driven gear (d_{ak2})** [mm]	281.907
Transmission ratio (i)	1.5	**Base profile angle (α_0)** [°]	20

The fillet radius of the driving gear is selected for 7 mm. The fillet radiuses of the driven gear are selected for 4 mm, 5 mm, 6 mm, 7 mm and 8 mm.

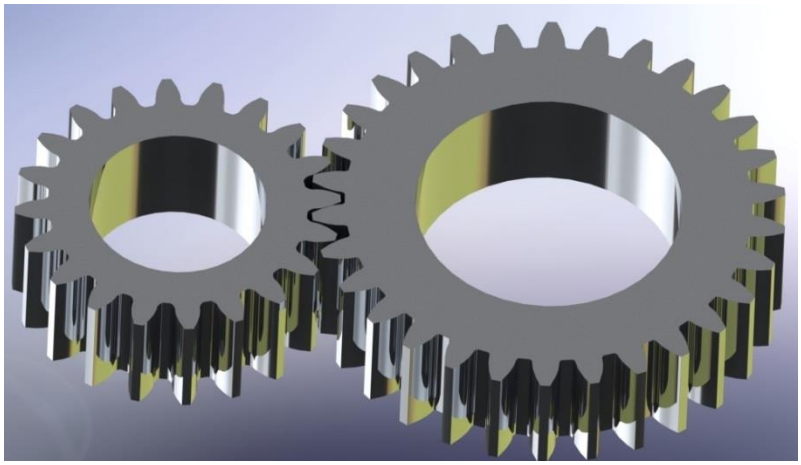

Fig. 4. 3-dimensional CAD model of the designed gear drive by SolidWorks software

3. TCA analysis of the fillet of the driven gear in case of tooth connection

For the analysis of the contact points, Ansys R18.0 Finite Element Modeling (FEM) software was used. In the tooth contact zone, 0.15 frictional factor was applied.

During the calculations tetrahedron meshing was applied on the face surfaces, while tooth lengths were divided into 40 equal parts. The density of the meshing was automatic outside the tooth contact zone. Inside the tooth root 0.5 mm density meshing was applied (Fig. 5).

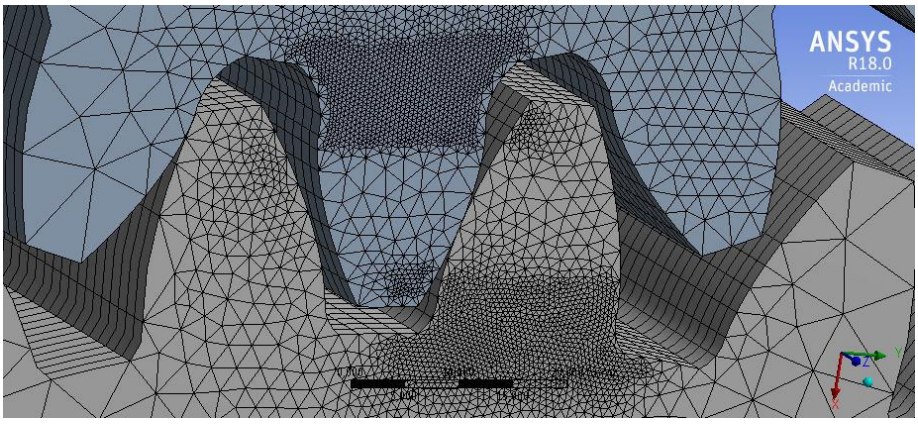

Fig. 5. Application of the mesh of FEM

During the analysis, the material of the drive pairs was structural steel (Table 2). The driven cog wheel having different fillet radius was loaded by 700 Nm torque.

Table 2. Parameters of the material

Density	7850 kg/m^3
Yield limit	250 MPa
Ultimate strength	460 MPa

Five degrees of freedom of the driving spur gear were fixed. Only the rotational movement around the rotational shaft was allowed. In case of the driven cog wheel fixed support was applied. During this analysis all parameters of the gears are equable only the fillet radius of the driven gear are changed. The normal stress distribution of the driving and the driven gears are analyzed on four radiuses (1, 2 on the driven gear and 3,4 on the driving gear) of every gear pair (Fig. 6, 7 and 8).

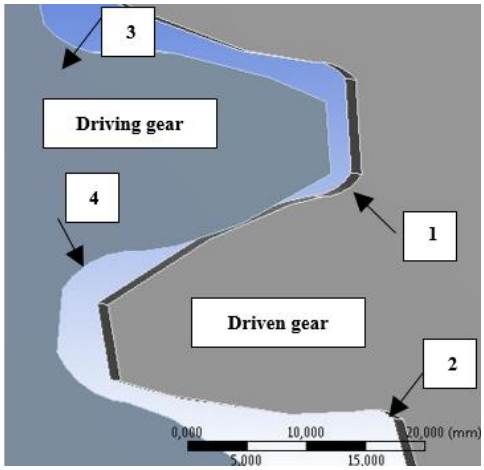

Fig. 6. Nominations of the fillet radiuses

Fillet radius	**1. tooth root**	**2. tooth root**
R4	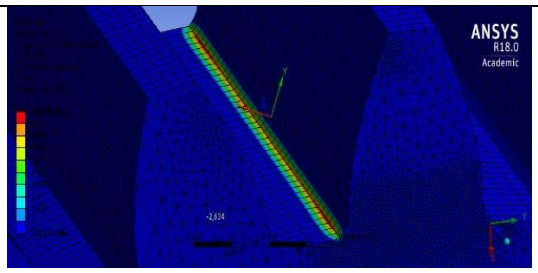	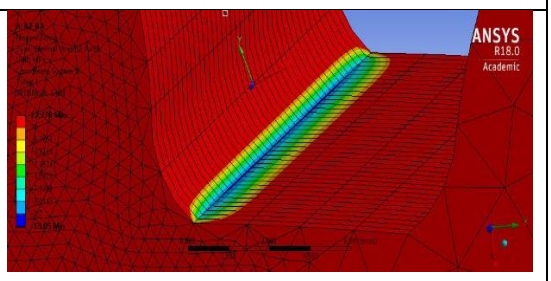
R5	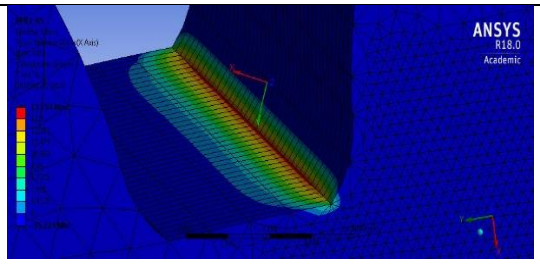	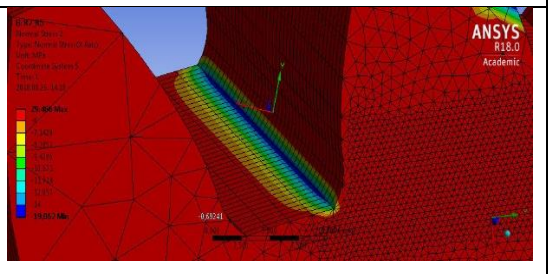

R6	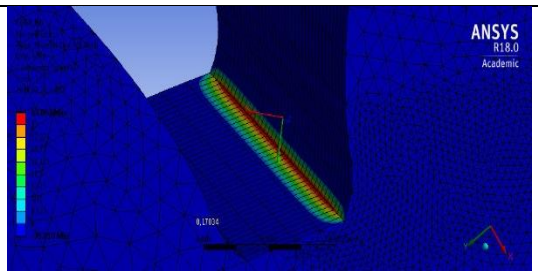	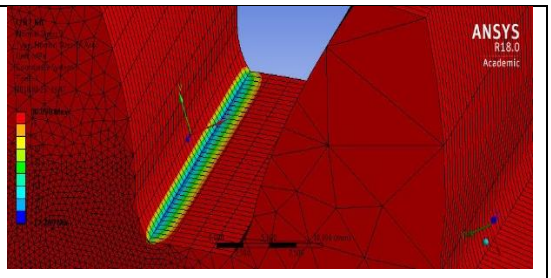
R7	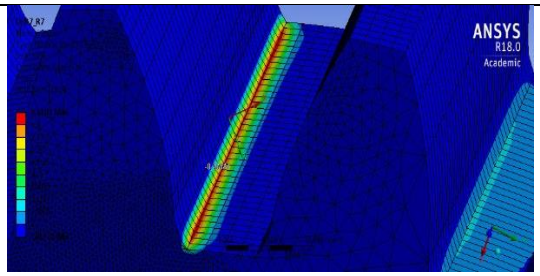	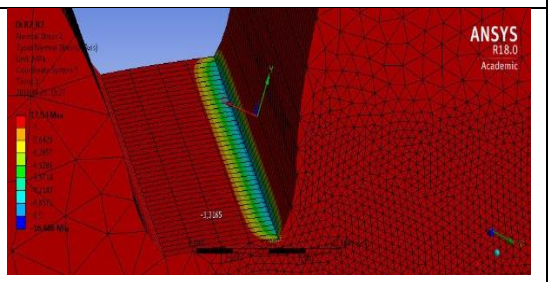
R8	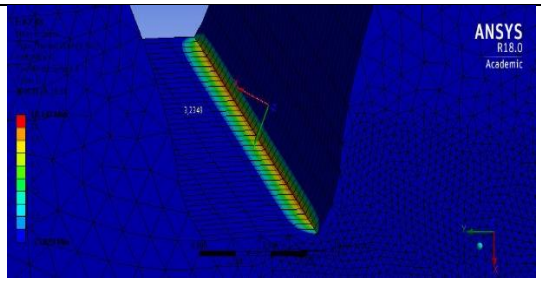	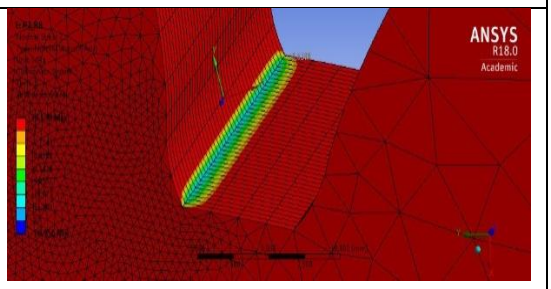

Fig. 7. Normal stress distribution on the 1 and 2 fillet radius of the driven gear

Fillet radius	**3. tooth root**	**4. tooth root**
R4	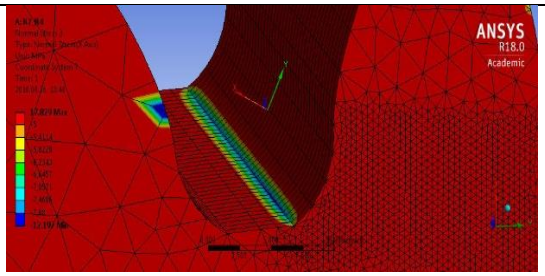	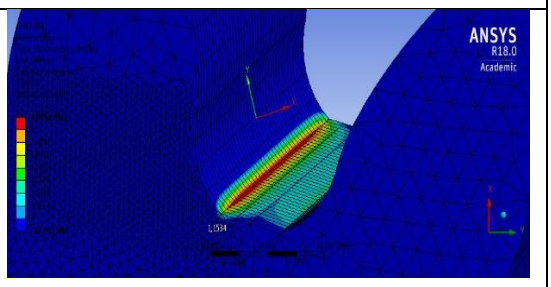
R5	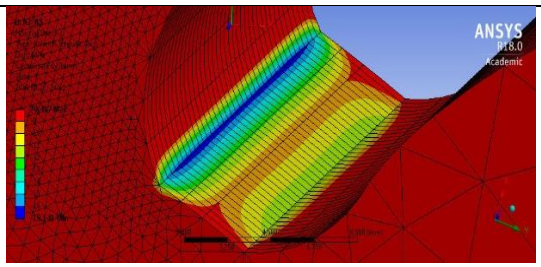	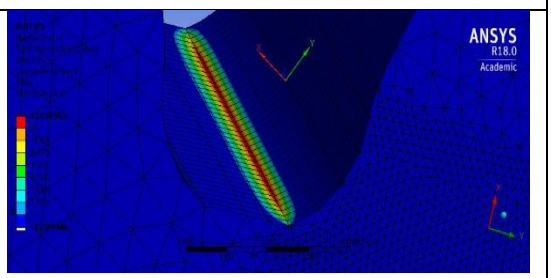

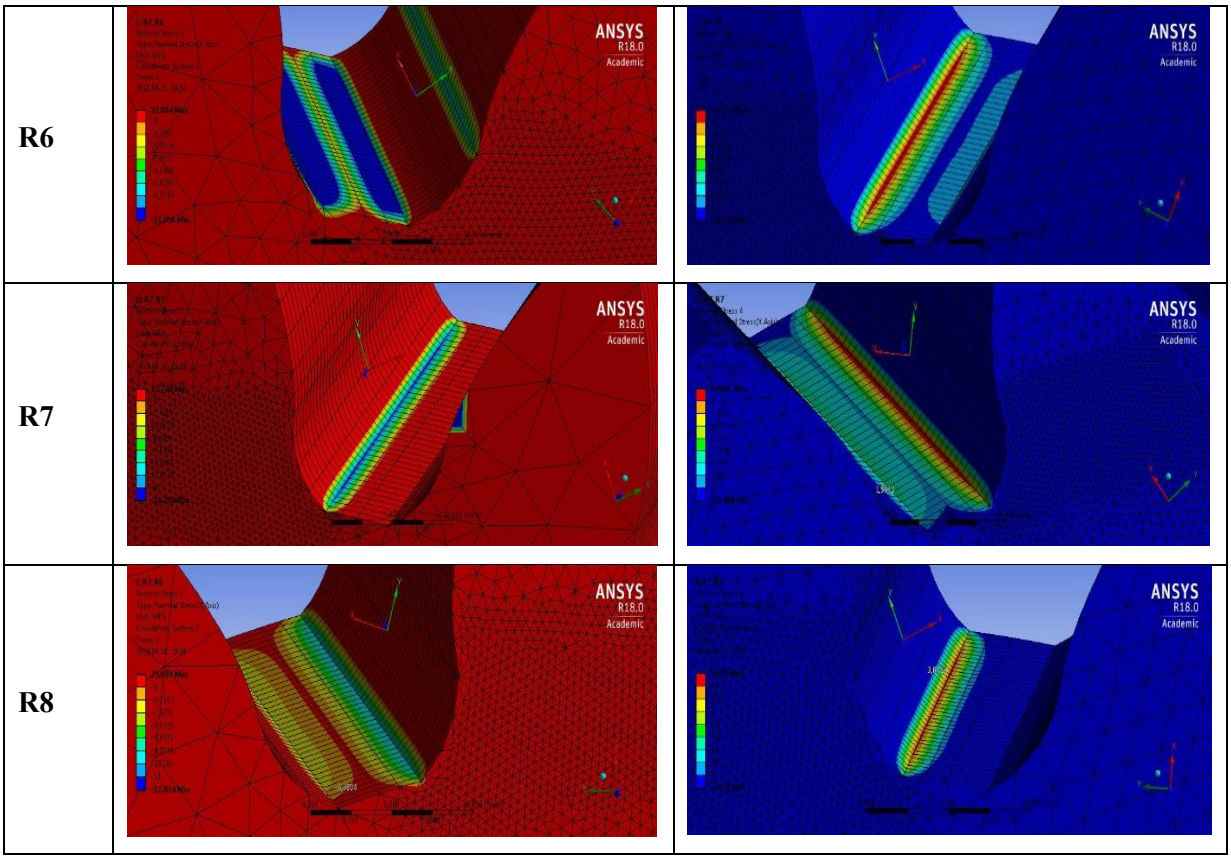

Fig. 8. Normal stress distribution on the 3 and 4 fillet radiuses of the driving gear

4. TCA analysis of the fillet of the driven gear in case of avoidance of the tooth break

In case of straight spur gear one tooth is functional as a supporter. It is loaded by F_n force which is perpendicular for the surface. Assuming planar stress condition the stress condition of the tooth root could be determined. The loads are compression, bending and shear [7, 8, 11, 13, 14, 15].

According to the experiences the highest stresses are developed on the A and B points of the tooth root. The stresses of these points are [13]:

$$\left.\begin{aligned} \sigma_A &= \sigma_{b1} - \sigma_{b2} - \sigma_s \\ -\sigma_B &= \sigma_{b1} - \sigma_{b2} + \sigma_s \end{aligned}\right\} \quad (6), (7)$$

Only one tooth pair is connected on Fig. 9. The root stress is the highest if the F_n force is situated on the tip circle of the gear [13].

$$\sigma_{b1} = \frac{6 \cdot l_1 \cdot F_n \cdot cos\alpha_0}{b \cdot v_a^2} \quad (8)$$

$$\sigma_{b2} = \frac{6 \cdot l_2 \cdot F_n \cdot sin\alpha_0}{b \cdot v_a^2} \quad (9)$$

$$\sigma_s = \frac{F_n \cdot sin\alpha_0}{b \cdot v_a} \quad (10)$$

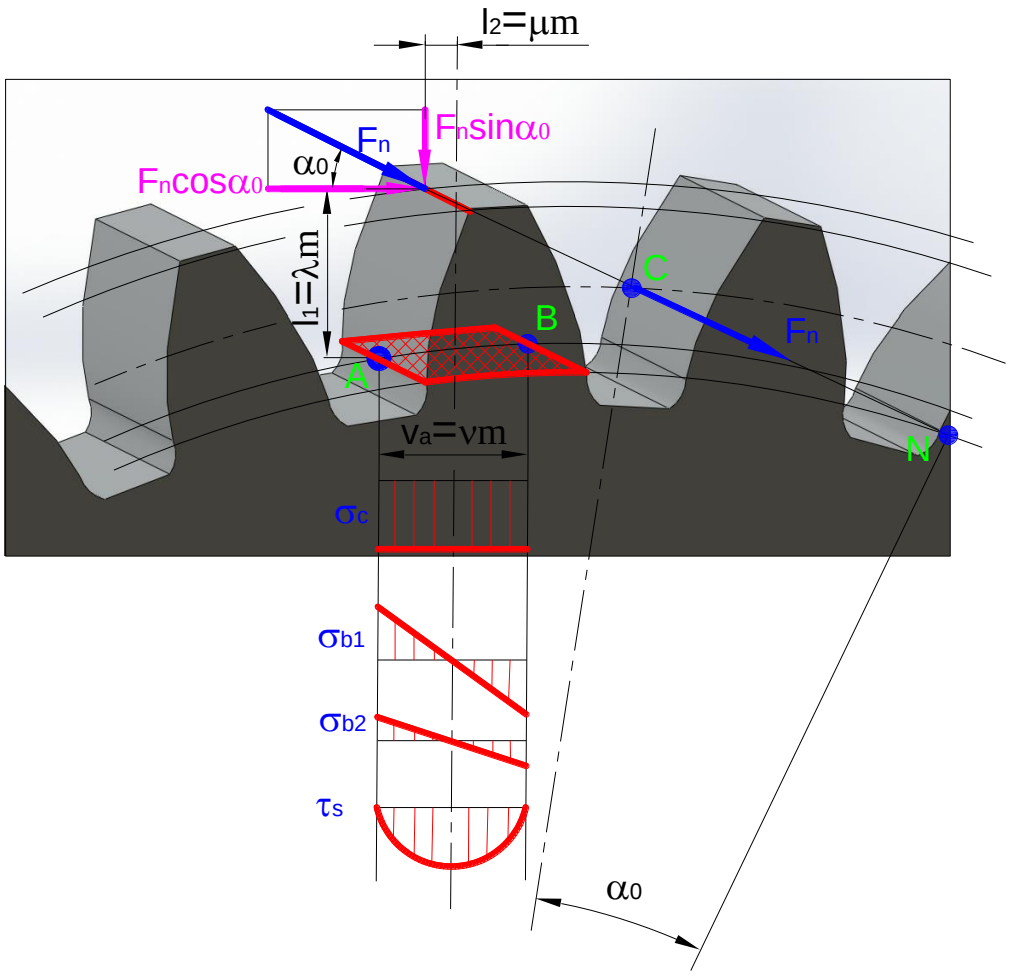

Fig. 9. Calculation of the tooth bending load

The l_1, l_2, v_a dimensions are expressed and substituted by the m module [13]

$$\sigma_A = \frac{F_n}{b \cdot m}\left(\frac{6 \cdot \lambda \cdot \cos\alpha_0}{\vartheta^2} - \frac{6 \cdot \mu \cdot \cos\alpha_0}{\vartheta^2} - \frac{\sin\alpha_0}{\vartheta}\right) \quad (11)$$

$$-\sigma_B = \frac{F_n}{b \cdot m}\left(\frac{6 \cdot \lambda \cdot \cos\alpha_0}{\vartheta^2} - \frac{6 \cdot \mu \cdot \cos\alpha_0}{\vartheta^2} + \frac{\sin\alpha_0}{\vartheta}\right) \quad (12)$$

In this analysis all degrees of freedom of the driven spur gear were fixed. During this analysis all parameters of the driven gears are equable only the fillet radius of the driven gear are changed. The normal stresses, normal elastic strains and the normal deformations in different direction (x and y) of the driven gears are analyzed on two radiuses (Fig. 10). The coordinate system is adopted on the middle of one tooth on the root circle.

In the tooth contact zone, 0.15 frictional factor was applied. During the calculations tetrahedron meshing was applied on the face surfaces, while tooth lengths were divided into 30 equal parts. The density of the meshing was automatic outside the analyzed tooth. Inside the analyzed tooth 0.5 mm density meshing was applied (Fig. 11).

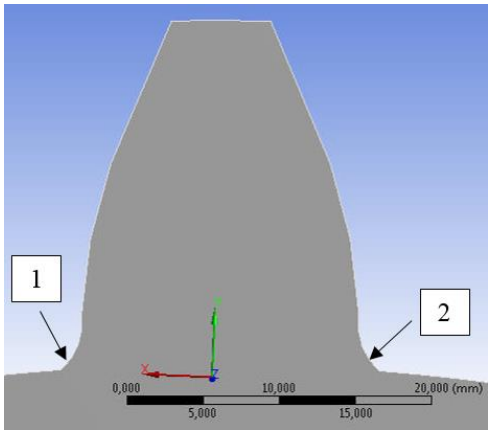

Fig. 10. Nominations of the fillet radiuses and the adoption of the coordinate system

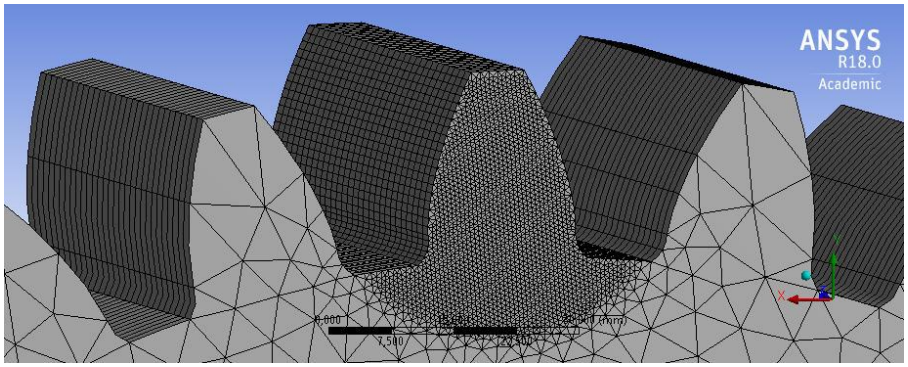

Fig. 11. Application of the mesh of FEM

During the analysis, the material of the drive pairs was structural steel (Table 2). The driven cog wheel having different fillet radius was loaded by 300 N force on the tip edge (Fig. 9).

4.1. Analyses of the normal stress on different directions

According to the coordinate system arrangement the normal stresses of the fillet radiuses are analyzed *x* and *y* directions. The *z* direction is perpendicular for the area of the tooth root (Fig. 9).

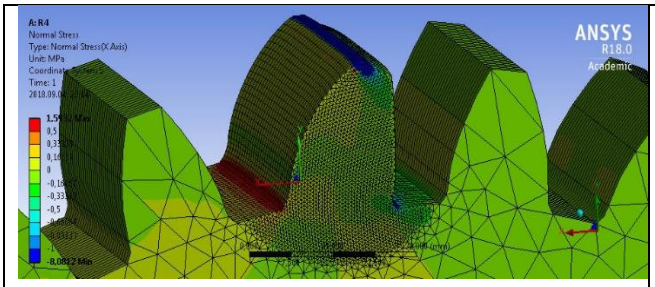	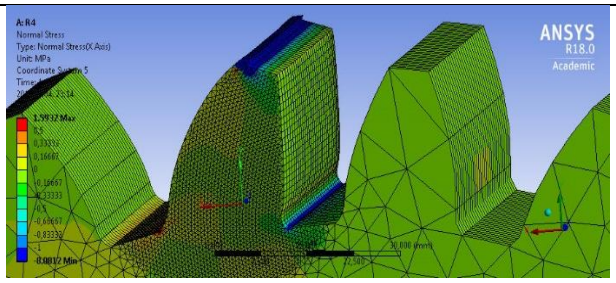
x direction 1. tooth root	*x* direction 2. tooth root

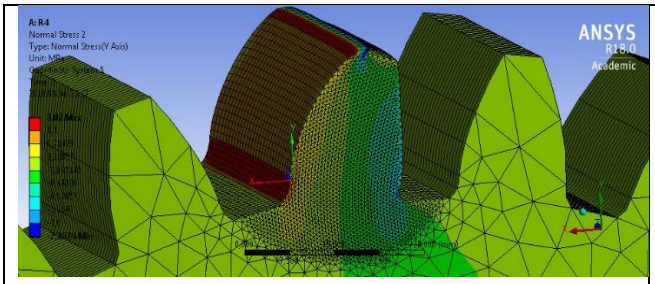	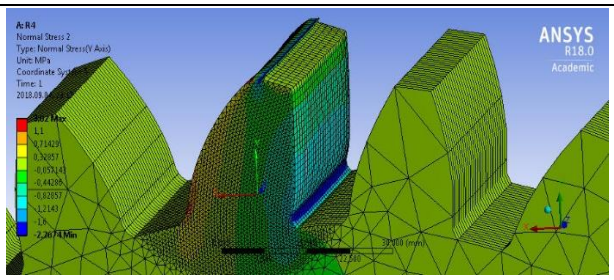
y direction 1. tooth root	*y* direction 2. tooth root
Fillet radius: R4	
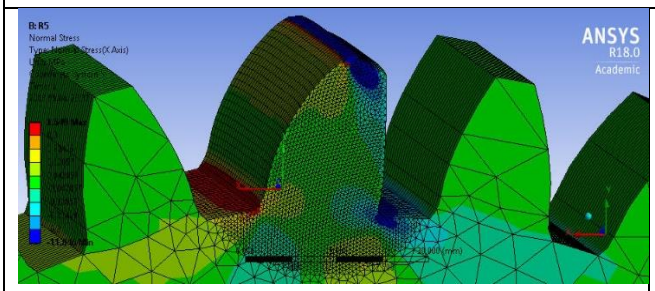	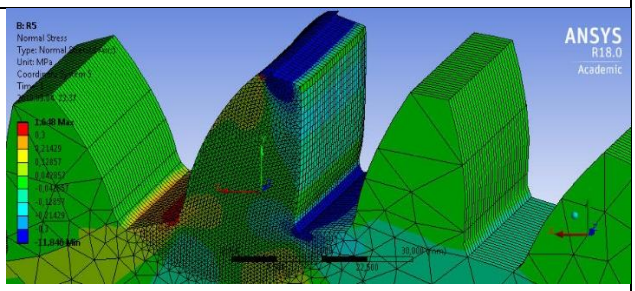
x direction 1. tooth root	*x* direction 2. tooth root
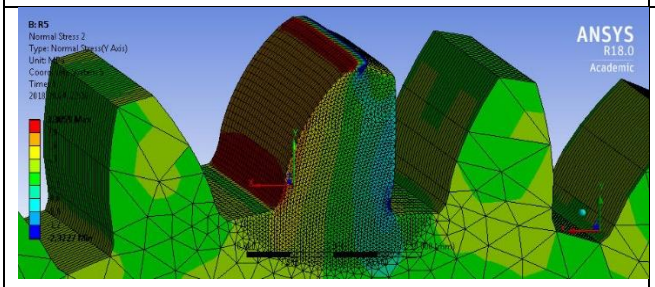	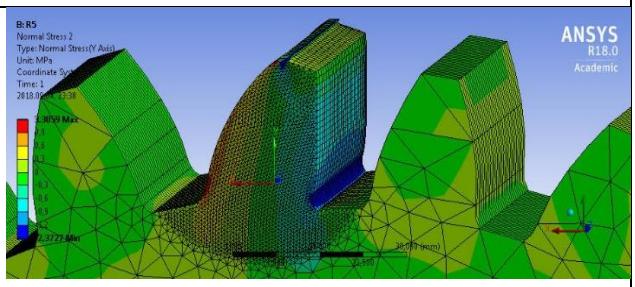
y direction 1. tooth root	*y* direction 2. tooth root
Fillet radius: R5	
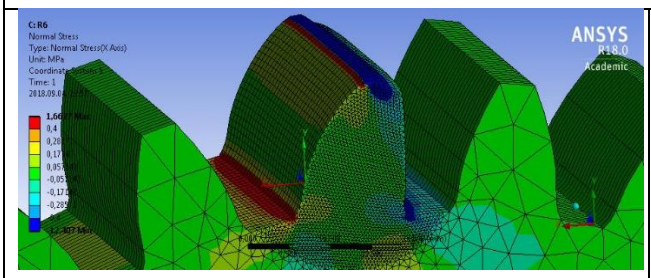	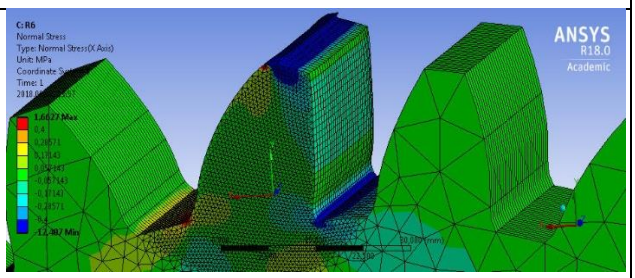
x direction 1. tooth root	*x* direction 2. tooth root
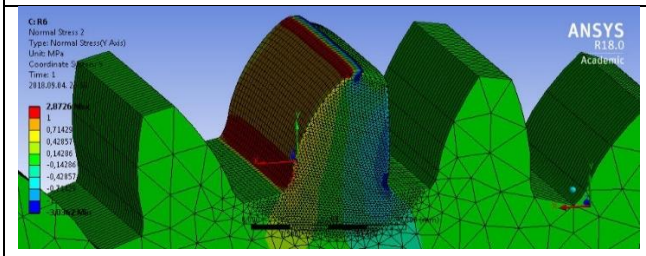	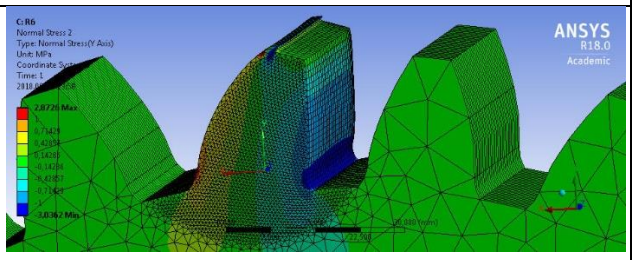
y direction 1. tooth root	*y* direction 2. tooth root
Fillet radius: R6	

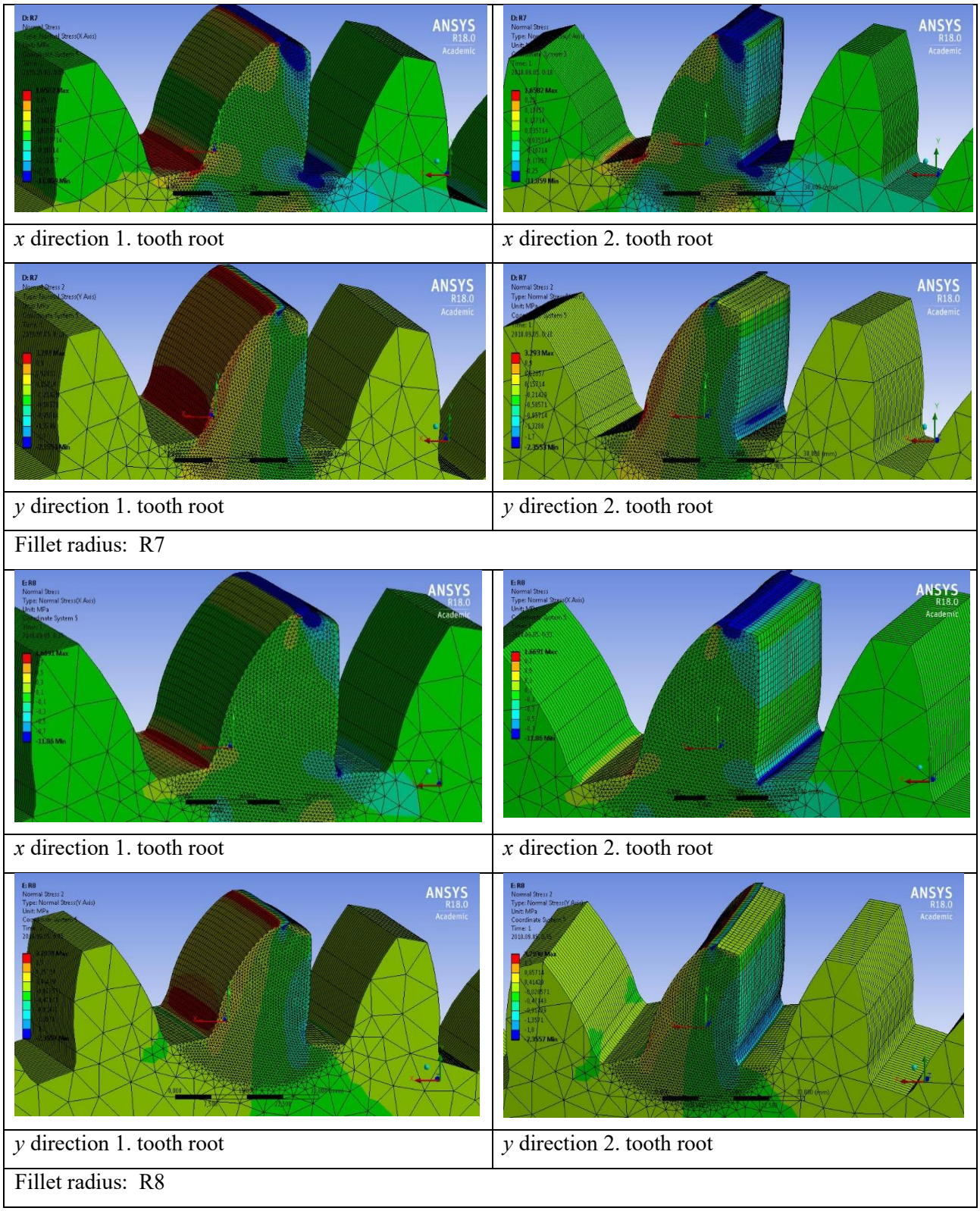

Fig. 12. Normal stress distribution on the 1 and 2 fillet radius of the driven gear

Based on the TCA results the average normal stress values are calculated in different directions on the fillet radiuses (Fig. 12).

In case of the 1. tooth root it could be determinable that the average normal stresses are increased on the *x* direction in the function of the increasing of the fillet radius. The average normal stresses are decreased on the *y* direction in the function of the increasing of the fillet radius (Fig. 13).

In case of the 2. tooth root it could be determinable that the average normal stresses are increased on the *x* direction in the function of the increasing of the fillet radius. The average normal stress are increased on the *y* direction in the function of the increasing of the fillet radius (Fig. 13).

The *x* directional and *y* directional normal stresses of the 1. tooth root are higher than the normal stresses of the 2. tooth root in absolute value (Fig. 13).

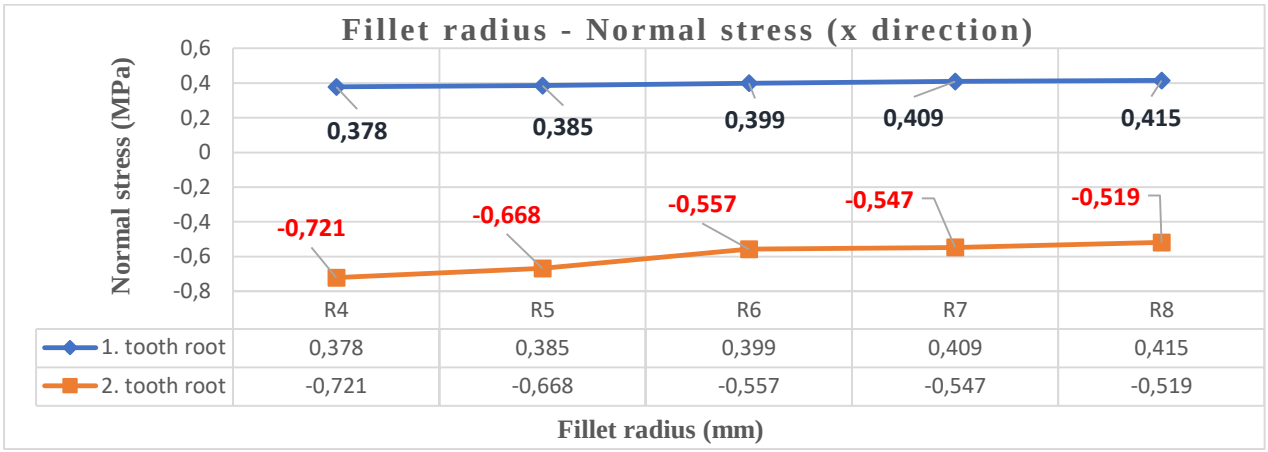

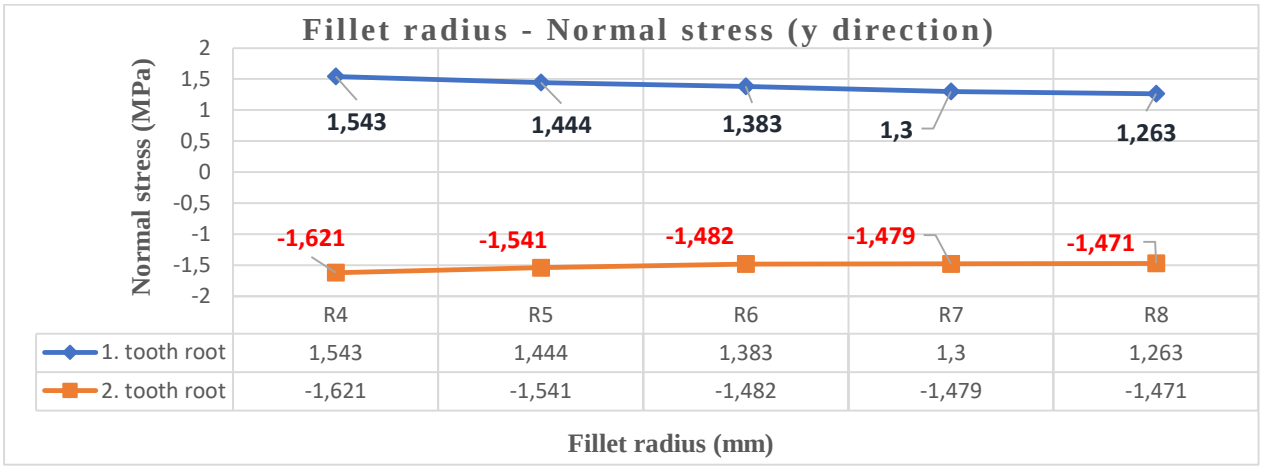

Fig. 13. The normal stress results in the function of the fillet radius of the driven gear

4.2. Analyses of the normal deformations on different directions

According to the coordinate system arrangement the normal deformations of the fillet radiuses are analyzed on x and y directions (Fig. 14).

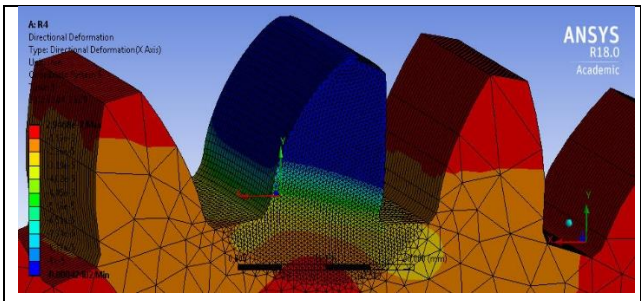	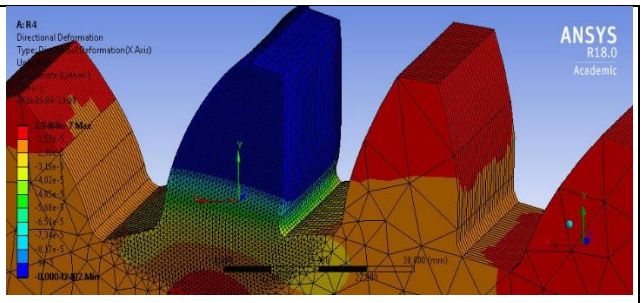
x direction 1. tooth root	*x* direction 2. tooth root
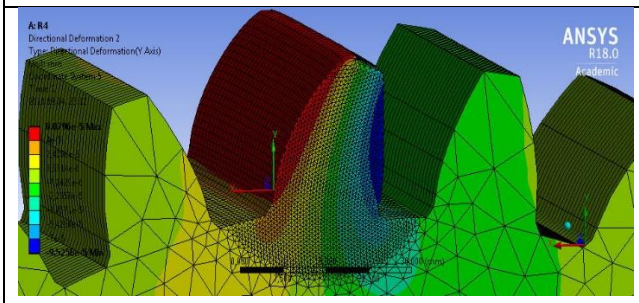	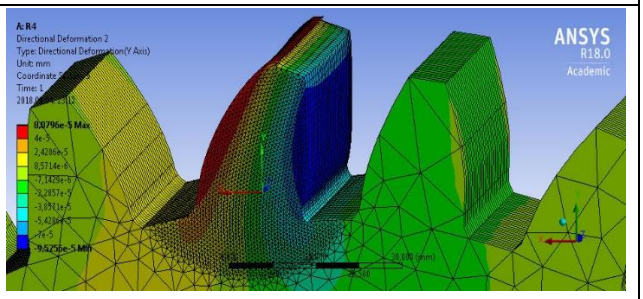
y direction 1. tooth root	*y* direction 2. tooth root
Fillet radius: R4	
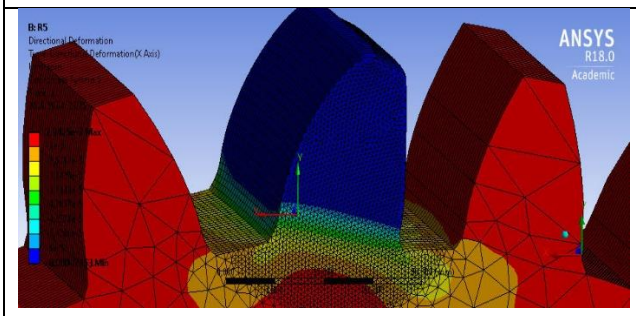	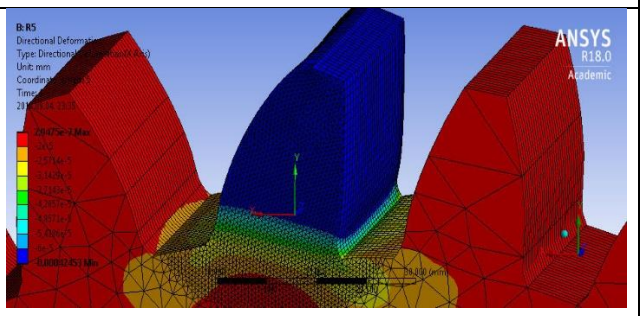
x direction 1. tooth root	*x* direction 2. tooth root
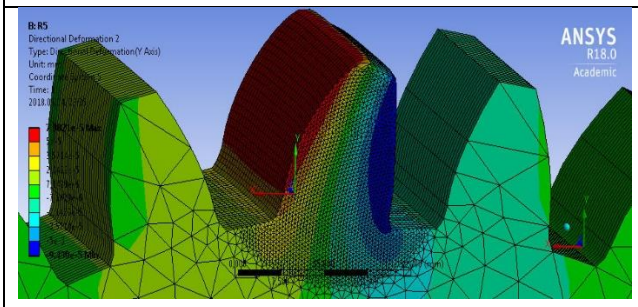	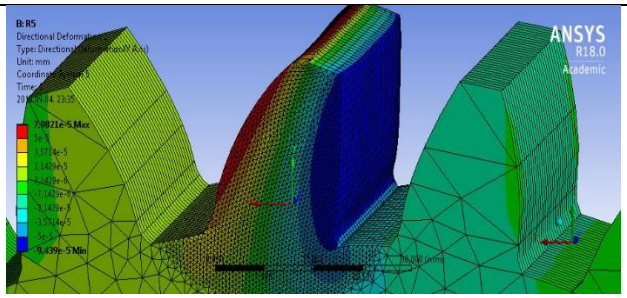
y direction 1. tooth root	*y* direction 2. tooth root
Fillet radius: R5	
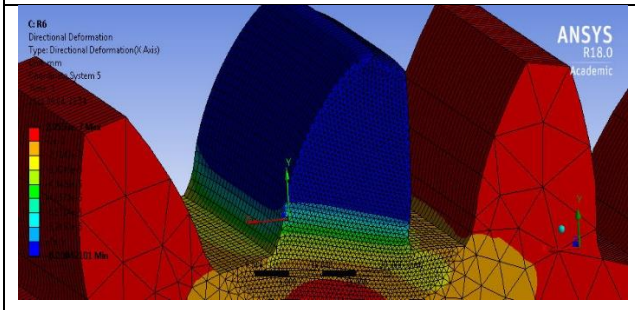	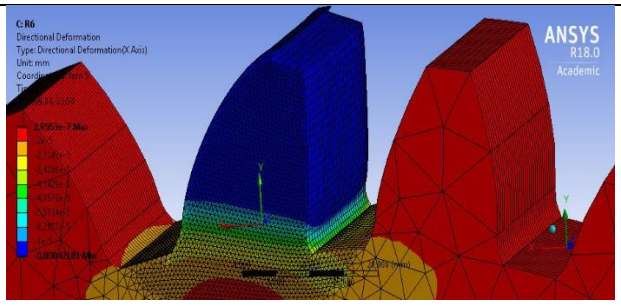

x direction 1. tooth root	*x* direction 2. tooth root
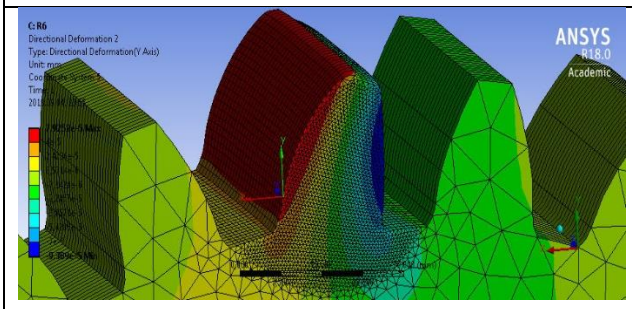	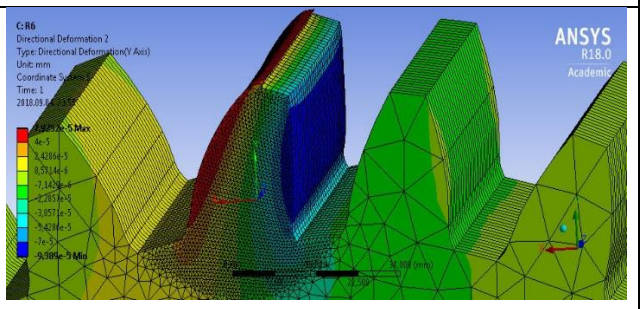
y direction 1. tooth root	*y* direction 2. tooth root
Fillet radius: R6	
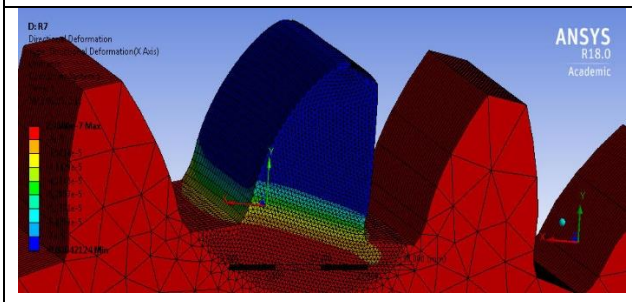	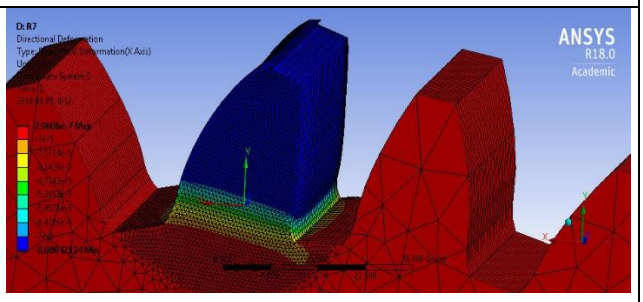
x direction 1. tooth root	*x* direction 2. tooth root
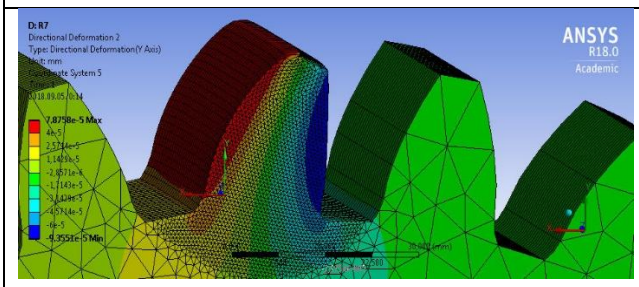	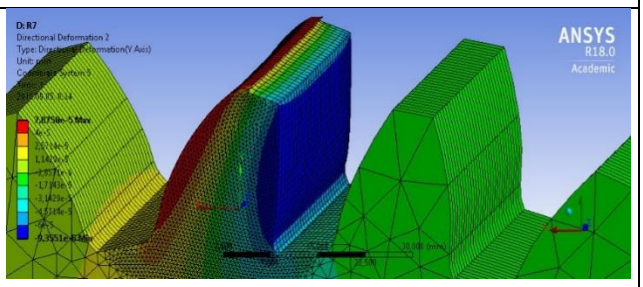
y direction 1. tooth root	*y* direction 2. tooth root
Fillet radius: R7	
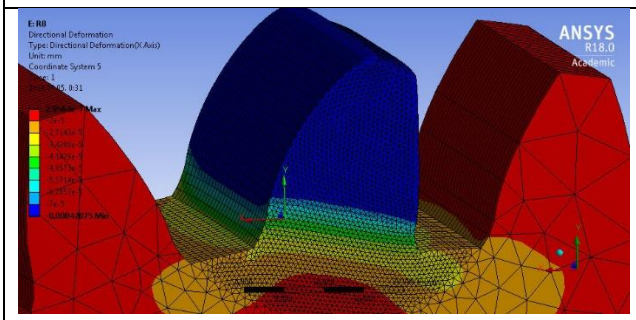	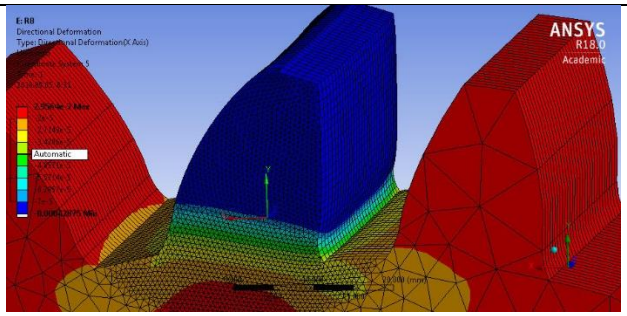
x direction 1. tooth root	*x* direction 2. tooth root

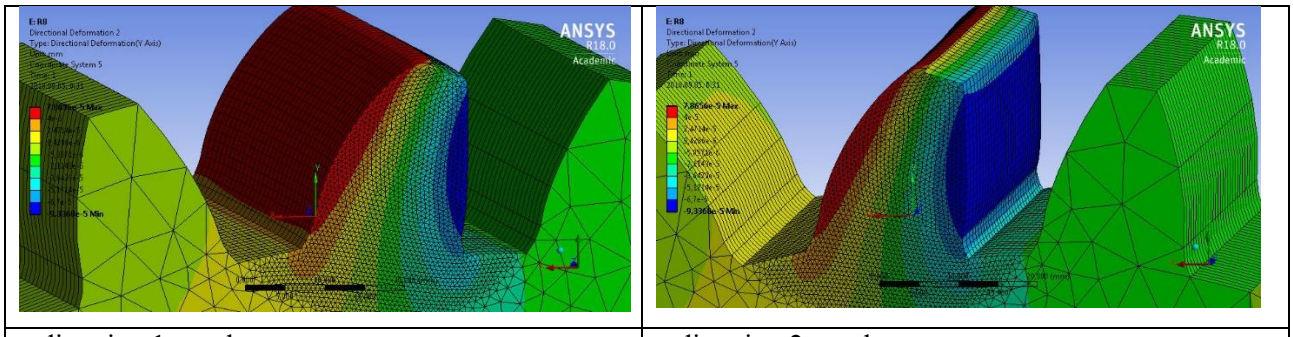

y direction 1. tooth root	*y* direction 2. tooth root
Fillet radius: R8	

Fig. 14. Normal deformation distribution on the 1 and 2 fillet radius of the driven gear

Based on the TCA results the average normal deformation values are calculated in different directions on the fillet radiuses (Fig. 14).

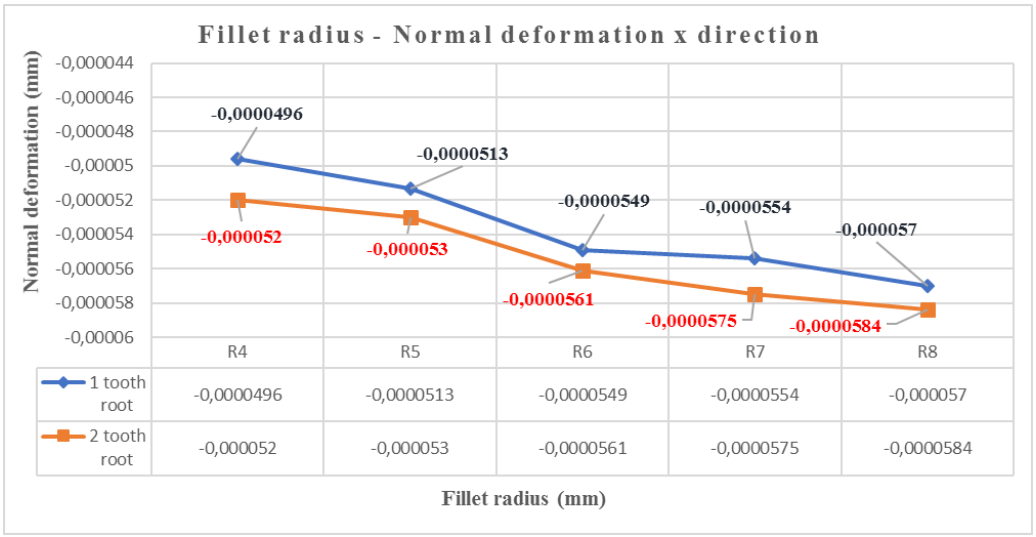

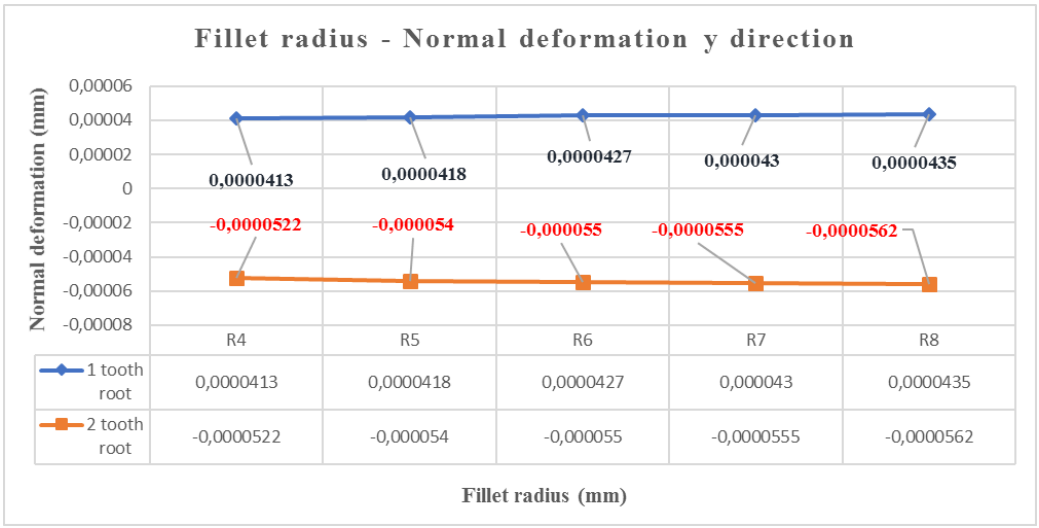

Fig. 15. The normal deformation results in the function of the fillet radius of the driven gear

In case of the 1. tooth root it could be determinable that the average normal deformations are decreased on the x direction in the function of the increasing of the fillet radius. The average normal deformations are increased on the y direction in the function of the increasing of the fillet radius (Fig. 15).

In case of the 2. tooth root it could be determinable that the average normal deformations are decreased on the x direction in the function of the increasing of the fillet radius. The average normal deformations are decreased on the y direction in the function of the increasing of the fillet radius (Fig. 15).

4.3. Analyses of the normal elastic strains on different directions

According to the coordinate system arrangement the normal elastic strains of the fillet radiuses are analyzed on x and y directions (Fig. 16).

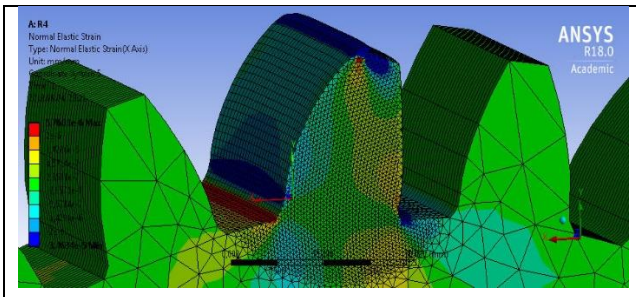	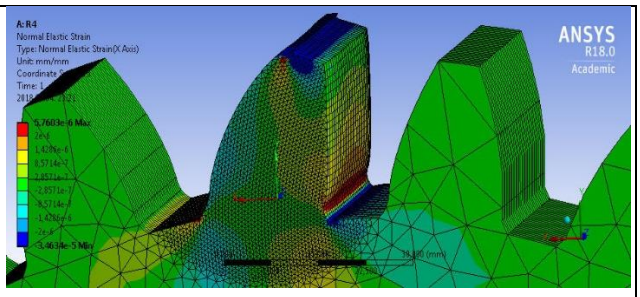
x direction 1. tooth root	*x* direction 2. tooth root
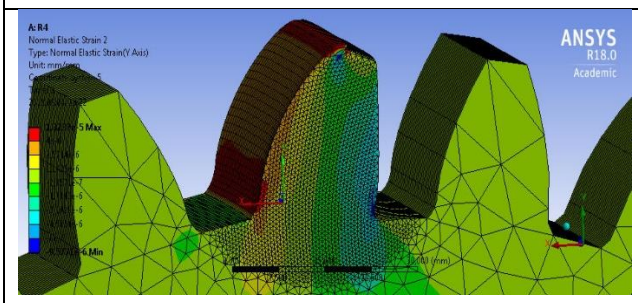	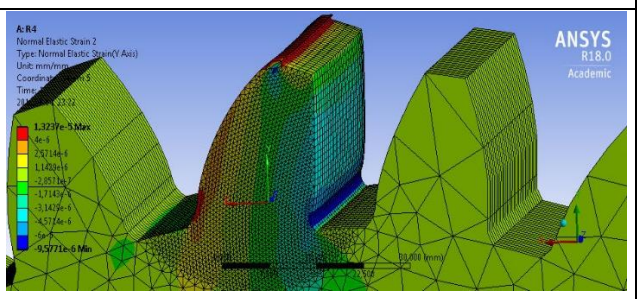
y direction 1. tooth root	*y* direction 2. tooth root
Fillet radius: R4	
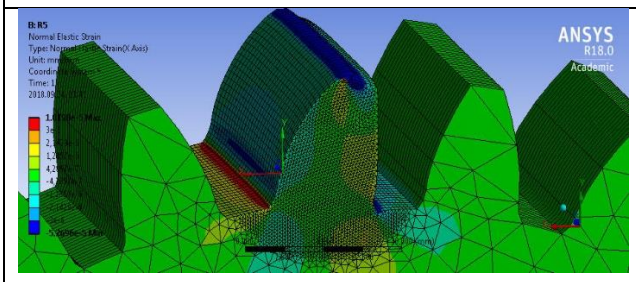	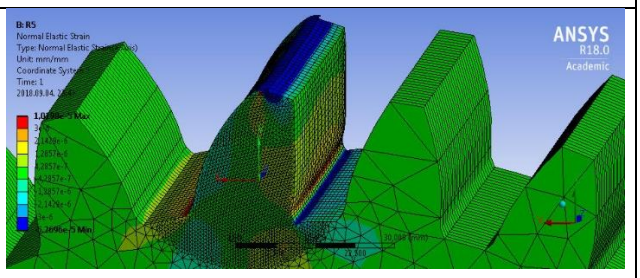
x direction 1. tooth root	*x* direction 2. tooth root
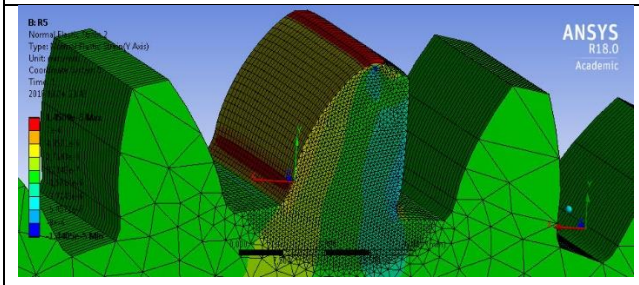	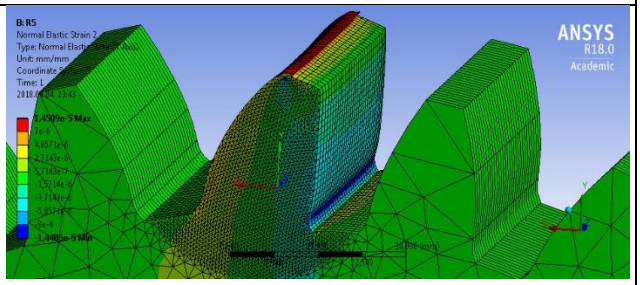

y direction 1. tooth root	*y* direction 2. tooth root
Fillet radius: R5	
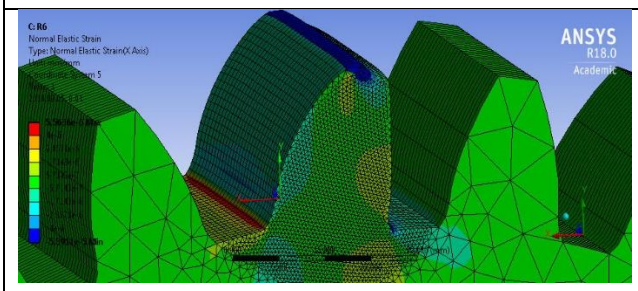	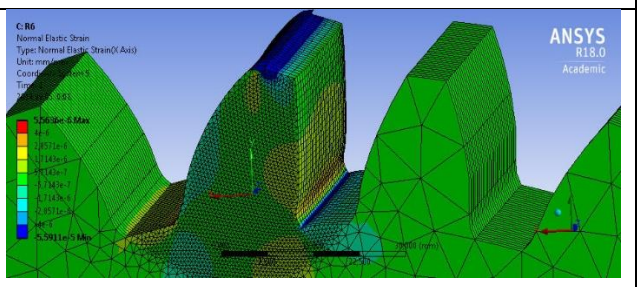
x direction 1. tooth root	*x* direction 2. tooth root
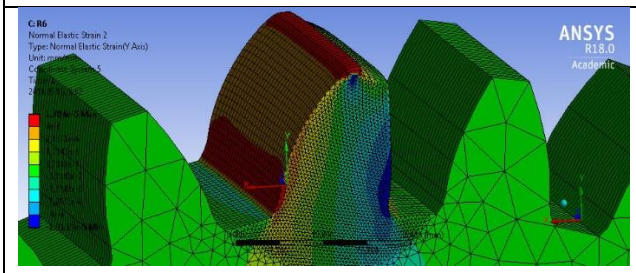	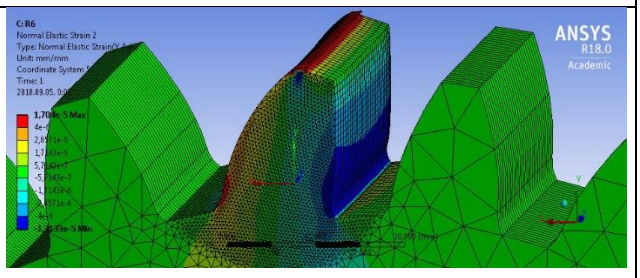
y direction 1. tooth root	*y* direction 2. tooth root
Fillet radius: R6	
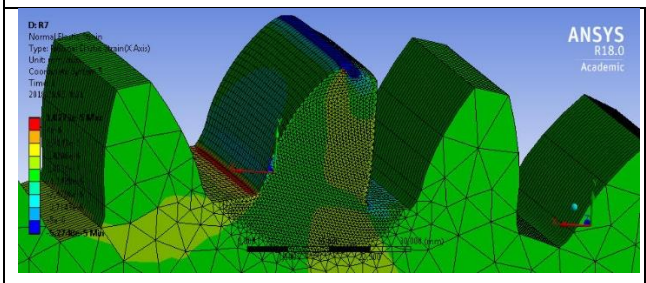	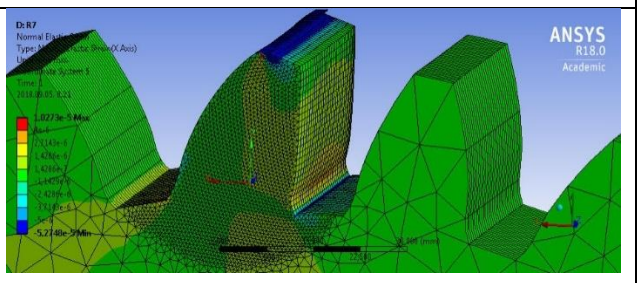
x direction 1. tooth root	*x* direction 2. tooth root
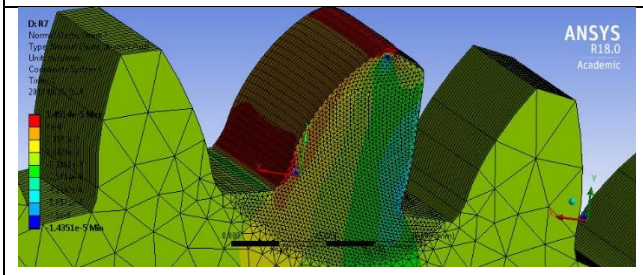	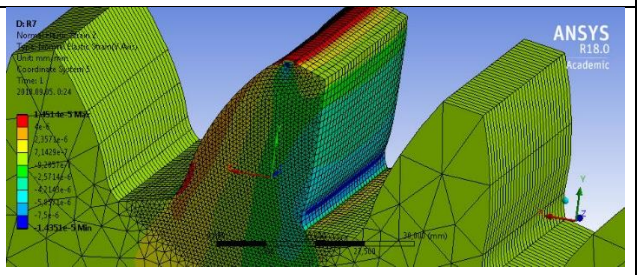
y direction 1. tooth root	*y* direction 2. tooth root
Fillet radius: R7	
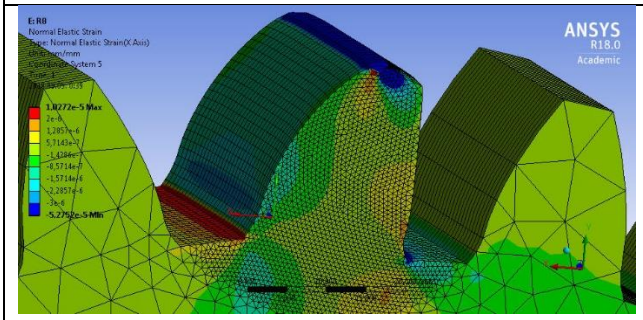	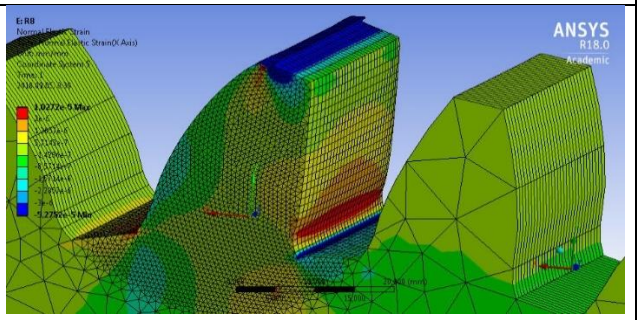

x direction 1. tooth root	*x* direction 2. tooth root
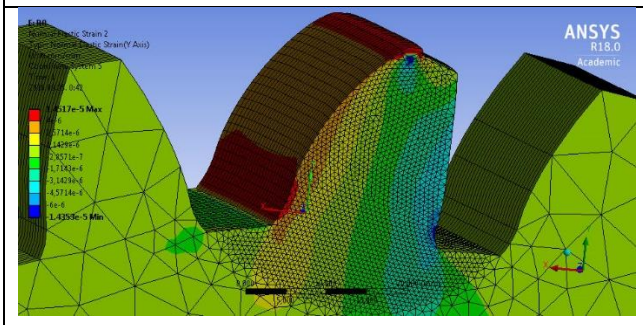	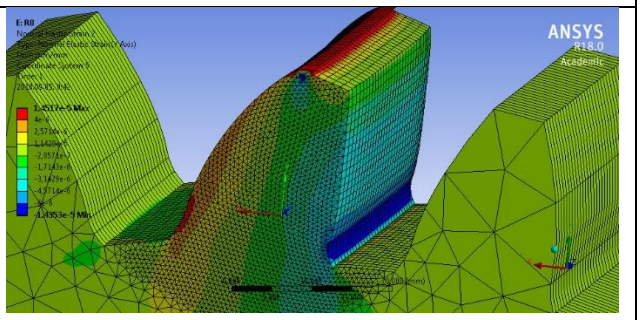
y direction 1. tooth root	*y* direction 2. tooth root
Fillet radius: R8	

Fig. 16. Normal elastic strain distribution on the 1 and 2 fillet radius of the driven gear

Based on the TCA results the average normal elastic strain values are calculated in different directions on the fillet radiuses (Fig. 16).

In case of the 1. tooth root it could be determinable that the average normal elastic strain are increased on the *x* direction in the function of the increasing of the fillet radius. The average normal elastic strain are decreased on the y direction in the function of the increasing of the fillet radius (Fig. 17).

In case of the 2. tooth root it could be determinable that the average normal elastic strain are increased on the *x* direction in the function of the increasing of the fillet radius. The average normal elastic strain are decreased on the y direction in the function of the increasing of the fillet radius (Fig. 17).

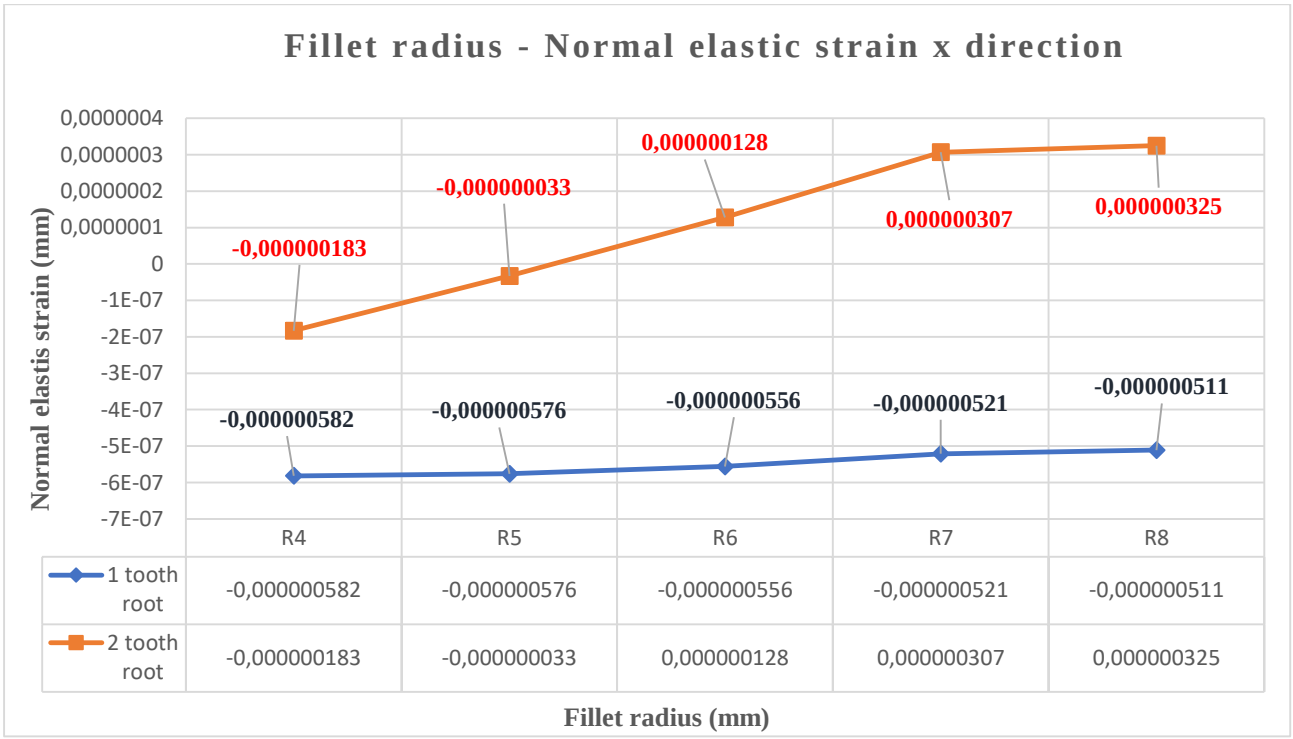

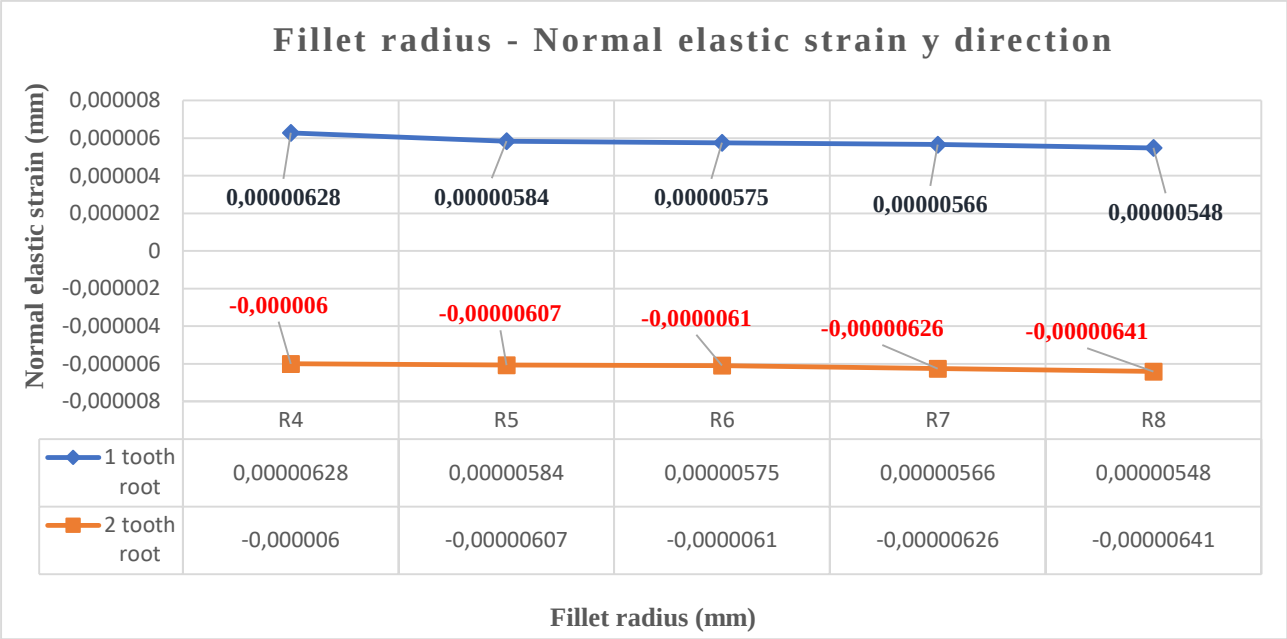

Fig. 17. The normal elastic strain results in the function of the fillet radius of the driven gear

Conclusion

Based on the geometric parameters of the x-zero gear drives a computer aided software has been developed to ease the designing process of the gears. Based on the calculated parameters the CAD models could be designed in SolidWorks software.

An x-zero gear drive having concrete geometry has been designed. The fillet radius is modified on the driven gear beside of the constancy of the other geometric parameters that is why we have received five types of x-zero gear drive having different fillet radiuses of the driven gear.

TCA analyses have been done on these gear drives to determine the normal stress, normal deformations and normal elastic strain distributions on different coordinate directions. Certainly the loads and boundary conditions were the same. The fillet radiuses have been analyzed by connection and concrete force load. The appropriate selection of the fillet radius is depended on the optimum purpose (normal stress, deformation or elastic strain). Based on the received results we determine the consequences.

The analysis and the appropriate selection of the fillet radius are important for the avoidance of the tooth break and increasing of the tool life.

Acknowledgement

EMBERI ERŐFORRÁSOK MINISZTÉRIUMA
„SUPPORTED BY THE ÚNKP-18-4 NEW NATIONAL EXCELLENCE PROGRAM OF THE MINISTRY OF HUMAN CAPACITIES”

REFERENCES

[1] S. Bodzás, "Computer aided designing and modelling of x-zero gear drive", *International Review of Applied Sciences and Engineering,* Volume 8, Number 1, Akadémiai Kiadó, 2017, pp. 93-97, ISSN 2062-0810, DOI 10.1556/1848.2017.8.1.13

[2] S. Bodzás, "Computer aided designing and modelling of spur gear pairs having normal and modified straight teeth", *International Review of Applied Sciences and Engineering* (during publication)

[3] I. Dudás, "Gépgyártástechnológia III., A. Megmunkáló eljárások és szerszámaik, B. Fogazott alkatrészek gyártása és szerszámaik", *Műszaki Kiadó,* Budapest, 2011.

[4] L. Dudás, "Kapcsolódó felületpárok gyártásgeometriai feladatainak megoldása az elérés modell alapján", Kandidátusi értekezés, Budapest, TMB, 1991., p.144., 2005. 06. 29.

[5] D. W. Dudley, „Gear Handbook", *MC Graw Hill Book Co.* New York-Toronto-London, 1962.

[6] Gy. Erney, "Fogaskerekek", *Műszaki Könyvkiadó*, Budapest, 1983., p. 460.

[7] A. Fuentes, R. Ruiz-Orzaez, I. Gonzalez-Perez, "Computerized design, simulation of meshing, and finite element analysis of two types of geometry of curvilinear cylindrical gears", *Computer Methods Apply Mechanical Engineering,* Elsevier, 2014, pp. 321-339

[8] I. Gonzalez-Perez, V. Roda-Casanova, A. Fuentes, "Modified geometry of spur gear drives of compensation of shaft deflections", *Meccanica,* 2015, pp. 1855-1867, DOI 10.1007/s11012-015-0129-9

[9] F. L. Litvin, A. Fuentes, "Gear Geometry and Applied Theory", *Cambridge University Press*, 2004., ISBN 978 0 521 81517 8

[10] F. L. Litvin, "A fogaskerékkapcsolás elmélete". *Műszaki Könyvkiadó*, Budapest, 1972.

[11] S. Pálinkás, Gy. Krállics, Z. Bézi, "Modelling of Crown and Cold Rolled Aluminum Sheet", *Materials Science Fórum,* pp. 115 – 124, 2013

[12] V. Rohonyi, "Fogaskerékhajtások", *Műszaki Könyvkiadó*, Budapest, 1980.

[13] Z. Terplán, "Gépelemek IV.", Kézirat, *Tankönyvkiadó,* Budapest, 1975., p. 220.

[14] I. Páczelt, T. Szabó, A. Baksa, "A végeselem módszer alapjai", Miskolci Egyetem, p. 243.

[15] T. Mankovits, T. Szabó, I. Kocsis, I. Páczelt, "Optimization of the Shape of Axi-Symmetric Rubber Bumpers", *Strojniski Vestnik-Journal OF Mechanical Engineering,* 2014, pp. 61-71.

Tensile Strength Analysis of 3D Printer Filaments

Dávid Halápi[1], Sándor Endre Kovács[1], Zsolt Bodnár[2],
Árpád B. Palotás[1], László Varga[1]
University of Miskolc[1], Philament Ltd. Miskolc[2]

Keywords: PLA, mechanical properties, 3D printing, additive manufacturing, tensile tests

Abstract:

The objective of this work is the mechanical characterization of materials produced by 3D printing based on Fused Deposition Modelling (FDM®). The materials chosen are various polylactic acid (PLA) bases reinforced with another material (e. g. glass fiber, metal powder, ….) in different weight fractions. In view of the FDM technique, producing specimens layer by layer and following predefined orientations, the main assumption considered is that the materials behave similarly to laminates formed by orthotropic layers. Great emphasis must be put on the selection of the appropriate quality filaments, therefore first the material properties of the fibers were examined. Following tensile strength tests, scanning electron microscopy (SEM) was employed to observe fracture surfaces. It was clear from the microstructure of the filaments that the morphology of the fibers are material dependent. This difference as well as the diverse types of the fibers explains the variability in material properties among the test materials examined.

Introduction

A 3D prototype manufacturing became quite widespread nowadays, a lot of manufacturer offers various printers with different solutions, at an available price. One can 3D print virtually anything and everything [1].

Prototype production can be categorized into three groups:

- Formative manufacturing (e.g., casting, plastic forming);
- Subtractive manufacturing (e.g., forging, turning, routing, etc.);
- Additive manufacturing (3D printing, etc.).

In this paper we will discuss additive manufacturing in detail. Fig. 1. shows the available 3D printing technologies. Fused Filament Fabrication (FFF) technology was selected for this set of experiments. As a comparison, SLA subjects made by SLA technology was also analyzed. Our goal was to select the process that produces the best tensile strength results.

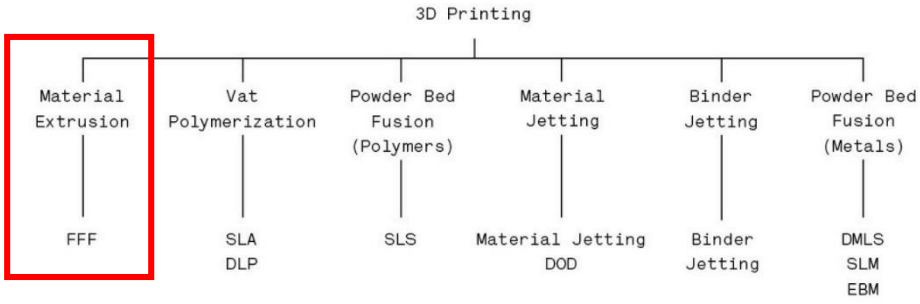

Fig. 1. Additive 3D technologies [2]

Each 3D printing process uses different materials (shown in Fig. 2). It is clear, that the chosen technology, the FFF process, is based on polymer-based materials. During the analysis mechanical properties were tested of these two kinds of polymer-based materials, the thermoplastics and the thermosets. [3]

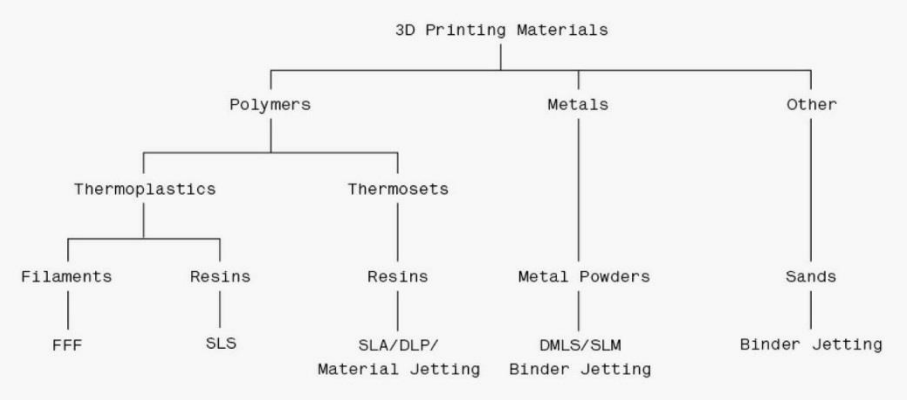

Fig. 2. Material classification of 3D printing [2]

Fig. 3 illustrates two comparisons, one, characterizing the 3D printed object by function and the other being the visual appearance / surface quality. It is essential to choose the printer technology according to what is more important. As stated above, each process has its own materials, and thus each has its own strengths and weaknesses. One always has to keep in mind what to achieve by printing something.

Our primary goal was comparing the available strength data of the newer types of filaments' properties. As Fig. 3 states, some of the 3D printed objects made of these filaments exhibit up to 30 MPa tensile stress.

When testing filaments enhanced by additive materials, the tensile stress properties of the specimens can exhibit as high as 50 MPa. As for visual appearance, the FDM filaments have strong potentials in the textured raw materials section.

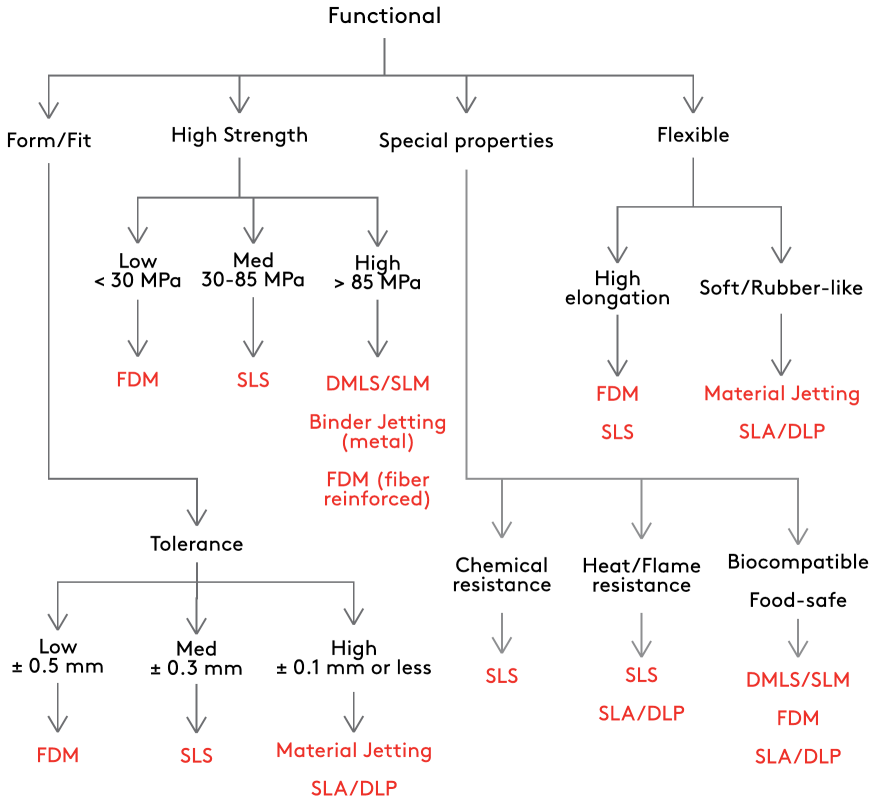

Fig. 3. Classification according to applicability and special properties [2]

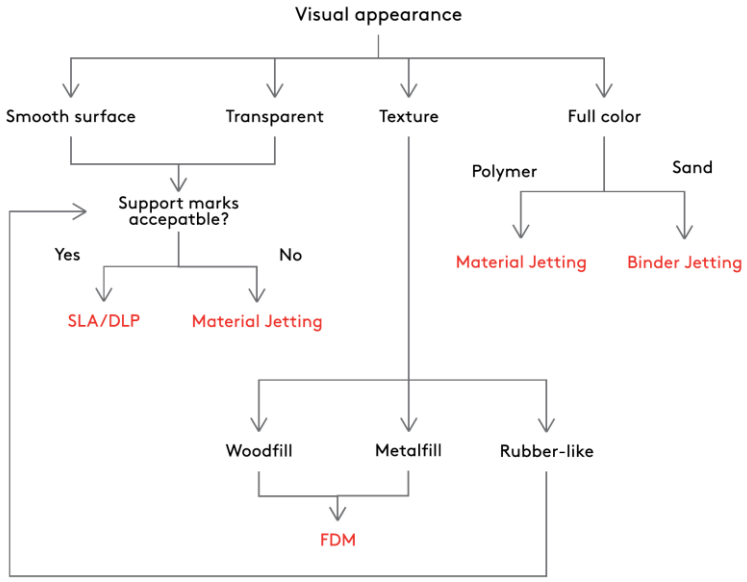

Fig. 4. Variety of visual appearance [2]

The PLA polymer threads basically have low tensile stress properties, however, they are available at a very attractive price. Fig. 5 shows the comparison between the fiber materials for semi-crystalline and amorphous structures. The other categorization possibility is based on the strength properties. There are general materials, engineering materials, with advanced strength properties, and high-performance materials.

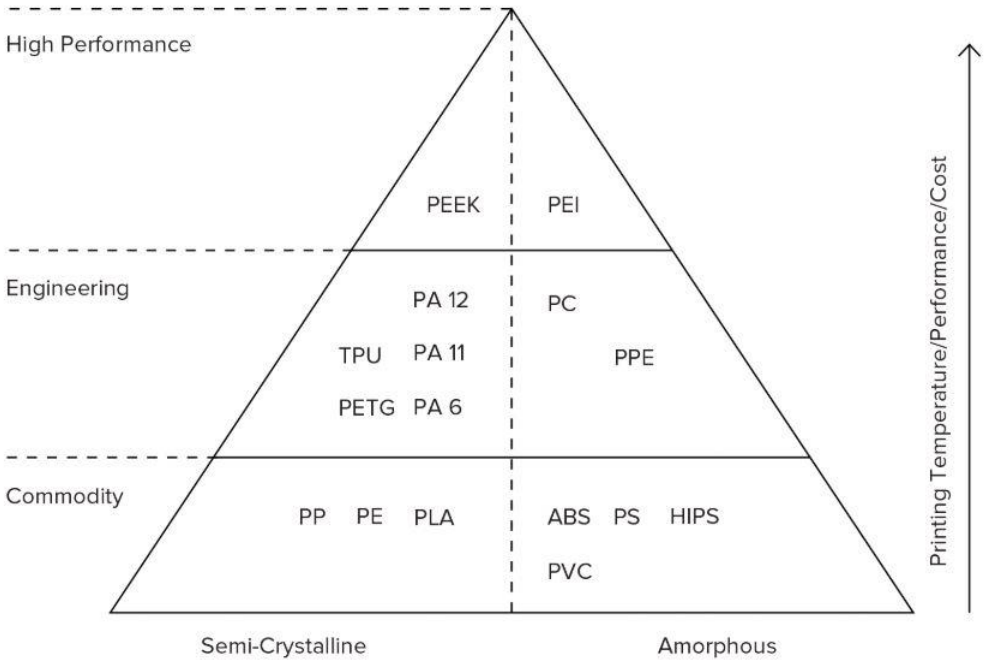

Fig. 5. Categorization of 3D Materials by Field of Application [2]

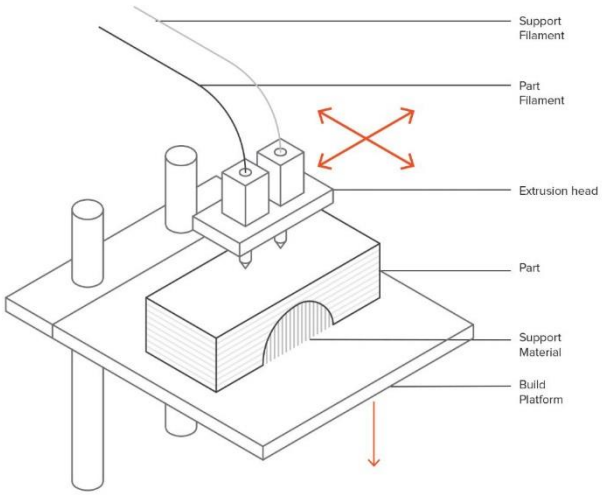

Fig. 6. Schematic and motion solution of FFF printer [2]

For the purpose of the current analysis Fused Deposition Modelling (FDM) (or Fused Filament Fabrication (FFF)), was chosen as the technology. This is the most widely used 3D printing technology.

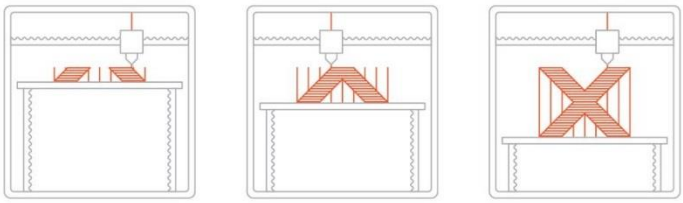

Fig. 7. The part making process [2]

Materials and Method

For the analysis 6 different FDM threads were tested. Our goal was to compare the tensile strength properties of the PLA (Poly-lactic Acid) based materials some of them with different additive materials. Two different methods were used: first, the tensile stress test specimens were compared, then the stress properties of each thread materials were analyzed. During the tests each thread's outer diameter was 1,75 mm. Printing was executed by a Cetus MKII extended 3D printer. As for the first wave of test specimens the printer's basic settings were used during the printing process, with 100% filling. The printed tensile strength test specimen was made according to the ISO 3167 1994 standard's parameters, with a thickness of 4 mm. These details are shown in Fig. 8. The threads contained the following additive materials [4]:

- White – chalk powder
- Black – "technical"
- Blue – 5% glass fiber
- Red – basic PLA
- Glass – 15% glass fiber
- Metal 10% – 10% metal powder
- SLA – SLA specimen without UV curing
- SLA UV – SLA specimen + UV furnace curing after printing

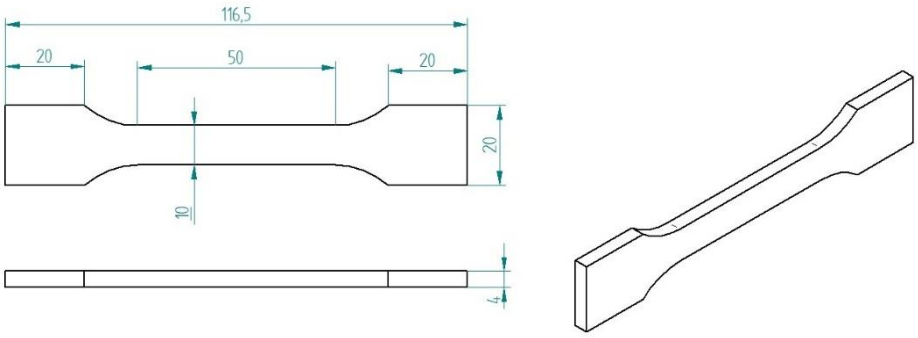

Fig. 8. ISO 3167 1994 specimen

Results

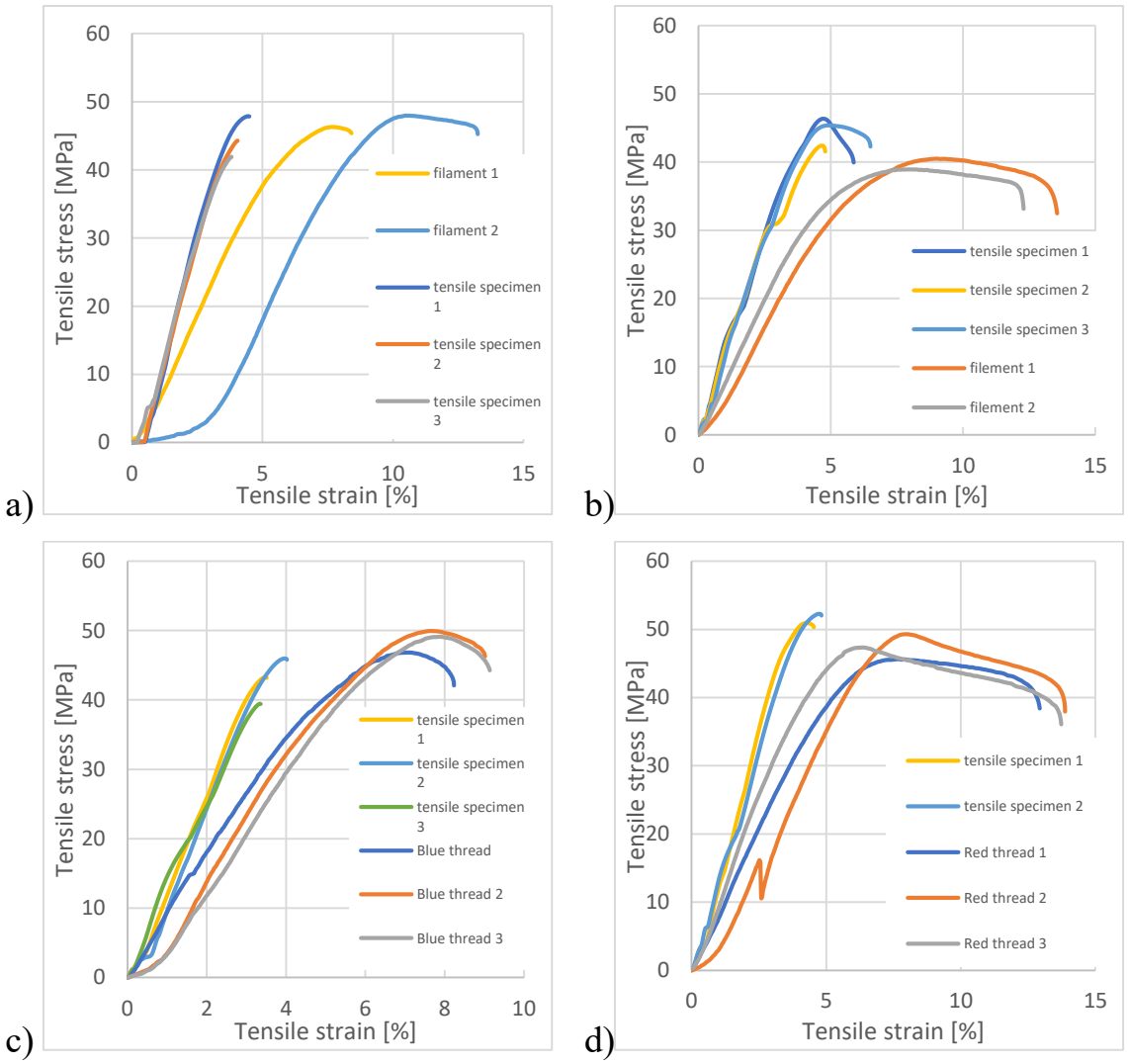

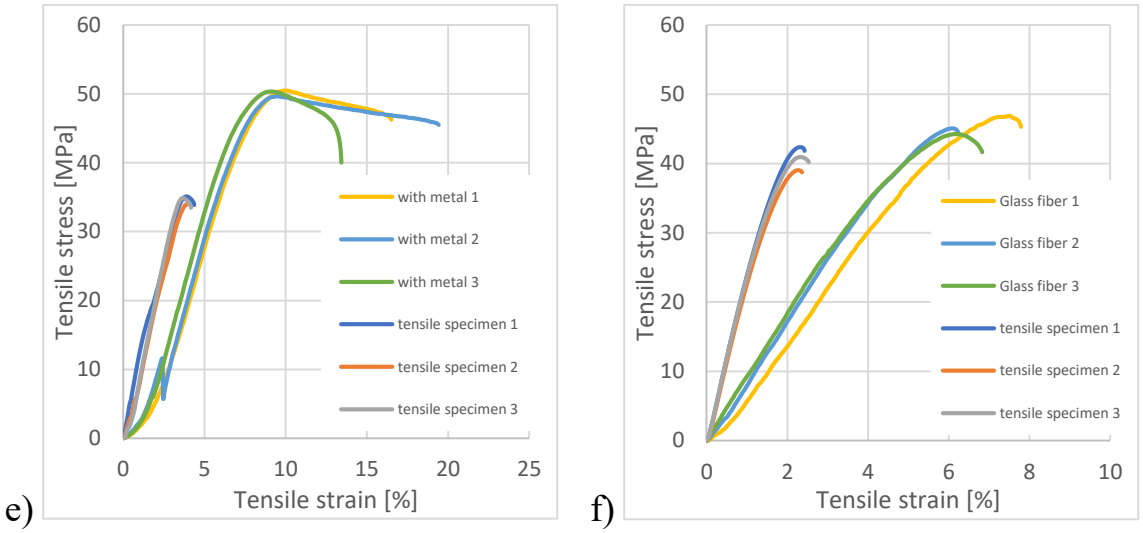

Fig. 9. Tensile test specimen – a) white, b) black, c) blue, d) red e) metal 10% and f) glass fiber thread

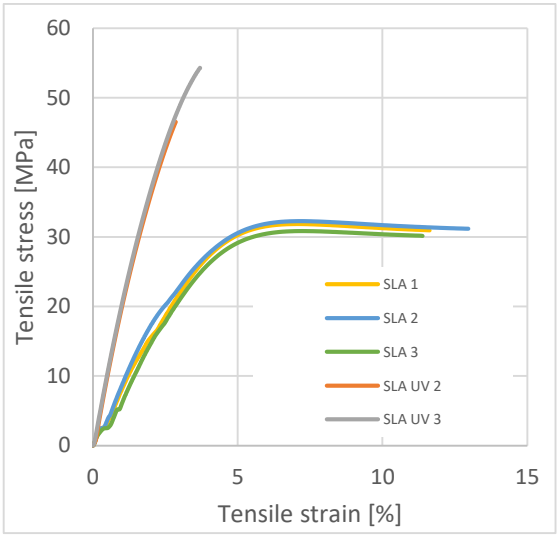

Fig. 10. Tensile test specimen: SLA

Results of the experiments are summarized in Figs. 9 and 10. One can clearly note, that the printing procedure weakens the material, i.e., the tensile strength of a printed specimen is lower than that of the original filament thread when there is an additive in the material.

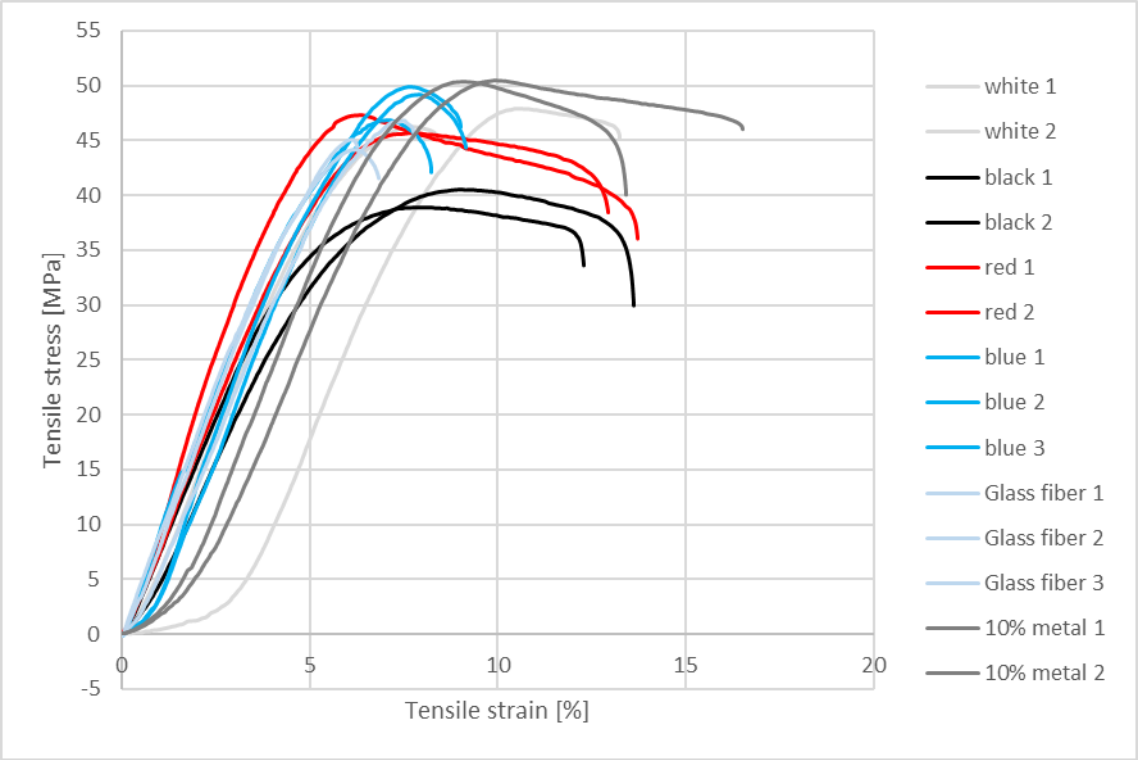

Fig. 11. Tensile test: all threads

Fig. 11. summarizes the test results in one single diagram. Tensile stress data are between 38 and 50 MPa for all the test materials. This result is not surprising, it is within the order of magnitude of the literature values.

Table 1. Summary of all tests

	Load at Maximum Tensile stress	Maximum Tensile stress	Maximum Tensile strain
	(N)	(MPa)	(%)
White 1	93,66455	38,94	15,68
White 2	111,32887	46,29	8,44
White 3	115,35612	47,96	13,26
Average	106,78318	44,4	12,46
Minimum	93,66455	38,94	8,44
Maximum	115,35612	47,96	15,68
Black 1	99,8094	41,5	20,16
Black 2	97,42329	40,5	18,58
Black 3	93,58906	38,91	12,28
Average	96,94058	40,3	21,24
Minimum	93,58906	38,91	18,58
Maximum	99,8094	41,5	24,97

Blue 1	112,69218	46,85	8,25
Blue 2	120,06435	49,92	9,03
Blue 3	118,17847	49,13	9,16
Average	116,97833	48,63	8,81
Minimum	112,69218	46,85	8,25
Maximum	120,06435	49,92	9,16
Red 1	109,7603	45,63	15,16
Red 2	118,57289	49,3	16,17
Red 3	113,91006	47,36	16,59
Average	114,08109	47,43	15,97
Minimum	109,7603	45,63	15,16
Maximum	118,57289	49,3	16,59
Metal 10% 1	121,36352	50,46	16,55
Metal 10% 2	119,41391	49,65	19,49
Metal 10% 3	121,09051	50,34	13,45
Average	122,8841	51,09	11,71
Minimum	120,62265	50,15	16,49
Maximum	119,41391	49,65	13,45
Glass 1	112,70834	46,86	7,81
Glass 2	108,35692	45,05	6,26
Glass 3	106,35715	44,22	6,86
Average	109,1408	45,38	6,98
Minimum	106,35715	44,22	6,26
Maximum	112,70834	46,86	7,81

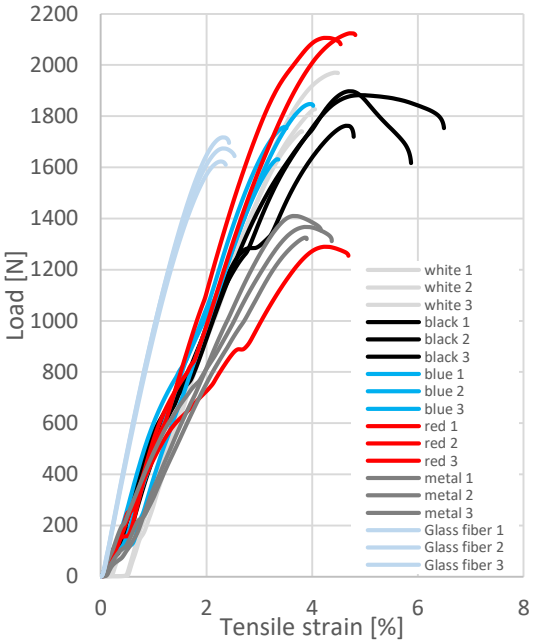

Fig. 12. Tensile stress

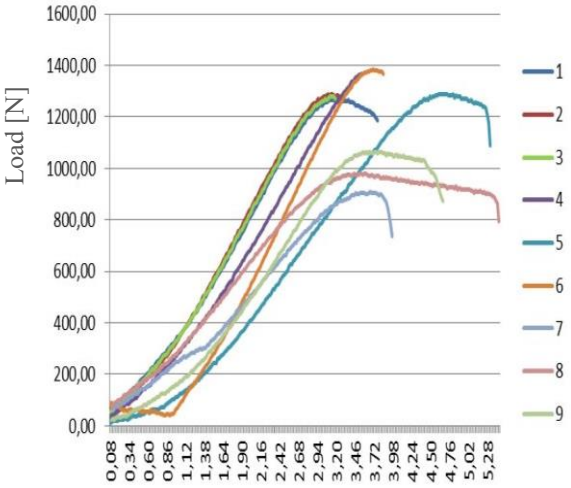

Fig. 13. Literature values [5]

Figs. 12 and 13 compares standard basic PLA from our own analysis and the literature. The geometry is identical for both cases [6].

Scanning electron micrographs (SEM images) of the various filament threads are shown in Figs. 14-19.

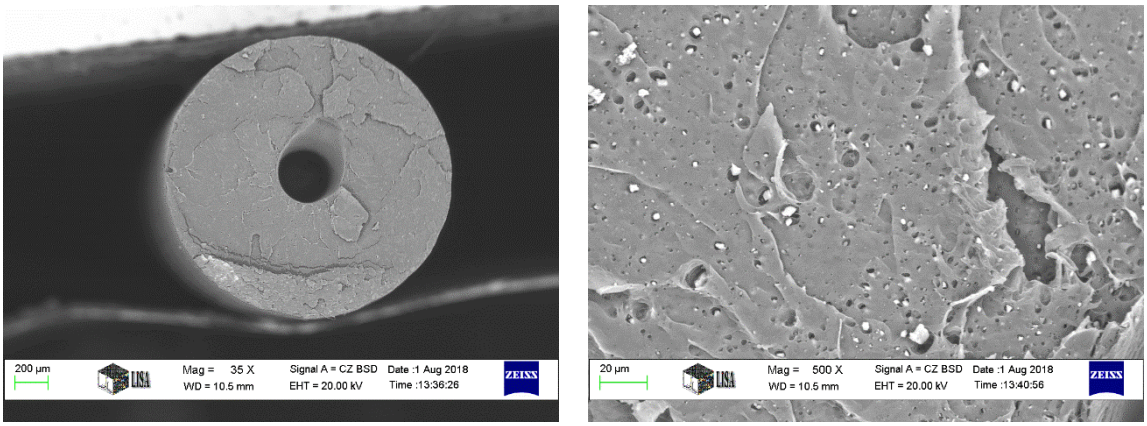

Fig. 14. Cross section of the PLA (White) filament by SEM magnified 35X; 500X

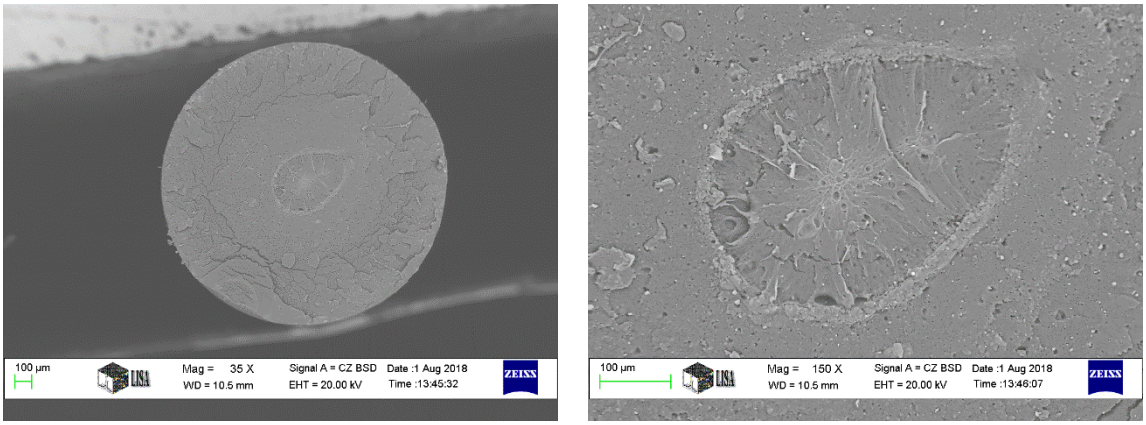

Fig. 15. Cross section of the PLA (Black) filament by SEM magnified 35X; 150X

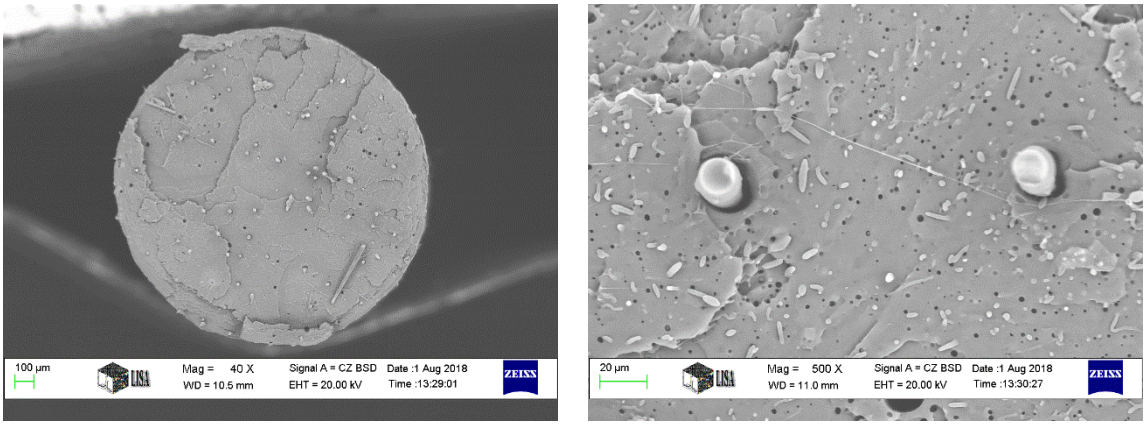

Fig. 16. Cross section of the PLA (Blue) filament by SEM magnified 40X; 500X

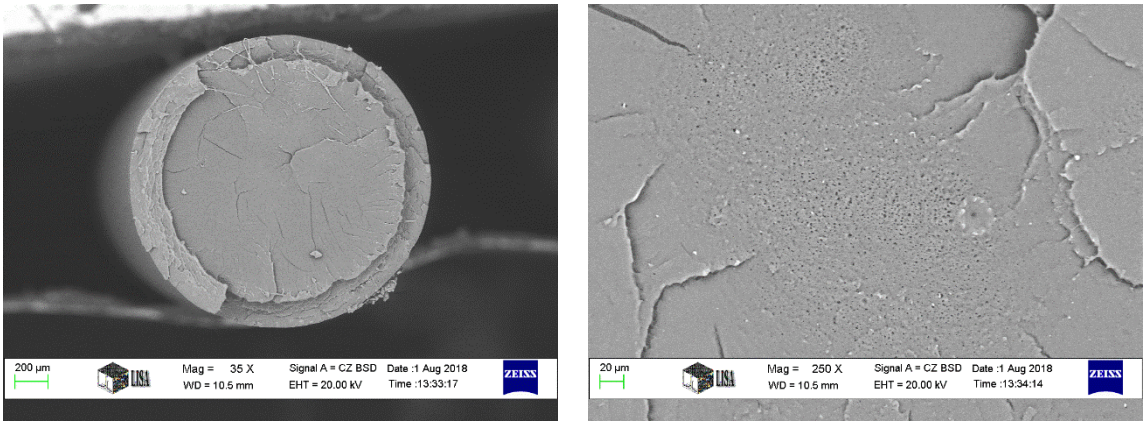

Fig. 17. Cross section of the PLA (Red) filament by SEM magnified 35X; 250X

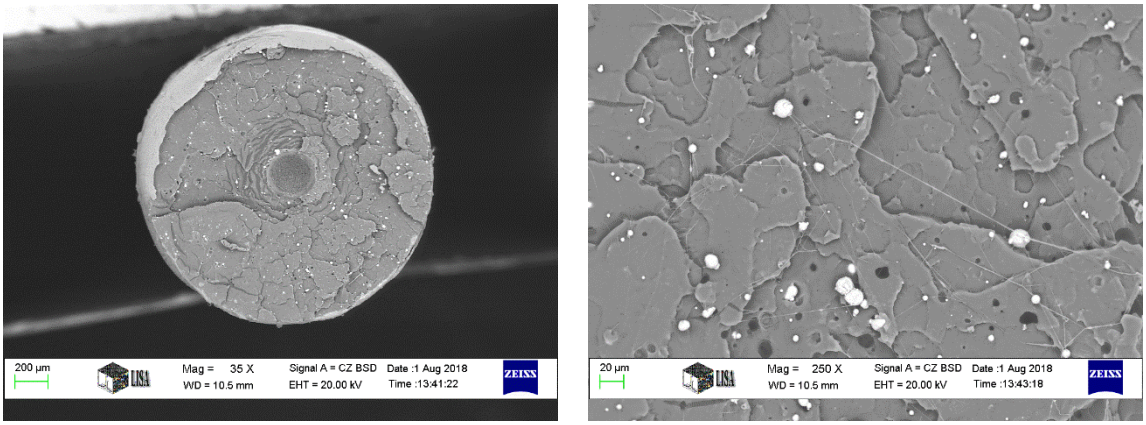

Fig. 18. Cross section of the PLA+10% metal powder filament by SEM magnified 35X; 250X

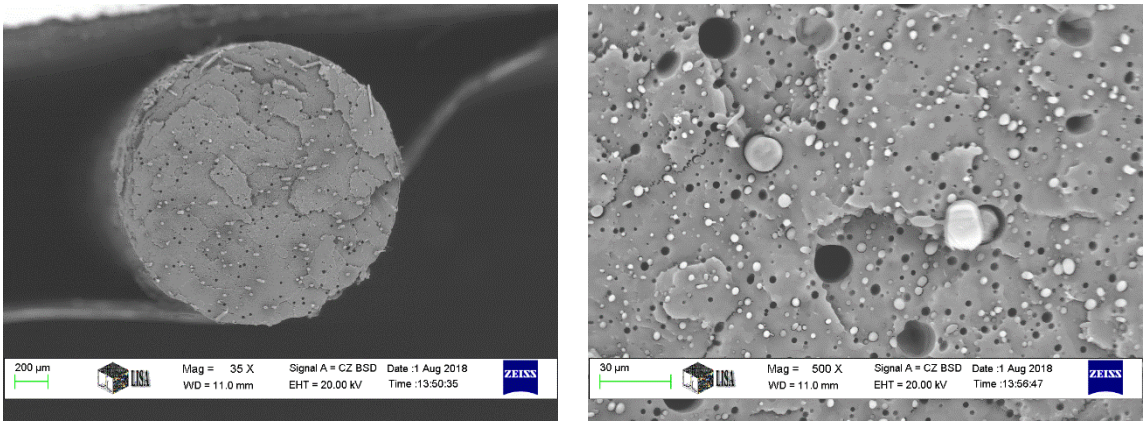

Fig. 19. Cross section of the PLA+glass fiber filament by SEM magnified 35X; 500X

Conclusions

Measurement data suggests that the printing process deteriorates some of the mechanical properties, i.e., namely the tensile strength value of the printed specimen is lower than that of the original filament thread of PLA with reinforcement additive. This finding seems to be additive independent.

Acknowledgements

The authors express their sincere appreciation to Philament Ltd. (Miskolc), for the samples and Árpád Kovács for the SEM analysis. This project was partially financed by the EU through the project TAMOP 6.3.1

REFERENCES

[1] J. Kietzmann, L. Pitt, and P. Berthon, “Disruptions, decisions, and destinations: Enter the age of 3-D printing and additive manufacturing,” Bus. Horiz., vol. 58, no. 2, pp. 209–215, 2015.

[2] B. Redwood, F. Schöffer, and B. Garret, “The 3D Printing Handbook,” 3D Hubs, p. 304, 2017.

[3] B. Berman, “3-D printing: The new industrial revolution,” Bus. Horiz., vol. 55, no. 2, pp. 155–162, 2012.

[4] Zsolt Bodnár, “Philament Technical materials.” [Online]. Available: www.philament.eu. [Accessed: 14-Aug-2018].

[5] Dénes Tóth, “Prototípusgyártás FDM eljárással,” 2015.

[6] R. T. L. Ferreira, I. C. Amatte, T. A. Dutra, and D. Bürger, “Experimental characterization and micrography of 3D printed PLA and PLA reinforced with short carbon fibers,” Compos. Part B Eng., vol. 124, pp. 88–100, 2017.

Complex study of the renal artery and its surroundings

Dávid Csonka[1], Péter Bogner[2], Iván Horváth[3],
Tornóczki Tamás[4], Károly Kalmár Nagy[5], István Wittmann[6], István Háber[1]

University of Pécs
[1]Faculty of Engineering and Information Technology, Department of Mechanical Engineering,
[2]Medical School, Department of Radiology, [3]Medical School, Heart Institute,
[4]Medical School, Department of Pathology, [5]Medical School, Surgery Clinic
[6]Medical School, 2nd Department of Medicine and Nephrological Center

Keywords: renal, haemodynamics, CFD, branching, kidney, rheology.

Abstract:

PURPOSE OF THE STUDY

Numerical fluid dynamic simulations, measurements and physiological investigation of the renal artery and its environment will be carried out to answer the following questions:

1. How does the renal artery branching angle, and the artery length affect the mass flow, pressure and flow speed of blood in the area of inspection?
2. What are the effects of the rheological factors examined on the kidneys?
3. What is the effect of vascular innervation on renal artery haemodynamics?
4. Does the distance between the arteria mesenterica and the arteria renalis along the aorta affect the renal blood flow parameters?
5. What is a suitable material model that characterizes the properties of the blood vessel wall in a finite element simulation?

HYPOTHESIS

The branching of the renal artery and the aorta in most patients is close to perpendicular. This results in high curvature of blood flow streamlines in the entrance of the artery, causing vortex and backflow. This turbulent flow leads to increased atherosclerosis, decreases the mass flow and flow speed in the artery and results in reduced pressure in smaller vessels. Therefore, we assume that there might be an optimal angulation of the renal artery, at which there is no dangerous backflow, but at the same time the protection of the glomeruli from systemic blood pressure is achieved.

We assume that the hemodynamic load of the kidney is also influenced by the nature of the oscillation in the renal artery. Because of this, a person may have an optimal artery length that can be taken into consideration during kidney transplantation.

Getting satisfyingly precise results requires setting up a numerical simulation environment that is as close to reality as possible, takes every known factor into consideration and is validated.

EXPECTED RESULTS

The planned study has both medical and technological goals. The numerical simulation methods regarding haemodynamics carried out so far use various approximations and do not take some possibly important factors into consideration, some are even neglected entirely.

The technological goal is to determine the importance of these factors and develop a precise simulation model. This could guide other researchers concerning the factors they can ignore. The outcome therefore is a numerical simulation model that is as close to reality as possible using current technology.

The medical findings can be of geometric nature, particularly optimal renal artery branching angle and length. The most important area of exploration is the possible correlation between physiological characteristics and haemodynamics which is tightly connected with geometry.

Exploring these coherences will result in answering the above questions and might reveal other connections we are yet unaware of.

Introduction

The main death cause in developed countries is related to blood circulation. In these cases, hypertension plays an important part, the second type of which is often caused by kidney disease and stenosis of the renal artery. In addition, the most common causes of kidney diseases have hemodynamic components, as well [1]

The haemodynamic conditions of the renal artery have been examined from several aspects, but mostly with many simplifications and only by emphasizing aspects closely related to the particular subject.

Further research in the subject therefore is of paramount importance, with the most accurate system approach in mind, considering all aspects of our knowledge. Combining geometric measurement data, numerical flow simulation results, histological and other physiological findings is needed. Thus, new connections between renal artery geometry, flow conditions and the general state of the kidneys can be investigated.

Background

The aorta-renal artery branching angle and the renal artery length affect the haemodynamic phenomena in the region of the branching, particularly the vorticity and the size of backflow zone. The mass flow and the flow speed increase due to the high curvature of the streamlines [2]. This turbulent flow leads to an increased chance for developing atherosclerosis, decreases the mass flow and flow speed in the artery and results in reduced pressure in smaller vessels.

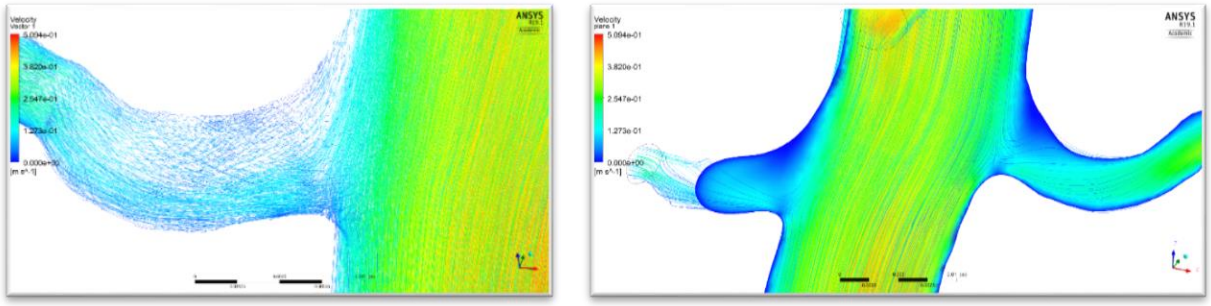

Fig. 1. CFD simulation generated with Ansys R19.1 Academic
showing the slow velocity zones of blood flow in the renal artery branching

This play a partial role in the fact that systemic blood pressure does not burden the glomeruli completely. In kidney diseases, when inflow increases (arteriola afferent dilation) intraglomerular pressure increase leads to glomerular damage.

In the region of the renal artery branching the risk of stenosis is increased due to vorticity. In the backflow zone there is a higher chance of deposition on the vessel wall [3].

Thus, the possibly optimal branching angle is sought, at which there is no dangerous backflow, while the protection of the glomeruli from systemic blood pressure is achieved.

We assume that the hemodynamic load of the kidney is also influenced by the nature of the oscillation in the renal artery. Because of this, a person may have an optimal artery length connected with the wavelength produced by the resting pulse. This optimal length can be taken into consideration during kidney transplantation.

Methods

Numerical flow analysis of the vessels requires a suitable finite element model. Many simulations have been carried out on highly idealized models, but in order to achieve the most realistic results, geometrical accuracy is required. Using simulation models that are not validated can be misleading.

For a detailed geometry, an accurate in vivo scan of the renal artery region is needed. The best method is using MRI or CT angiography to form a volume model that can be used in the numerical simulation.

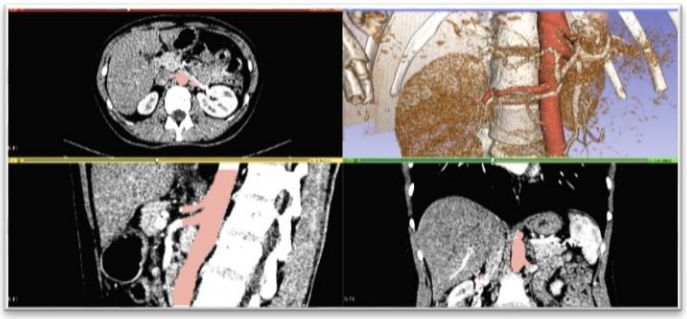

Fig. 2. Image generated using Slicer software from MRI angiography made at University of Pécs, Medical School, Department of Radiology

In addition, it is necessary to define the flow parameters in every vessel to retrieve boundary conditions of the simulation. There are several methods for measuring pressure and speed. For best results, it is best to determine the flow rate distribution along the vessel's cross section [4].

To measure the flow velocity in any section of the blood vessel, using phase contrast MRI is a very effective way [5]. This method consists of the use of time resolution phase contrast MR with three-dimensional velocity vector coding while simultaneously producing 3D anatomical images. The data produced this way can be used to validate the simulation.

Catheter angiography is very useful in understanding and measuring the pulsatile nature of the flow. The method uses a catheter along with x-ray imaging guidance and contrast material injected directly to the region of inspection from the catheter. The result is a very detailed image of the blood vessels.

Fig. 3. Catheter angiography made at University of Pécs, Medical School, Heart Institute

To get information about the physiological state of the kidney connected with geometry measurement data it is necessary to carry out measurements on the same patient. This requires involvement of pathological investigation on deceased patients. We measure the following:

- Length of the renal arteries
- Distance between the branching of the renal arteries along the aorta
- Distance between the branching of arteria mesenterica inferior and the arteria renalis closer to it along the aorta
- Fibrosis score based on histology samples from both kidneys

Geometric features of the renal artery

The geometric diversity of the abdominal aorta is investigated by O'Flynn et. al. [6]. The results suggests that very few in vivo data or images are available about the geometry of the abdominal aorta and its major peripheral branches. Therefore, further investigation and data collection is needed.

While investigating the surroundings of the renal artery branching, it became clear that in many cases the arteria mesenterica inferior is close to the branching of the renal artery. This may affect the flow conditions in the area, so we include the arteria mesenterica inferior and superior in the volume model and investigate the effect of its presence. For this we perform measurements about the distance between the renal and mesenteric arteries. (S_{mi}) Few studies have investigated the renal artery in relation to arteria mesenterica.

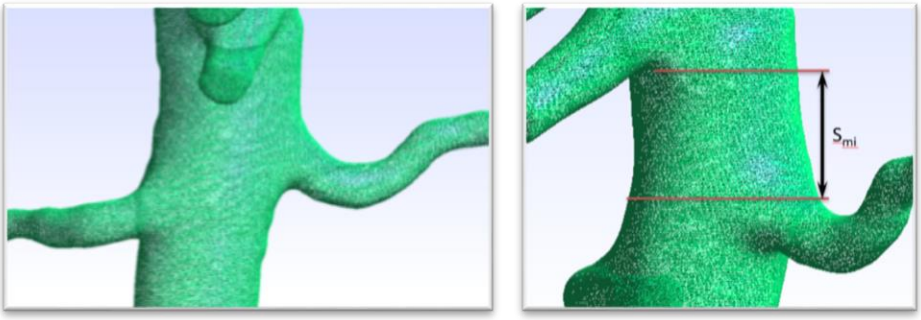

Fig. 4. Images of the mesh created from angiography MR made at University of Pécs, Medical School, Department of Radiology

Haemodynamics and numerical simulations of the renal artery

There are certain features of blood flow that need to be considered to achieve a precise simulation. In the literature, the calculations performed so far neglected most of these factors. We investigate them one by one to decide their importance by validating simulation results with measurements. Validation is substantial in getting useable results.

The factors we might consider important are as follows:

1. The pulsatile nature of blood flow

In most calculations this has been taken into account, so its significance is demonstrated [7]. Simulation results would be incorrect if we excluded the pulsatile flow speed curve.

2. Spirality of blood flow

The spiral nature of arterial blood flow is widely accepted. The spiral velocity component of the spiral flow has positive and negative effects on the haemodynamics of the artery. The results show that the helical effect causes a significant change in blood velocity distribution. Therefore, in an accurate simulation we probably need to consider this phenomenon. With increasing spiral flow intensity, the rate of turbulent kinetic energy production decreases.

In addition, the size of the recirculating zones decreases due to the spiral flow; this may reduce the extent and progression of atherosclerosis in the aorta-kidney artery branch.

Available results showed that the spiral nature of the blood flow in the renal arteries is atheroprotective and should be considered in the analysis of aortic and kidney arteries [8].

3. The vascular material model

In the literature, most simulations consider the arterial wall rigid. One of the reasons for this is that most of these studies relate to atherosclerosis, where deposition causes the artery wall to be less elastic [9]. In this case,

this simplification is permissible, but during the inspection of a healthy, flexible vascular wall the cross-sectional change occurring during the pulsatile flow must be considered. For this, there is a need for an appropriate vascular material model, and its elasticity equation.

Modeling the vessel wall as an elastic, solid body, with neglecting the gravitational forces, the stress-deformation relationship can be mathematically expressed as follows:

$$\rho_w \frac{\partial d_i}{\partial t^2} = \frac{\partial \sigma_{ij}}{\partial x_j} \tag{1}$$

Where

d_i : displacement tensor

σ_{ij} : stress tensor

ρ_w: vascular wall density

The stress tensor σ_{ij} can be expressed for a Hookean material as:

$$\sigma_{ij} = \lambda e_{kk} \delta_{ij} + 2\mu_L e_{ij} \tag{2}$$

Where

λ and μ_L : Lame's constants

δ_{ij} : Kroeneker delta

e_{ij} : strain tensor components

The strain tensor components can be gained from the equation:

$$e_{ij} = \frac{1}{2}\left(\frac{\partial d_i}{\partial x_j} + \frac{\partial d_j}{\partial x_i}\right) \tag{3}$$

The Lame's constants can be calculated as:

$$\lambda = \frac{\upsilon E}{(1+\upsilon)(1-2\upsilon)} \tag{4}$$

$$\mu_L = \frac{E}{2(1+\upsilon)} \tag{5}$$

Where

E : Young's modulus

υ : Poisson's ratio

4. The effect of innervation on the vascular properties

In the case of transplanted patients, the vascular wall is denervated, which, we assume, may affect its elasticity, resulting in a Young's modulus and a Poisson's ratio other than in case of artery of the native kidney. We also examine this possibility.

Expected results

The results of this interdisciplinary study consists of engineering and medical components. The engineering part is creating a satisfyingly precise simulation model that is as close to reality as possible and takes into account all the factors proven to be important. This result serves as a guideline that can be used to precisely simulate haemodynamics in this area.

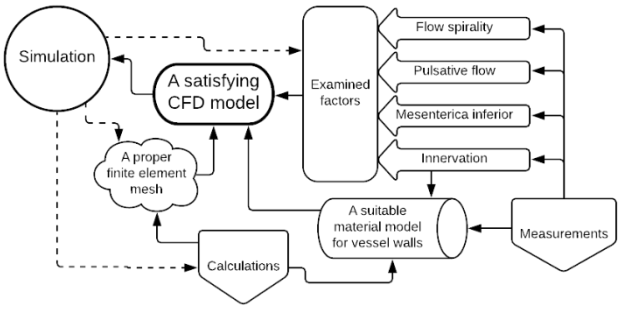

Fig. 5. A simplified flowchart of the acquisition of engineering results

We perform measurements and research to define flow spirality and pulsatility, the distance of the mesenterica inferior and the renal artery along the aorta and the elasticity of the vascular wall along with innervation effects on the material.

To determine the importance of the factors above defined we run simulations including or neglecting them and compare the results.

If the flow conditions are perpendicularly close to the measured data by PC-MRI, then the results and the model can be defined as satisfying and validated.

For the simulation to be precise a proper finite element mesh is also required. After some necessary iterations and refinement of the mesh the results will show valid data.

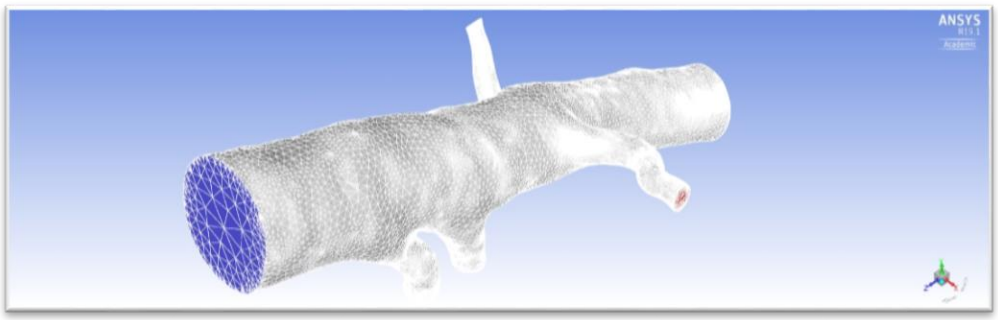

Fig. 6. Finite element mesh generated with Ansys R19.1 Academic

The results of the validated simulations will give a good feedback on the importance of the factors examined, the nature of the vessel wall material and the finite element mesh.

The other component of the results is of medical nature. We are looking for possible correlations between the general physiological status of the kidneys and the geometry of the renal arteries and its surroundings. The physical link between geometry and kidney status is haemodynamics. If we successfully complete the engineering part of the study, it makes the simulation of haemodynamics possible. And this means we can determine the haemodynamic characteristics of a given geometry and utilize it in transplantation or diagnostics.

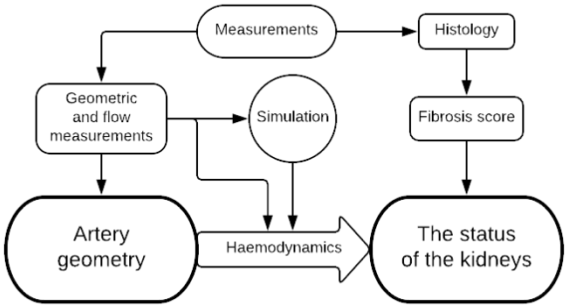

Fig. 7. A simplified flowchart of the acquisition of medical results

REFERENCES

[1] Faucon AL, Bobrie G, Jannot AS, Azarine A, Plouin PF, Azizi M, Amar L. "Cause of renal infarction: a retrospective analysis of 186 consecutive cases." *J Hypertens*. 2018 Mar;36(3):634-640. doi: 10.1097/HJH.0000000000001588. PubMed [citation] PMID: 29045340

[2] Mortazavinia Z, Arabi S, Mehdizadeh AR. "Numerical investigation of angulation effects in stenosed renal arteries." *J Biomed Phys Eng*. 2014 Mar 8;4(1):1-8. eCollection 2014 Mar. PubMed [citation] PMID: 25505762, PMCID: PMC4258856

[3] Albert S, Balaban RS, Neufeld EB, Rossmann JS. "Influence of the renal artery ostium flow diverter on hemodynamics and atherogenesis." *J Biomech*. 2014 May 7;47(7):1594-602. doi: 10.1016/j.jbiomech.2014.03.006. Epub 2014 Mar 20. PubMed [citation] PMID: 24703300, PMCID: PMC4035116

[4] Maier SE, Scheidegger MB, Liu K, Schneider E, Bollinger A, Boesiger P. "Renal artery velocity mapping with MR imaging." *J Magn Reson Imaging*. 1995 Nov-Dec;5(6):669-76. PubMed [citation] PMID: 8748484

[5] Stankovic Z, Allen BD, Garcia J, Jarvis KB, Markl M. "4D flow imaging with MRI." *Cardiovasc Diagn Ther*. 2014 Apr;4(2):173-92. Doi: 10.3978/j.issn.2223-3652.2014.01.02. Review. PubMed [citation] PMID: 24834414, PMCID: PMC3996243

[6] O'Flynn PM, O'Sullivan G, Pandit AS. "Geometric variability of the abdominal aorta and its major peripheral branches." *Ann Biomed Eng*. 2010 Mar;38(3):824-40. Doi: 10.1007/s10439-010-9925-5. Epub 2010 Jan 20. PubMed [citation] PMID: 20087766

[7] Grechy L, Iori F, Corbett RW, Gedroyc W, Duncan N, Caro CG, Vincent PE. "The Effect of Arterial Curvature on Blood Flow in Arterio-Venous Fistulae: Realistic Geometries and Pulsatile Flow." *Cardiovascular Engineering and Technology.* 2017 Jul 26; 8(3): 313-329 PMC [article] PMCID: PMC5573765, PMID: 28748414, DOI: 10.1007/s13239-017-0321-2

[8] Javadzadegan A, Simmons A, Barber T. "Spiral blood flow in aorta-renal bifurcation models." *Comput Methods Biomech Biomed Engin.* 2016;19(9):964-76. doi: 10.1080/10255842.2015.1082552. Epub 2015 Sep 28. PubMed [citation] PMID: 26414530

[9] Kagadis GC, Skouras ED, Bourantas GC, Paraskeva CA, Katsanos K, Karnabatidis D, Nikiforidis GC. "Computational representation and hemodynamic characterization of in vivo acquired severe stenotic renal artery geometries using turbulence modeling." *Med Eng Phys.* 2008 Jun;30(5):647-60. Epub 2007 Aug 21. PubMed [citation] PMID: 17714975

Segmentation of Multiple Organs in Computed Tomography and Magnetic Resonance Imaging Measurements

A. Kriston[1], V. Czipczer[1,2], A. Manno-Kovács[1,2], L. Kovács[1], Cs. Benedek[1] and T. Szirányi[1]

[1] Hungarian Academy of Sciences, Institute for Computer Science and Control/Machine Perception Research Laboratory, Budapest, Hungary

[2] Pázmány Péter Catholic University, Faculty of Information Technology and Bionics, Budapest, Hungary

Keywords: Medical image segmentation, Multi-organ segmentation, 3D data representation

Abstract: The segmentation and visual representation of human organs on medical images with different modalities is of great importance in the study of medical analysis. In order to perform multi-organ segmentation on medical image sets, deep learning based methods were tested on publically available datasets. Moreover, custom developed algorithms were proposed to detect and segment specific organs, like liver and kidney. The algorithms and related results presented in this study are aimed to be implemented in a specific virtual reality hardware which will be used during physician-patient meetings to improve communication and also for teaching purposes of medical students.

Introduction

Segmentation of medical images is crucial for quantitative medical analysis and for visualizing organs of the human body. Manual segmentation is possible for an individual image and might be applied for small datasets, however it is not the way to process large dataset, where a single image volume of a human organ consists of hundreds or even thousands of images. The need for reliable and fast image segmentation algorithms is really important [1]. Although physicians have good understanding and able the perform diagnosis relying on their visual interpretation of grayscale images, patients face difficulties to understand those complex medical images. Segmentation and three-dimensional representation of patient's organs may facilitate the general understanding. The study presented in this paper aims to further advance the field of digital medical image processing and visualization used for medical teaching purposes and to improve the relation and communication between patients and physicians. During the current work different deep learning based multi-organ segmentation algorithms were tested on available datasets. Traditional image segmentation techniques like, region growing and active contour based methods were tried as well to segment liver and kidney.

Datasets

A common practice in medical diagnosis processes is to perform Computed Tomography (CT) and Magnetic Resonance (MR) imaging about patients to reveal diseases. In order to test image segmentation algorithms CT and MR volumes with and without contrast enhancement were acquired from various datasets. Different available databases, namely VISCERAL, BRATS and SLIVER07, as well as new hand labeled samples provided by the Medical School of University of Pécs were used for performing multi-organ image segmentation. The collected databases include samples of different MR acquisitions types, like Flair, T1, T1c, T2, which were used alone or combined as input for the algorithms. The volumes were in nifty (.nii) and MHA (.mha) file formats, which are common types for medical imaging purposes. To process the images in the CT and MR volumes, Matlab, C++ and Python codes were created.

Deep learning based image segmentation

The focus of the deep learning based image segmentation study was on testing the different methods and measure their performance on the acquired datasets. We have been looking for convolutional networks with various segmentation and classification capabilities of the organs. It is promising for these methods or similar approaches that e.g. in the case of [2], 281 labeled contrast CT scans were sufficient for teaching (460-1177 slice, 512x512 pixels, 0.5-1mm resolution), and for [3] 20 + 59 images (contrast abdominal CT, 512x512 pixels, 426 slice, 0.6-0.8mm resolution [4]) were sufficient. Such type of algorithms need a well-labeled set of ground truth data sets that are relevant to the particular segmentation or classification task. Such publicly available data sets are e.g. the BRATS [5] (cerebral tumors) and VISCERAL [4] (upper / abdominal, abdominal

organs). The nets used during the study were the two and three dimensional version of the U-Net and the WT-Net. The U-Net 2D network was tested on the VISCERAL data set for multiple organs (liver, pancreas, kidney) and on the BRATS which has brain volumes. We first separated the volumes containing individual organs, then randomly 10% of them were isolated for testing and the remainder (80-20%) was used for train - validation. The results are presented in Table 1.

Table 1. The caption format for the table is this, please use plain table without colors and other design

	Dice	Specificity/TNR	Sensitivity/recall	precision
2D U-Net				
liver	0.802679	0.99813	0.770739	0.89054
pancreas	0.305916	0.997472	0.32681	0.371207
kidney	0.651467	0.993629	0.913739	0.555003
brain	0.534425	0.999247	0.462648	0.761543
WT-Net				
brain	0.880051007466	0.995697035725	0.902059385208	0.871988
3D U-Net				
brain	0.606450440436	0.957828332746	0.799461787508	0.564523080524

A representative CT slice is shown by Fig. 1. Experts drawn contours of the liver then binary masks were generated that are used for training of the deep learning network. Expert defined label and corresponding prediction is shown by the figure.

Fig. 1 Example slice of a CT volume (left) of the Visceral dataset and the corresponding ground truth of the liver (middle) and resulted prediction by U-net.

Fig. 2 shows automatic liver segmentation result on a CT volume found in the VISCERAL database. The segmentation was performed using the 2D U-Net. Green color indicates the liver on both the ground truth and prediction images. We can see that prediction fails in some cases and the algorithm falsely labels pixels as liver too even further from abdominal region.

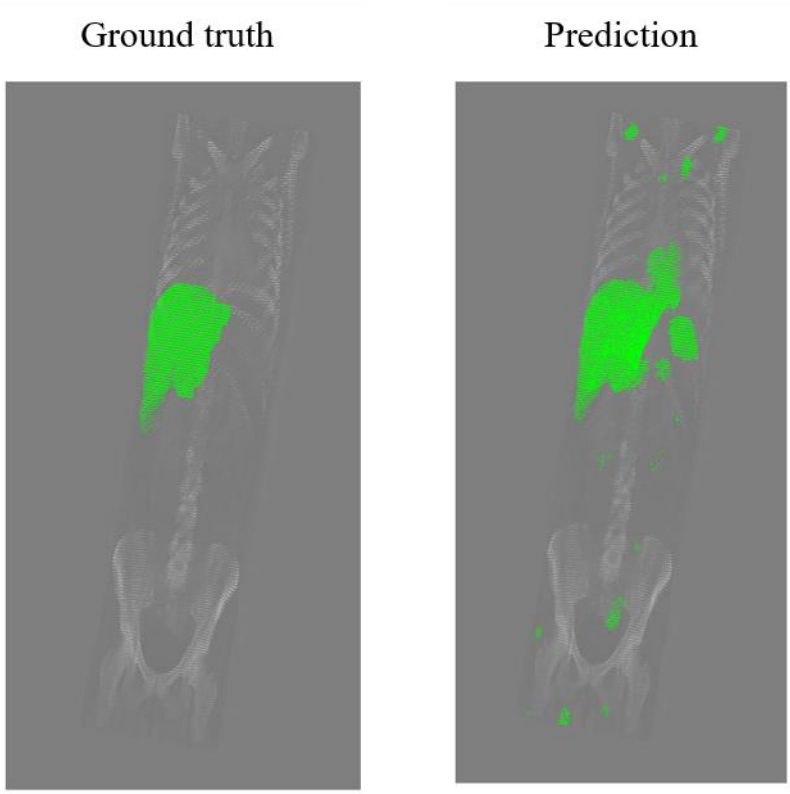

Fig. 2 Automatic segmentation on the Visceral dataset using U-net.

Individual slices of the segmented liver part is presented by Fig. 3. Different views show the shape of the liver. One can observe some segmentation faults that might be filtered by post-processing. Overall, the segmentation on this particular dataset seemed to be right.

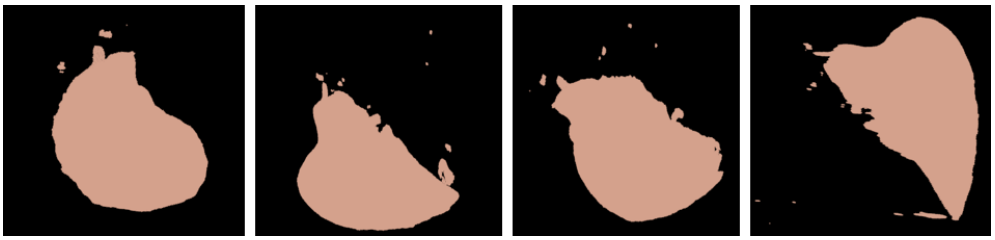

Fig. 3 Reconstruction of 3D point cloud of the automatically detected liver on a volume of the Visceral dataset. Figure represents multiple views.

Traditional image segmentation

When applying traditional image segmentation methods, one has to develop task specific algorithms which is more sensitive to input data and alterations in the properties of the organ in interest. On the other hand, if the algorithm is well tuned for the task, it is able to deliver very accurate results with low computation costs. Within this study a liver segmentation algorithm was developed using the combination of Chan-Vese active contour algorithm and Region Growing. The result is presented by *Fig. 4*.

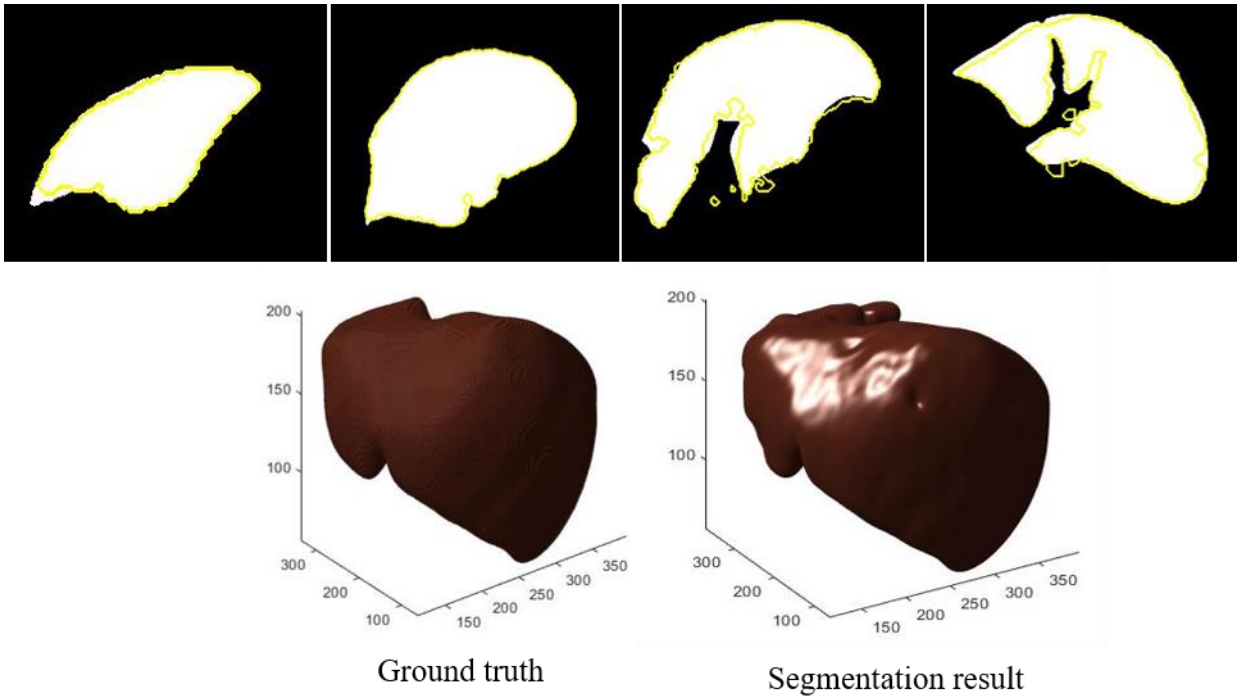

Fig. 4 Liver segmentation result by a custom developed Active Contour and Region Growing based algorithm. In the 1st row the segmentation of individual slices is presented (white is ground truth while yellow border is segmentation result) and in 2nd row 3D ground truth is compared to rendered 3D segmentation result.

Applying anatomical constraints to the output of the deep learning based segmentation, presented by Fig. 2, one can filter the parts which were falsely labeled as liver, see Fig. 5.

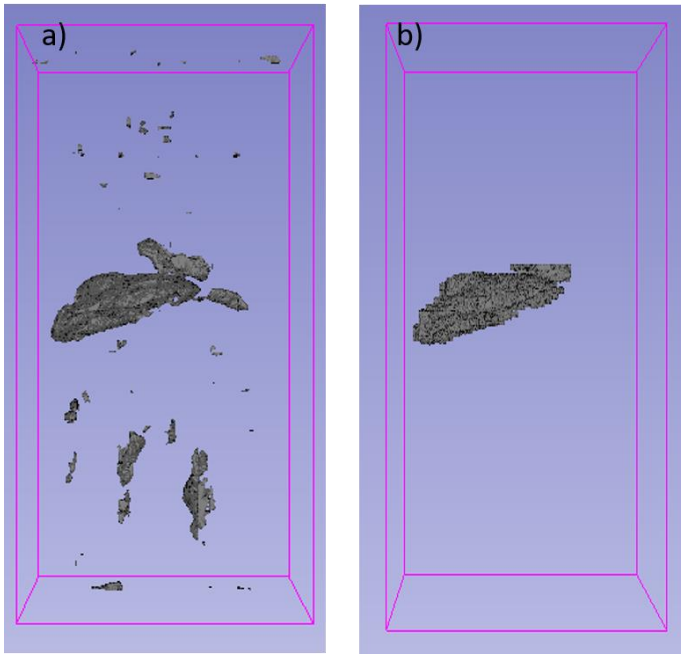

Fig. 5 a) is the result of U-Net liver segmentation; b) is the anatomically filtered a).

Chan-Vese active contour algorithm [6] was also implemented in python and used for kidney segmentation slice by slice on MR (T1) datasets. On this type of MR imaging, kidney has relative high intensity compared to its surrounding. The algorithm is based on energy minimization problem taking into account the mean intensity inside and outside the initial curve, and the curvature of the region. Problem might arise in

segmentation when organs have similar intensity values, resulting false separation. In that case, the algorithm could be tuned with a parameter to better judge phases with similar intensity values. The location of the initial rectangle is chosen based on prior knowledge, then algorithm runs automatically. *Fig. 6* demonstrates the initial state and the final shape of the evolved curve around kidney.

Fig. 6 Application of Chan-Vese active contour algorithm on MRT1 images. Initial rectangle is placed close to kidney, then curve evolves around kidney based on energy minimization principles.

The result of the active contour segmentation on two datasets are demonstrated by Fig. 7. The algorithm is relatively fast and accurate if initial rectangle is well located and background and foreground have separable intensity. The algorithm is not sensitive to noise thus no noise filtering was applied. In order to increase the robustness of the algorithm, anatomical constraints are needed to find a right location for the initial curve.

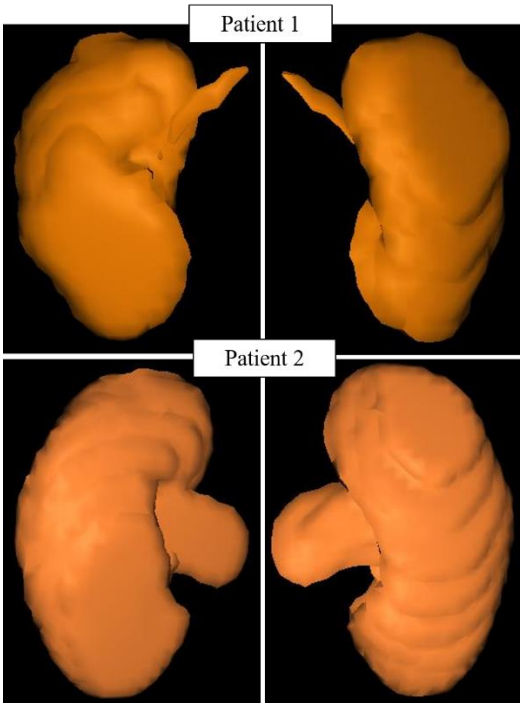

Fig. 7 3D rendered images of the 2D kidney segments resulted by the active contour algorithm. The two rows show the kidneys of two different patients. Both sides belong to the same kidney, only perspectives are different.

Conclusions

Automatic deep learning based image segmentation algorithms are quite powerful for multi-organ segmentation in case of sufficient amount of precisely labeled data. When there is no anatomical information about the organ which is aimed to be segmented, convolutional networks are favorably used thanks to their robustness. Supposing we have prior information about the location of the organ of interest, then traditional image segmentation algorithms suit well the tasks, because of their simplicity and fast running time.

Acknowledge

This work was supported by the "zMed" project (grant GINOP-2.2.1-15-2017-00083), and by the National Research, Development and Innovation Fund (grants NKFIA K-120233, K-120499, KH-125681 and KH-126688). Cs. Benedek also acknowledges the support of the Janos Bolyai Research Scholarship of the Hungarian Academy of Sciences

REFERNCES

[1] R. Gauriau, R. Ardori, D. Lesage and I. Bloch, „Multiple template deformation application to abdominal organ segmentation," in *IEEE*, New York, NY, USA, 2015.

[2] H. R. Roth, H. Oda, Y. Hayashi, M. Oda, N. Shimizu, M. Fujiwara, K. Misawa és K. Mori, „Hierarchical 3D fully convolutional networks for multi-organ segmentation," arXiv:1704.06382, 2017.

[3] V. Zografos, A. Valentinitsch, M. Rempfler, FedericoTombari and B. Menze, „Hierarchical multi-organ segmentation without registration in 3D abdominal CT images," in *International MICCAI Workshop on Medical Computer Vision*, 2016.

[4] V. A. 3, „http://www.visceral.eu/closed-benchmarks/anatomy3/," [Online].

[5] B. Menze, A. Jakab, S. Bauer, J. Kalpathy-Cramer, K. Farahani, J. Kirby, Y. Burren, N. Porz, J. Slotboom, R. Wiest and et al. „The Multimodal Brain Tumor Image Segmentation Benchmark (BRATS)," *IEEE Transactions on Medical Imaging, Institute of Electrical and Electronics Engineers*, p. 33, 2014.

[6] T. F. Chan and L. A. Vese, „Active Contours Without Edges," *IEEE Transactions on Image Processing*,10 (2), 2001.

Design Questions of the Individual Medical Implants

Péter Ficzere, PhD

Budapest University of Technology and Economics
Faculty of Transportation Engineering and Vehicle Engineering
Department of Vehicle Elements and Vehicle-Structure Analysis
Budapest, Hungary

Keywords: Bone material properties, Bone porosity, Solid CAD geometry

Abstract: Background: The spread of additive manufacturing technologies is accompanied by the development of technology, the expansion of the range of usable materials and the reduction of costs of the technology. All of these together facilitate the use of customized medical implants. Methodology: The supplementing a damaged bone or bone part is a very complex task. In order to fit the implant to its environment appropriately we need to know the geometry of the original bone, bone part, and the topology of its environment. This is usually done by re-modeling from CT scans. From CT images we can create stl file (input to 3D printers) suitable for 3D printers relatively easily, quickly with high precision. Then we can choose from multiple materials and multiple additive manufacturing technologies, taking into account different aspects (load capacity, cost, etc.). Thus we can quickly and cheaply create a load bearing implant that is geometrically matched perfectly to the patient. Results: Nowadays it is important that the mass of the implant approaches well the mass of the original bone or bone part. It is also expected that at a given load the deformations will be almost the same to the deformations of the original bone. This is the only way to protect the environment of the implant (neighboring bones) and in many cases only this can ensure people's post-operative stability. For this, however, the mechanical properties of the original bone have to be known. As well as knowing the external geometry, loads and material properties of the implant, we can optimize the bone topology. For such topology optimization we need a solid CAD geometry. Creating this CAD model from the CT scans or from stl files is more problematic in the case of complicated shapes like for example a bone geometry. Another difficulty is that the material properties of the bones are difficult to determine. In the bones' material characteristics the literature data have great deviation. Conclusion: Based on the literature data it can be stated that the different types of bones compared to each other - as well as the bones of the same type in different humans differ significantly. For this reason we performed our own measurements which also indicate that there are significant differences in the multiple loading and unloading of the same bone.

Introduction

Nowadays, additive manufacturing technologies - known as 3D printing and rapid prototyping - are spread unmatched. The main reason for the spread is that the equipment they need is getting cheaper and more accurate. The number of the type of material to be used also continues to expand as well as from a technological point of view these devices are constantly evolving [1], [2], [3], [4]. All of these together create an increasing number of areas of interest for professionals, so their application area is becoming increasingly widespread [4], [5], [6], [7], [8]. The ever-expanding use entails further development. One of the most promising areas is in medical applications [4], [9], [10]. Within this in the case of the individualized medical implants - thanks to the support of additive manufacturing technologies - took great impetus. With these methods almost any geometrical design can be realized.

In such a case, it is important that the implant that serves the replacement of missing bone or bone part is geometrically accurately aligned with the existing bone part of the patient. It is also important that the implants be constructed properly both geometrically and mechanically for implantation and fixation. An additional requirement for bone replacement implants is that after the implantation it will tolerate the stresses acting on it. To achieve this goal earlier implants were made from strong, rigid materials. This did not result in a perfect solution in the long term because the implants damaged its environment and the patient lost its stability. Thus it is necessary to design a material or topology whose elasticity closely approximates the original resilience of the given bone.

By examining the steps of design it is easy to see that questions marks emerge in many places. In elderly patients due to increased osteoporosis, the approximation of the geometry of the original bone has an extremely time and computational capacity. Determining and estimating the expected stresses is also a difficult, complex

task that makes the scaling extremely difficult. The design of geometry with adequate flexibility and load bearing capacity can be determined in principle by topology optimization. The biggest problem here is that we need to define the appropriate flexibility as a goal. However in most cases we do not have corresponding data. The data available in the literature on the modulus of elasticity are virtually inadequate to determine the objective with the correct accuracy [11], [12] because their standard deviation is extremely high. Such deviations are inexplicables from an engineering point of view. That is why it is important to test by experiments the bones' material properties exactly.

Metodology

The individually tailored medical implants can be characterized by complex geometry, material model and load cases. Dimensioning of such implants is not possible with conventional mechanical tools, by manual calculation. Therefore we need numerical simulations. For a numerical simulation we need 3D geometry (CAD model), the knowledge of the built-in environment, constraints and loads as well as the usable materials laws and material characteristics. It is important to note that these complex geometries in most cases can only be produced by additive manufacturing technologies, so the knowledge of the specialties of the manufacturing technologies and the used materials are also essential.

The 3D geometry (CAD model) must be produced by reverse engineering tools. As a starting point to a DICOM (Digital Imaging and Communications in Medicine) format CT (Computer Tomography) series can be used. Such a CT image is shown in Fig. 1. These are usually grayscale images.

Fig. 1. CT image about skull

In all planes a curve that matches the contours that is well visible can be defined. Then we create spatial geometry through these defined curves. On the same principle the missing part can be drawn to each individual layer CT images (Fig. 2).

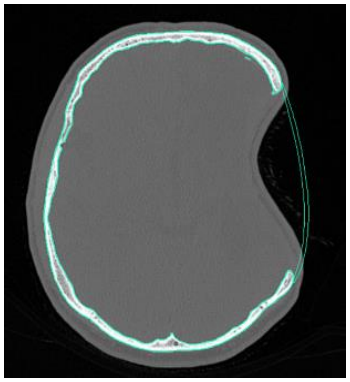

Fig. 2. Add contour in CT image

At this step care should be taken to ensure that in the image plane and in the plane perpendicular to it the implant is connected to the existing parts in a continuous manner both in tangent and curvature. It is also

important to approximate the original bone thickness and to form geometry according to the physician's required surgical requirements. Existing geometry and implant are shown in Fig. 3.

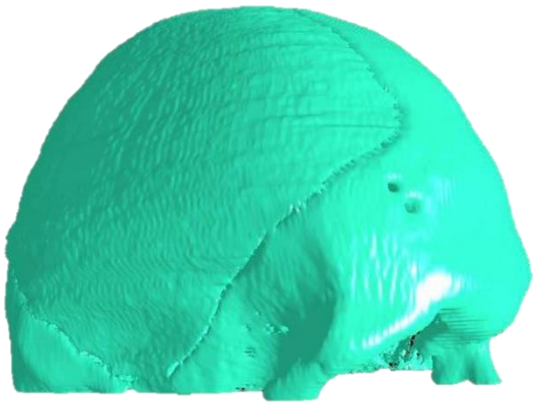

Fig. 3. 3D geometry and implant from CT scans

It should be noted that the resulting geometry is not yet a CAD model but a suitable input (STL) for 3D printers. However for numerical simulations a CAD model is required. The difference between the two versions is shown in Fig. 4.

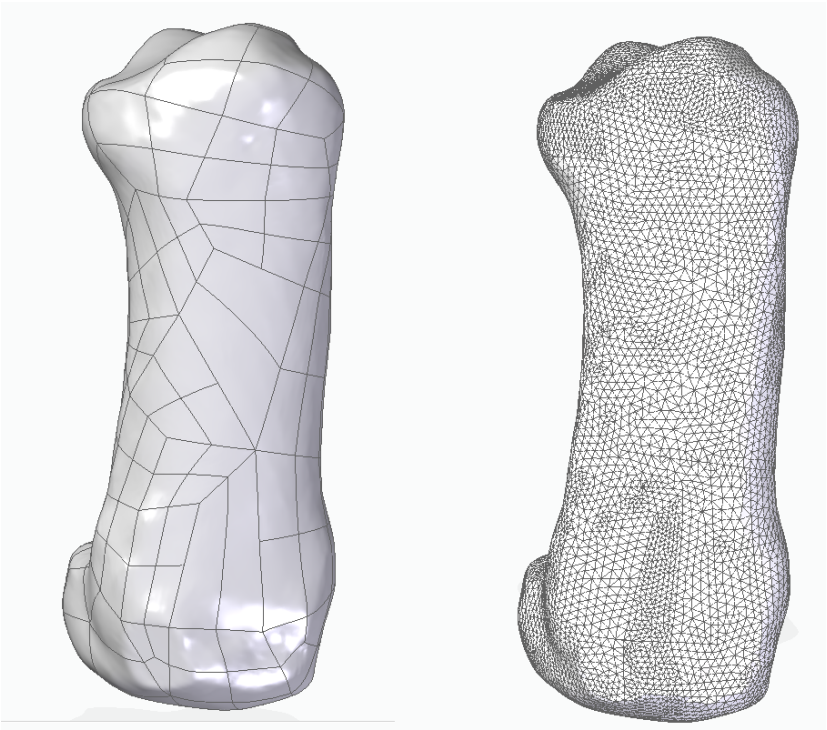

Fig. 4. CAD and stl geometry

While the surfaces of the geometry of the stl is described with small triangles in the case of CAD geometry the volume limiting surfaces are made from NURBS surface elements.

Unfortunately it is not always easy to create 3D geometry. In many cases, the contours are not clear. In fact most of the cases requiring implants need to be based on CT scans from bone of older people with significant osteoporosis. This causes serious difficulties in modeling. Problems encountered in the reverse modeling of such a strong osteoporosis patient can be found in the next chapter.

The constraints (environment), the geometry of adjacent bones can also be determined from CT scans as shown in Fig. 5.

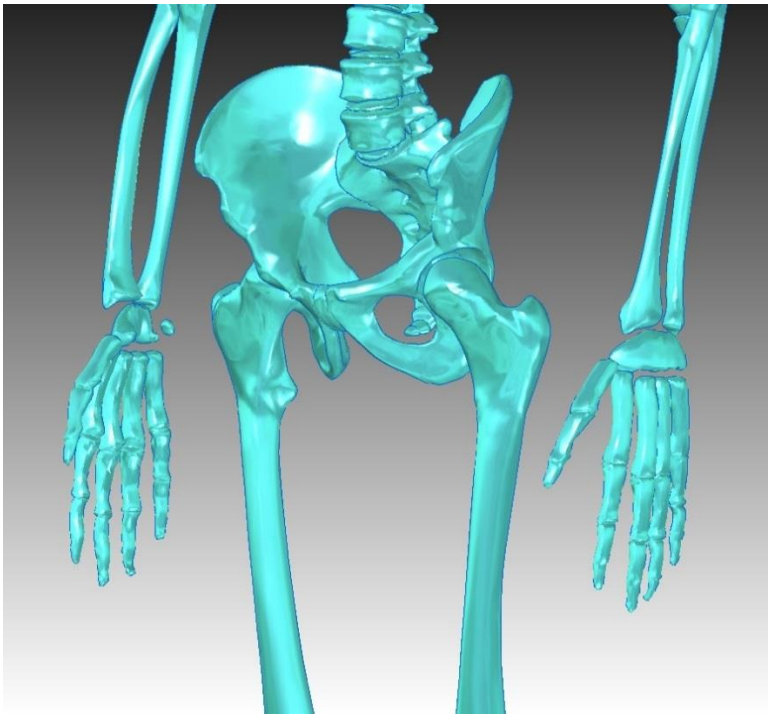

Fig. 5. Embedding environment, location of adjacent bones

Determining the loads and stresses of certain bones is also very difficult. It is questionable whether the implant dimensioning to the daily routine load or to withstand a critical load. Another interesting question is how to handle life expectancy issues. Based on the results obtained from the literature it can be seen that different authors have been defined values with significant differences for the same load case [13].

In order to design a topology wich is approximate the elasticity of the bones, we should know the bones' material properties. This is a particularly complex issue since bone and bone parts have very different mechanical properties. Mostly, referring to the literature, we "choose" a certain flexibility, but its compliance is highly questionable. Different bones, bone parts and bone types can be characterized by different flexibility [14]. In addition these values depend heavily on bone density which is also dependent on gender and age [15]. In many cases the test conditions also have a significant impact to these results. Furthermore according to some studies the same parts of the same bones undergo at the same conditions also show significant differences in the case of repeated loads.

Because of the questionable use of the literature data [16] therefore own measurement results are needed. The results of such a test are presented in the next chapter. In many cases it is not possible to use the results of own measurement so another method should be used. Such a definition could for example, the estimated bone density from the gray level of CT recordings [17].

The production of the optimized geometry can be accomplished with sufficient accuracy with one of the additive manufacturing technologies. Of course beside the proper material selection attention must be paid also to technological features such as the possibility of removing the support material, orientation dependence [18], [19] [20] and biocompatibility.

Results

As previously described, theoretically the individualized medical implants can be relatively easy to produce. However, according to the literature, fractures requiring implant insertion are 90% in people older than 50 years [15]. This also means that it has to be calculated with significant osteoporosis which can make the modeling quite complicated.

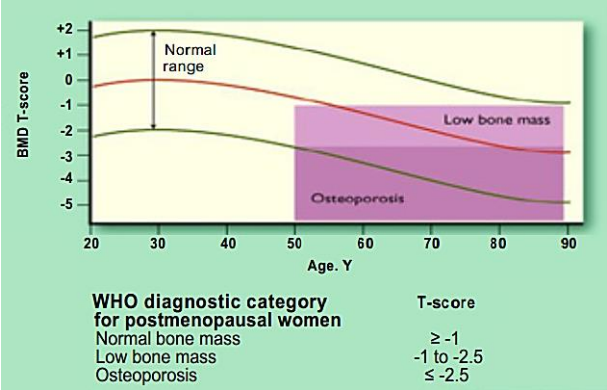

Fig. 6. Osteoporosis diagnosis by WHO [21]

Therefore I present a case different from the one presented earlier (Figs 1 and 2). In Fig. 7 a 3D model wich was taken from a CT record from an elderly man's metacarpale is shown.

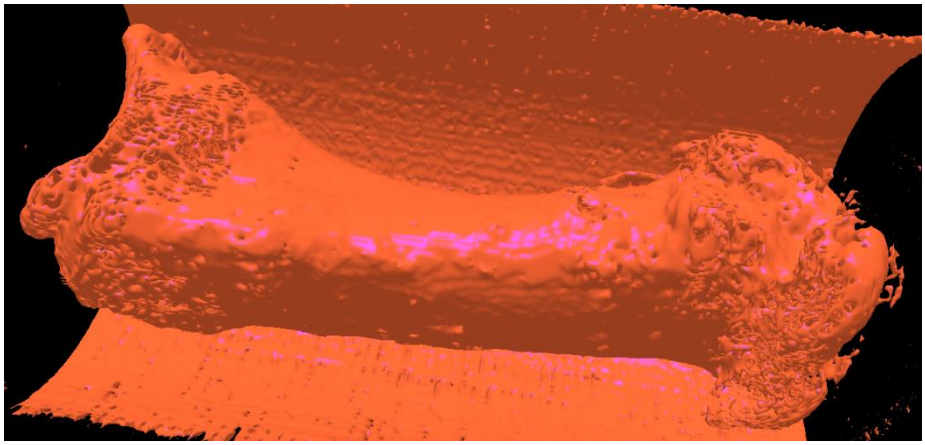

Fig. 7. 3D image of a metacarpale from CT scans

Fig. 7 shows good observation of osteoporosis in some parts of the old bone. In some parts of the bone the geometry shows very high levels of porosity. Practically in these areas the bone breaks into small pieces. This is shown from another angle of view in Fig. 8.

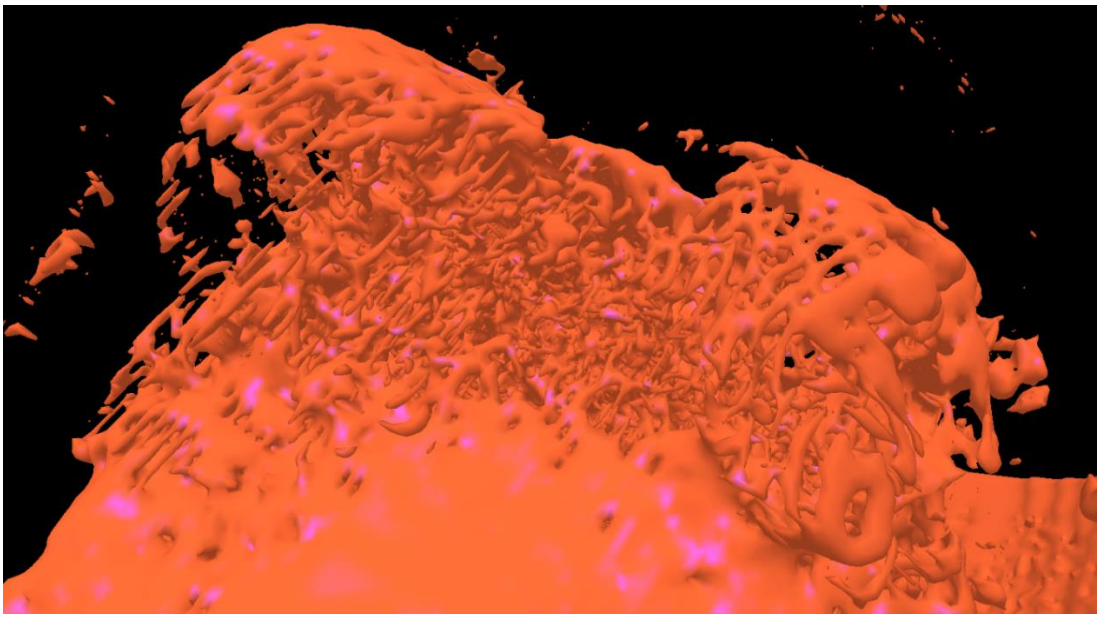

Fig. 8. Significant porosity on the aged bone

The problem is illustrated in Fig. 9 below which shows a cross section of the examined bone. The disruptions can be clearly seen in the figure as well as that it is not coherent surface should be define with a curve.

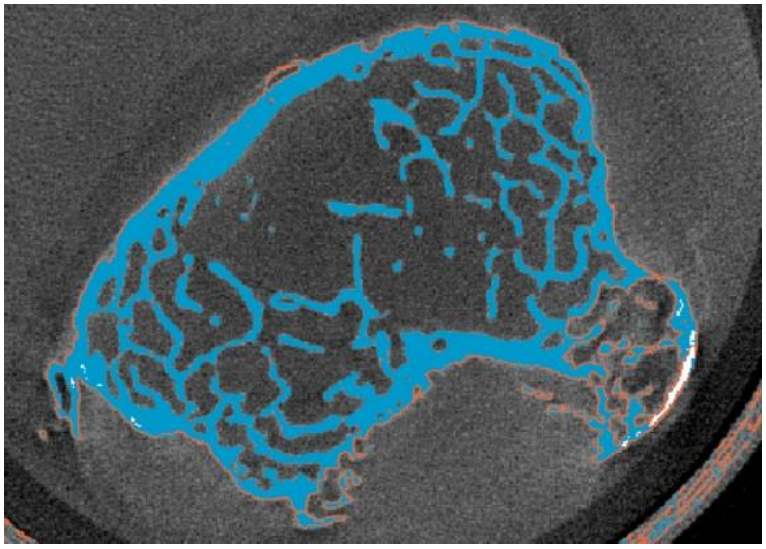

Fig. 9. Significant porosity in a cross section of an old bone

In order to perform geometry simulations and so that it can able to produced we have to model it as one piece. To achieve this it requires a lot of post-work. The result of this can be seen in Fig. 10.

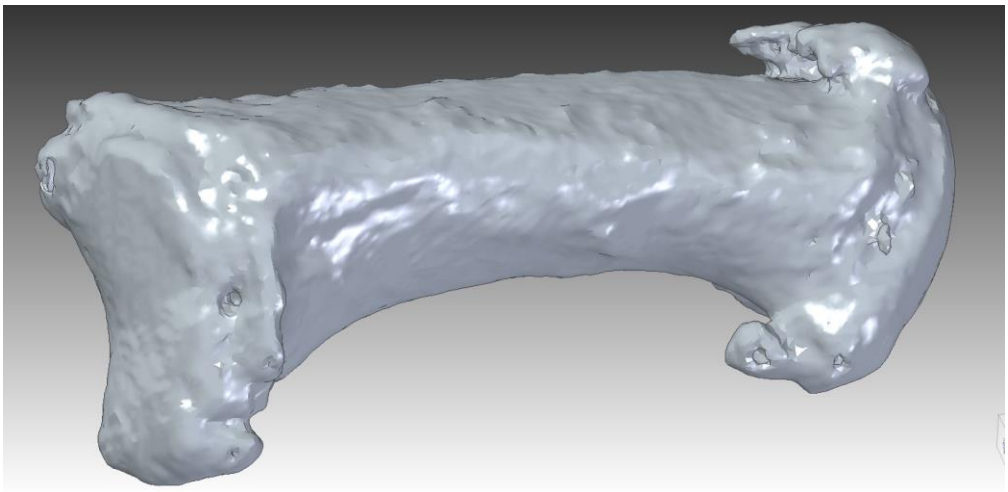

Fig. 10. A one-piece coherent model

This seems to be better but if we examine the inside of the model then the complexity of the geometry becomes clear. To perform the simulations this geometry is the target what should be approached with the finite element mesh. The meshing of such a complex hollow geometry results in extremely high computational capacity needs. A thicker section of geometry shows the inner porous portions (Fig. 11).

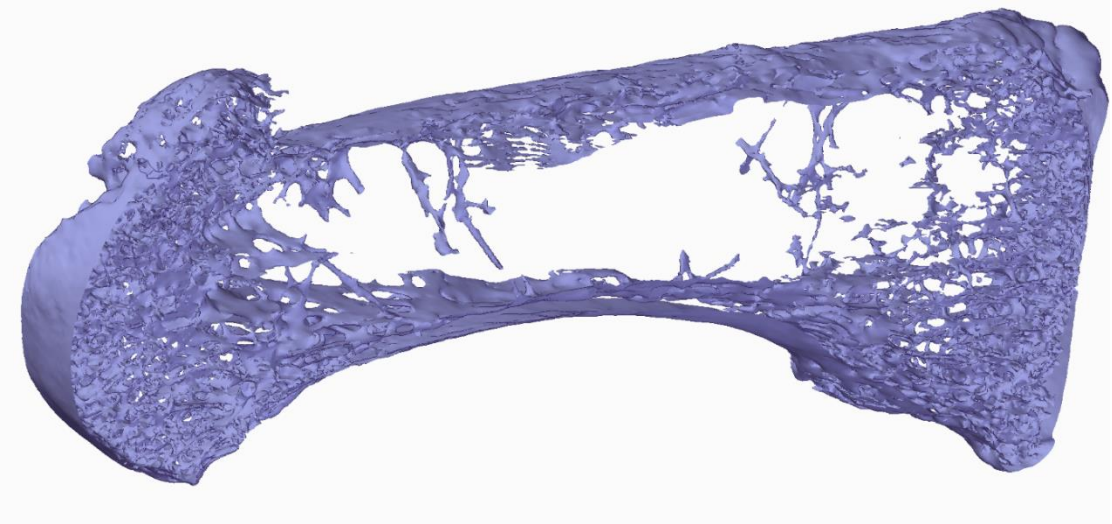

Fig. 11. Porosity of the inside of the bone

Basically, we perform simulations for two main purposes.

In the first case the determination of the exact material properties of a given bone is the goal. In this case a test on real bone was made. We try to approximate the degree of the measured deflection at 3-point bending by the applied force to the results of simulations. Here exactly the same geometry is required that can be modeling from the CT recordings. As boundary condition, as constraint, and as load we set the simulation environment according to the actual real test conditions. Then by changing the material properties by iteration steps we approach the results obtained in real model experiments, for example the values of deflections.

In the second case it is not a goal to determine the exact material properties of a given bone. In this case our aim is that the implant (plastic or metal) at the same load has the same deformation as the original bone. Therefore important is that only on the outer surfaces of the implant is identical to the original bone geometry that are in contact to its environment. This provides the right boundary conditions, constraints, and load ability for the simulation. However in this case the goal is to achieve the same deformation as the result of a given load. At this method the material properties are known and fixed (from which we will manufacture the implant) and the interior design can be modified. This requires a much simpler model since only the outer surfaces must be identical to the original, the geometry may be solid inside.

It has been discussed earlier that it is important for individualized medical implants that the elasticity of the implant closely approximates the elasticity of the original bone. To do this we need to know the mechanical properties of the investigated bone. Because this is different in every human this is either measured or reference is made to the literature. In the literature however we can find data with difference of several orders of magnitude for the same bones and bone parts. In addition multiple differences may also be found in the same bone examination [22]. This is unmanageable from an engineering point of view as these inputs are for design.

To test whether the bones material properties can can they scattered to such an extent I show the results of a 3-point bending experiments. During the study the same metacarpale has been loaded several times to determine the reproducibility of the measurement. The examined bone is an old female bone with significant osteoporosis. It is advisable to examine this type of bones as most cases which required implants this kind of bone will replace to implant. The measurement layout is a 3-point bending in which the displacement was measured as a function of the force. The results of the measurement are shown in Fig. 12.

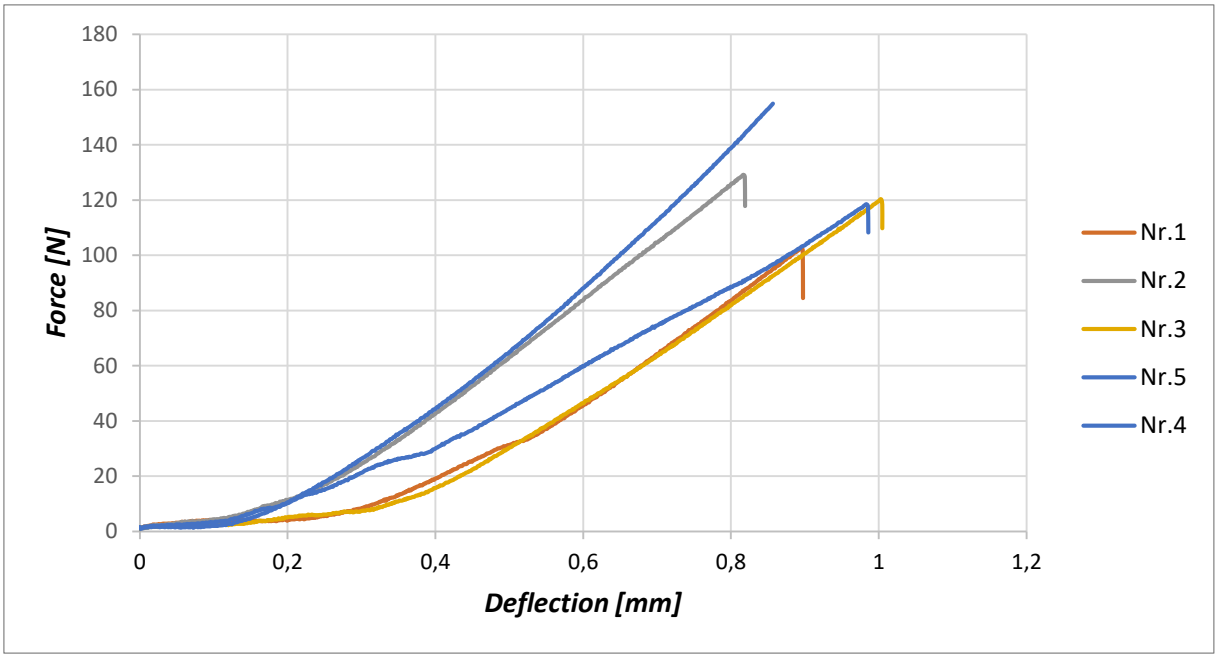

Fig. 12. Results of a 3-point bending test for a metacarpale

By examining the chart it can be seen that the curves do not really match each other. We may also think that the material is weakened due to loading and unloading but taking into account the number of measurements it can be seen that the load capacity does not depend on the load order. Since we need to define a specific goal in the simulations it is advisable to take the average of these measurements. Of course this can only be done within the measuring range where all curves can be interpreted. The result thus obtained is shown in Fig. 13.

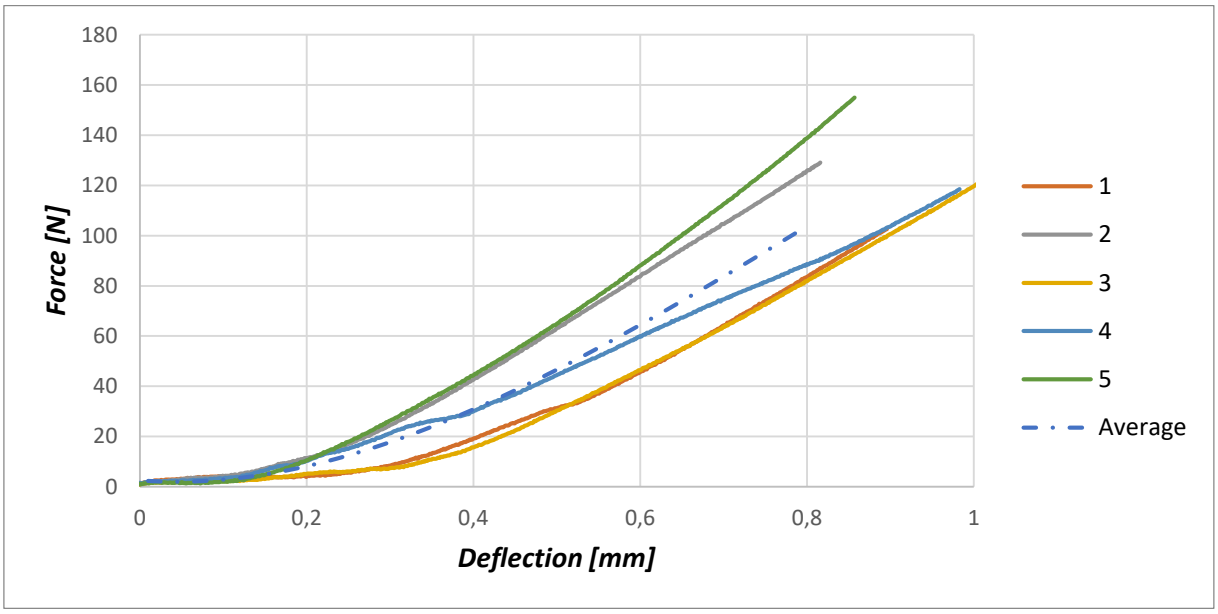

Fig. 13. Results of a 3-point bending test for a metacarpale and the average

Looking at Fig. 13 it can be seen that the measured real values may differ significantly from the average. The average values as well as the measured extremes (maximum and minimum deflection for a given load) are shown in Fig. 14.

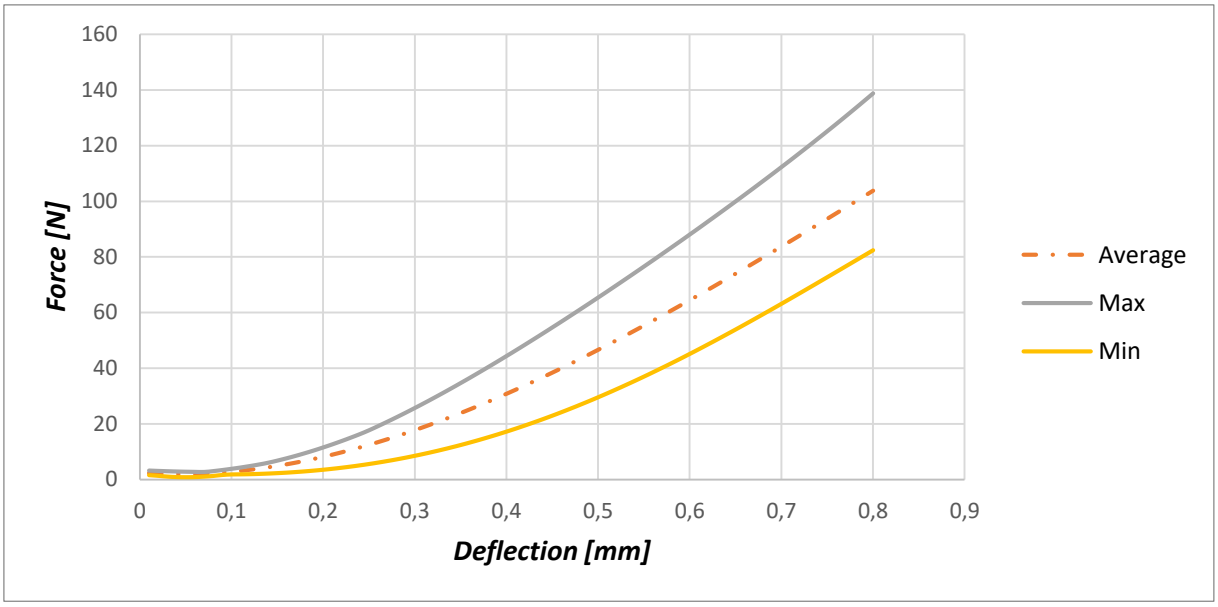

Fig. 14. Average, maximum and minimum deflection values of 3-point bending test of a metacarpale at given load

In Fig. 14 we can observe also that with the increase in the loads the differences also increase. The largest positive and negative deviations from the average value are shown in Fig. 15.

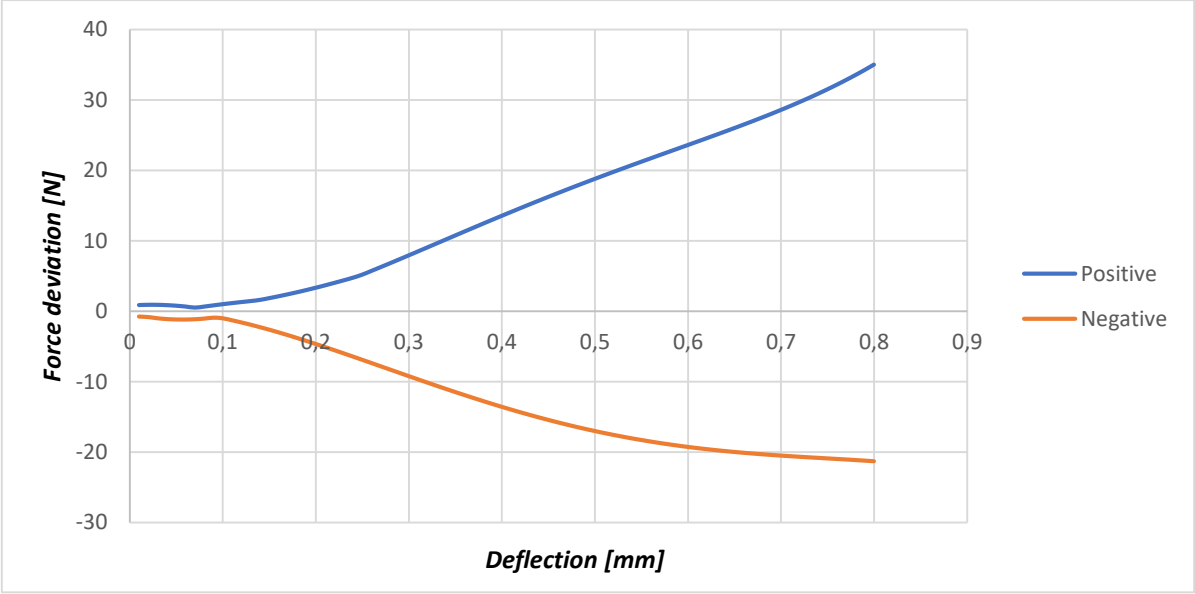

Fig. 15. The largest positive and negative deviations from the mean

Perhaps the problem is better illustrated in Fig. 16 where the difference between the measured extreme values can be seen as a function of deflection.

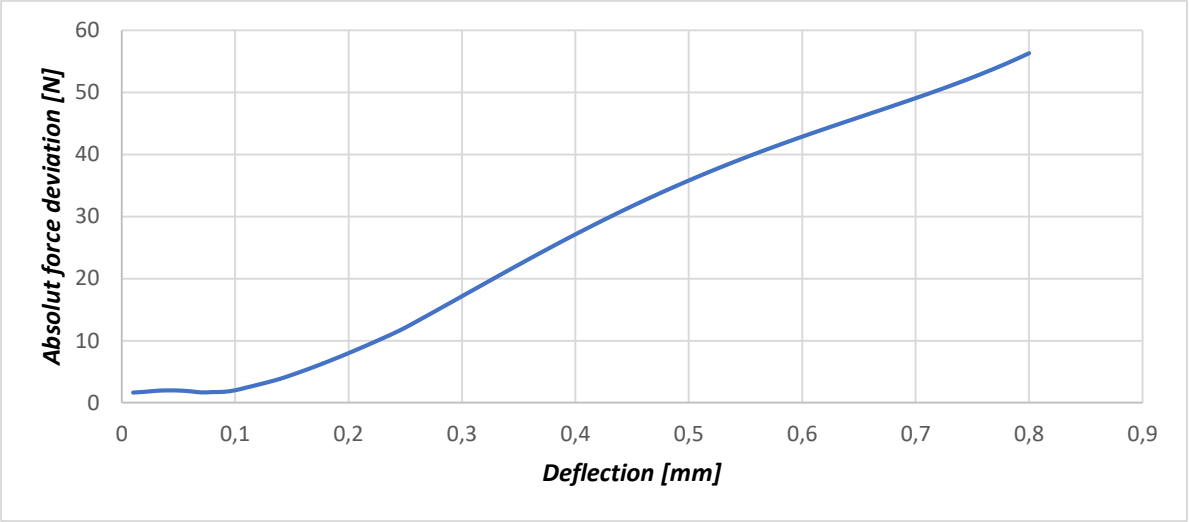

Fig. 16. Sum of the maximum deviations to the mean value

Examining Fig. 16 it can be seen that with the increase of the degree of deflection there is an increasing deviation in the various measurements. The results are also interesting if the differences are measured as a percentage of the measured values.

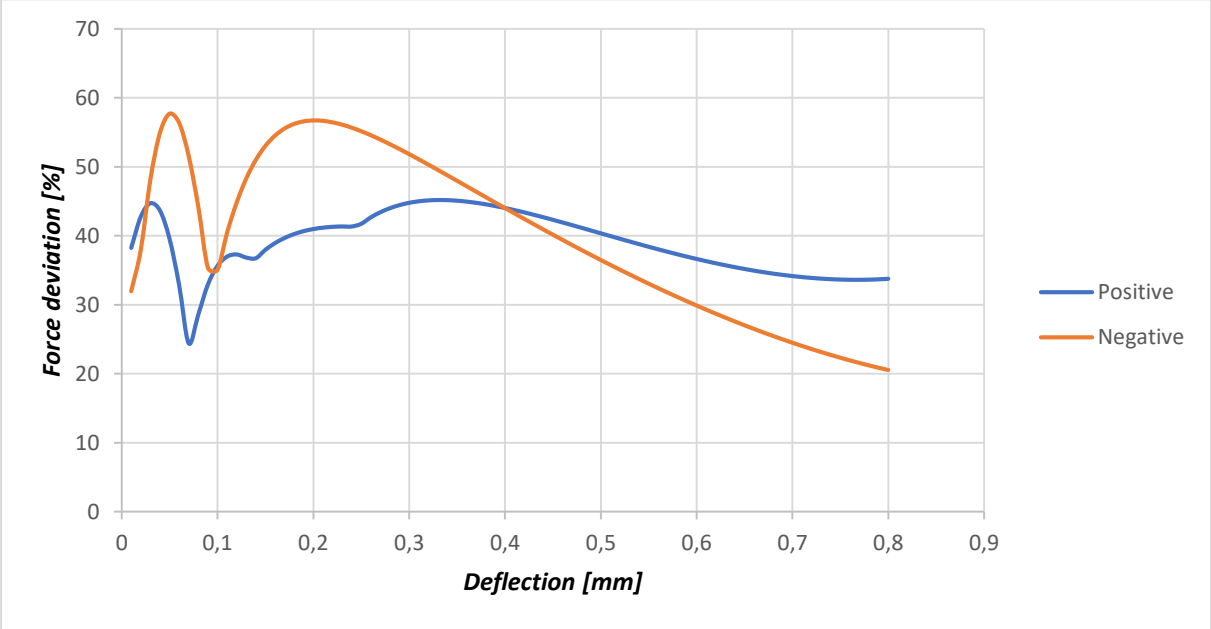

Fig. 17. Percentage deviations from the average value

Conclusion

In summary it can be stated that in the case of individualized medical implants modeling of geometry in only a small percentage of cases is simple. The reason for this is that the bone fractures requiring the implant are approximately 90% of the patients have osteoporosis. In such cases the determination of the bone material properties becomes very difficult.

When designing implants it is essential to determine the elasticity of the bones to that the environment of the implant will not be damaged later and to be ensured the patient's stability. However it is clearly demonstrated that the reproducibility of values of measurable material properties for bones is inappropriate. This means that the same bone in the same conditions is significantly different. These differences may even

reach plus-minus 40%. Thus, even in the case of the appropriate accuracy of simulation and geometry the uncertainty remains very high.

Aknowledgement

This project results have been realized with a subsidy of the National Research Development and Innovation Office from the fund of NKIH. The title of the project is “Development of the New Generation of Production Technology for Individual Medical-Biological Implantation and Tools”. Project identification No.: NVKP_16-1-2016-0022. The elaborators express their thanks for the support.

REFERENCES

[1] Ficzere P, Borbás L, Falk Gy, Orvosi implantátumok méretezéséhez szükséges anyagmodellek additív gyártástechnológiák alkalmazása esetén, BIOMECHANICA HUNGARICA 10:(2) pp. 57-58. (2017)

[2] Ficzere P, Borbás L, Falk Gy, Szebenyi G, Experimental determination of material model of machine parts produced by SLS technology, In: Francesca Cosmi (szerk.), Proceedings of 34th Danubia-Adria Symposium on Advances in Experimental Mechanics. 207 p., Trieste, Olaszország, 2017.09.19-2017.09.22. Trieste: Università degli Studi di Trieste, 2017. pp. 161-162., (ISBN:978-88-8303-863-1)

[3] Ficzere P, Szebényi G, Lovas L, Borbás L, SLS eljárással elérhető anyagjellemzők egyénre szabott orvosi implantátumok méretezéséhez, GÉP LXVIII:(3) pp. 62-65. (2017)

[4] Ficzere P, Borbás L, Gyors prototípus anyagok orvosi alkalmazásának lehetőségei, kérdései, In: Borbás Lajos (szerk.), Korszerű anyagok és gyártástechnológiák alkalmazása a gyógyászatban. Tatabánya, Magyarország, 2014.05.30-2014.05.31., Magyar Biomechanikai Társaság, 2014. p. 17., (ISBN:978-963-88981-2-8)

[5] Ficzere P, Borbás L, Török Á, Usage of rapid prototyping in vehicle manufacturing, In: Stanislaw Borkowski, Dorota Klimecka-Tatar (szerk.), Toyotarity: Elements of the organization's mission. 225 p., Dnepropetrovsk: Yurii V Makovetsky, 2011. pp. 182-193., (ISBN:978-966-1507-70-7)

[6] Ficzere P, Horváth E, Török Á, Rapid prototyping as a road safety instrument, In: Kibédi-Varga Lajos (szerk.), CERSC 2012: Conference on Effectiveness of Road Safety Campaigns. 178 p., Magyarország, 2012.05.08-2012.05.10. Budapest: Premium Relations, 2012. pp. 144-149., (ISBN:978-963-08-4186-3)

[7] Ficzere P, Borbás L, New Application of 3D Printing Method for Photostress Investigation, MATERIALS TODAY: PROCEEDINGS 3:(4) pp. 969-972. (2016), 32nd DANUBIA ADRIA SYMPOSIUM on Advanced in Experimental Mechanics.

[8] Horváth Á M, Ficzere P, Rapid prototyping in medical sciences, PRODUCTION ENGINEERING ARCHIVES / ARCHIWUM INŻYNIERII PRODUKCJI 8:(3) pp. 28-31. (2015)

[9] Szűcs N A, Szép G, Szabó F, Kovács N K, Korszerű gyártástechnológiák szerepe az egyszer használatos orvostechnikai eszközök fejlesztésében, POLIMEREK 2:(8) pp. 232-237. (2016)

[10] Molnár B, Fekete K, Borbás L, Paput L, Graft lehetőségek a fülkagylóképzésben, In: Borbás Lajos (szerk.), Korszerű anyagok és gyártástechnológiák alkalmazása a gyógyászatban. Tatabánya, Magyarország, 2014.05.30-2014.05.31.,Magyar Biomechanikai Társaság, 2014. Paper 16. 5 p., (ISBN:978-963-88981-2-8)

[11] Lakatos É, A csont mikroszerkezetének mechanikai viselkedése fogászati implantátumok környezetében, PhD értekezés

[12] L. Cristofolini, M. Viceconti: Mechanical validation of whole bone composite tibia models, Journal of Biomechanics 33 (2000), pp 279-288

[13] Simonovics J, Orosz P, Bujtár P, Egyedi teherviselő állkapocs implantátum optimalizálásának lehetőségei, GÉP 67:(7-8) pp. 85-88. (2016)

[14] J-Y Rho, L Kuhn-Spearing, P Zioupos, Mechanical properties and the hierarchical structure of bone, Medical Engineering & Physics 20 (1998) pp. 92–102

[15] M V Kumar Reddy, BKC Ganesh, KCK Bharathi, P ChittiBabu, Use of Finite Element Analysis to Predict Type of Bone Fractures and Fracture Risks in Femur due to Osteoporosis, Journal of Osteoporosis and Physical Activity, Volume 4 • Issue 3 • 1000180, ISSN: 2329-9509, doi: 10.4172/2329- 9509.1000180

[16] Ficzere P, Egyedi orvosi implantátumok méretezési problémái, GÉP LXVIII:(3) pp. 58-61. (2017)

[17] D C Wirtz, N Schi!ers, T Pandorf , K Radermacher, D Weichert, R Forst: Critical evaluation of known bone material properties to realize anisotropic FE-simulation of the proximal femur, Journal of Biomechanics 33 (2000) 1325-1330

[18] Ficzere P, Borbás L, Csontok anyagjellemzőinek közelítése a gyártástechnológiai paraméterek módosításával 3D nyomtatás esetén, BIOMECHANICA HUNGARICA 10:(2) p. 22. (2017)

[19] Győri M, Ficzere P, Use of Sections in the Engineering Practice, PERIODICA POLYTECHNICA-TRANSPORTATION ENGINEERING 45:(1) pp. 21-24. (2017)

[20] Ficzere P, Orthotrop anyagmodell alkalmazása additív gyártástechnológiával előállított alkatrész méretezése során [Usage of orthotrop material law for additive manufacturing in part design], GÉP LXVII:(5-6) pp. 78-81. (2016)

[21] Juckerman JD (1996) Hip fracture. N England J Med 334: 1519-1525.

[22] Luca Cristofolini, Marco Viceconti: Mechanical validation of whole bone composite tibia models, Journal of Biomechanics 33 (2000) 279-288.

Brain Tumor Segmentation in MRI Data

Petra Takács†*, Andrea Manno-Kovacs†*
†Machine Perception Research Laboratory, MTA SZTAKI, Budapest, Hungary
* Pázmány Péter Catholic University, Faculty of Information Technology and Bionics, Budapest, Hungary

Keywords: visual saliency, 3D medical image segmentation, convolutional neural networks

Abstract:
This paper proposes a brain tumor segmentation method based on visual saliency features on MRI image volumes. The proposed method uses a novel combination of multiple MRI modalities and highlights the potential tumors by applying a healthy template generated from the annotated database slices without tumors. The introduced method proposes a saliency model that includes color and spatial features and as a novel contribution, also incorporates information about the relation of neighboring slices. Based on the saliency map, the outline of the tumor is detected by a region-based active contour method. Moreover, the proposed method is also combined with convolutional neural networks to reduce the networks' eventual overfitting which may result in weaker predictions for unseen cases. The proposed methods were tested on the BRATS2015 database, and the quantitative results showed that hybrid models (including both trained and handcrafted features) can be promising alternatives to reach higher segmentation performance.

Introduction

Gliomas are the most frequent primary brain tumors in adults [1], comprising about 30 per cent of all brain tumors and central nervous system tumors. Being highly malignant, this type covers 80 per cent of all malignant brain tumors. In case of patients with such brain tumors, the role of noninvasive imaging techniques are even more important, as repeated tumor biopsies have high risk. Therefore, continuous monitoring using 3D image modalities (CT, MRI) is a widely applied tool.

When categorizing state-of-the-art tumor segmentation algorithms, we can divide them into two broad families [2]. *Generative* models use detailed prior information about the appearance and spatial distribution of multiple different tissues, including anatomical and domain-specific knowledge. They usually also perform brain tissue segmentation [3], [4]. In our proposed model we followed a similar approach as in [3] and we built a healthy template for the applied image scans (*T2* and *FLAIR* components in our case). They can handle unseen images efficiently, but they strongly rely on the registration step.

The other large group is *discriminative* models, using annotated training images and directly learning the characteristics of different segmentation labels without any prior domain knowledge [5], [6]. To cover intensity and shape variations of tumors, they require huge amount of training data to extract tumor features thoroughly. Nowadays, deep learning methods are the most popular models of this group, using convolutional neural networks. Different network architectures, such as U-Net [7] or cascaded anisotropic networks (WTNet) [8] are applied for training segmentation models using 2D or 3D interpretation. However, the disadvantage of these methods is still their strong dependence on the training data, e. g., they cannot handle images with differing imaging protocols from the ones used for acquiring the training data.

To compensate for the mentioned drawbacks, one solution might be to use a mixed generative-discriminative model to fuse handcrafted features and learning.

From a medical point-of-view, the existence of tumors may support diagnosis, therefore these objects may function as the ROI of the image. This motivates to consider tumors as salient regions in the image, and highlight them by applying a visual saliency model. Our proposed algorithm follows this direction and, inspired by [9], constructs a saliency model using handcrafted features. The referred saliency-based detection algorithm [9] is based on a pseudo-coloring scheme using *FLAIR*, *T2* and *T1c* sequences respectively as RGB channels, followed by a bottom-up color and spatial distance calculation to highlight tumor areas as salient regions in the image.

In this paper, a novel pseudo-color image is introduced, calculating channels as difference images between a specific image patch and a healthy image template built up using the healthy slices of the database for *FLAIR* and *T2* sequences. Beside calculating color and spatial distance in the image patch, information between brain volume slices is also incorporated in the proposed saliency function, exploiting the connection between

neighboring slices concerning the location, size and shape of the tumor. The calculated saliency map estimates the location of the tumor. To produce a more accurate tumor outline, a region-based active contour step [10] is also performed.

As a proof-of-concept step the proposed saliency map is combined with trained convolutional neural networks (U-Net and WT-Net) by applying a weighting function for the saliency map and the network's prediction map. The quantitative results on the Multimodal Brain Tumor Image Segmentation Benchmark (BRATS) 2015 [2] showed that the hybrid models (including both trained and handcrafted features) can be promising alternatives to reach higher segmentation performance.

Visual saliency based tumor segmentation

Pseudo color model

We construct a color image from the available MRI sequences. Improving the color model of [9] we have also calculated a difference image for the *FLAIR* and *T2* scans in the BRATS2015 database. By analyzing the annotated ground truths, we selected slices without marked tumor regions. For all axial slices, available healthy scans were collected and we constructed the healthy mean templates HM_{FLAIR}, HM_{T2}. The proposed color model has the following form:

$$\begin{aligned} &\mathbf{R} : FLAIR, \\ &\mathbf{G} : T2 * \alpha - HM_{T2} * \beta, \\ &\mathbf{B} : FLAIR * \alpha - HM_{FLAIR} * \beta, \end{aligned} \quad (1)$$

where we selected $\alpha = 1.5$ and $\beta = 0.2$ based on the experiments. As a simple registration, the brain area (pixels with non-zero values) in the template is fitted to the brain region in the actual image. To further enhance local contrast, the pseudo*RGB* image is transformed to the CIE $L*a*b*$ color space, which is later used for saliency calculation.

Saliency map for ROI estimation

To build the saliency model, [9] advised to apply color difference and spatial difference in a block-based processing system. To achieve this, first the image slice was rescaled to 256×256. Then, the rescaled image was decomposed into nonoverlapping blocks with size $k \times k$, where w is a multiple of k. Therefore, saliency calculation was performed for $w/k \times w/k$ patches and the S_c color difference feature for R_i patch was computed as:

$$S_c(R_i) = \sum_{j,j \neq i} \sqrt{(R_i^{\overline{L}*} - R_j^{\overline{L}*})^2 + (R_i^{\overline{a}*} - R_j^{\overline{a}*})^2 + (R_i^{\overline{b}*} - R_j^{\overline{b}*})^2}, \quad \forall i, j \in \{1, \ldots, (w/k \times w/k)\}. \quad (2)$$

The color difference was calculated for each $L*a*b*$ channels, and $R_i^{\overline{ch}}$ marks the mean value for *ch* channel, which represents the i^{th} image patch R_i.

Motivated by the human observation that tumors are spatially concentrated objects, close to a spatially salient area, the probability is high to find further salient regions. On the other hand, regions further from the salient area have a smaller probability to be salient. Therefore, spatial distance feature was incorporated for saliency calculation:

$$S_{cs}(R_i) = \sum_{j,j \neq i} \frac{1}{1 + d(R_i, R_j)} \times S_c(R_i), \quad (4)$$

where $d(R_i,R_j)$ is the Euclidean distance of the mean spatial coordinates of R_i, R_j patches. The S_{cs} saliency map is then scaled back to its original size saliency model scale-invariant to local feature sizes, the S_{cs} (denoted by $\hat{S}_{cs}$), using bilinear interpolation. To make the saliency model scale-invariant to local feature sizes, the S_{cs} color-spatial saliency is calculated for different block sizes. 8 × 8 and 16 × 16 blocks are used for saliency calculation: $S_{cs} = \sum_{k=8,16} r^k \times \hat{S}_{cs}^k$, where r^k is the weighting parameter for the color-spatial based saliency map of different sizes. By following the recommendations of [9], $r^k = 0.5$ is applied.

Beside these features, we added 3D spatial information and the color-spatial saliency model was further extended to extract salient information from neighboring slices. Motivated by the fact that the location, size and shape of the tumor is quite similar in neighboring slices, we calculated the final saliency map as a weighted fusion of the actual (S_{cs}^{a}), previous (S_{cs}^{p}) and next (S_{cs}^{n}) slice's color-spatial saliency. The proposed saliency map looks as follows:

$$S = w^p \times S_{cs}^{p} + w^a \times S_{cs}^{a} + w^n \times S_{cs}^{n}, \qquad (6)$$

where w^p, w^a, w^n denote the weights for the different slices, after extensive testing, $w^a = 0.4$ and $w^p = w^n = 0.3$ were set.
Finally a 25×25 mean filter was applied on the calculated S saliency map to get a smoother final estimation.

Active contour based tumor outline detection
The original method [9] highlights tumor regions, however it sometimes fails for healthy slices. In such cases, the calculated saliency map has balanced values for the whole brain region, falsely emphasizing large healthy areas. To avoid such errors, we add a spatial checking step before the tumor outline detection. The saliency map is first binarized by applying an adaptive threshold motivated by the original paper:

$$T_\gamma = \frac{\gamma}{M \times N} \sum_{x=0}^{M-1} \sum_{y=0}^{N-1} S(x, y) \qquad (7)$$

where $\gamma = 3.55$ is set, as proposed in [9].

The area of the foreground in the binarized image (the estimation of the potential tumor) and the area of the whole brain region is measured, and if their ratio exceeds a T_r threshold ($T_r = 0.425$, set based on the experiments), then the salient area is filtered out, and the slice is claimed to include no tumor. The ratio was set based on the analysis of the annotated tumor sizes and their rate to the coherent brain regions in the BRATS2015 database. The saliency based tumor estimation gives a rough localization of the ROI (blue contour in Fig. 1), however the fine details of the object outline are usually missed. To detect the complex shapes more accurately we used a region based active contour method [10]. Fig. 1 shows the results of the tumor outline detection, blue marking the initial contour, which is the binarized estimation of the color-spatial saliency map, red is the result of the iterative Chan-Vese active contour method and green shows the ground truth. We checked the final active contour detection for overly large areas, rejecting areas exceeding the mentioned T_r ratio. After running the segmentation algorithm for all the slices of a volume, we added a final drop-out step to eliminate false positive hits. Tumor candidates were followed throughout neighboring slices, and the number of slices (length of the chain) with the tumor was counted. Finally, only the detection of the longest chain was kept. If a tumor appeared only on a few slices, then it was assumed to be false and deleted.

Fusion of deep learning based predictions and handcrafted saliency maps
As it was discussed in the Introduction, nowadays neural networks are widely used for brain tumor segmentation. However, adapting deep learning methods to new data can be hard, requiring lengthy retraining, making real world application very challenging. In case of novel data, they have to be retrained, which makes real world application or software implementation very challenging. This motivates the idea to fuse a *generative*, handcrafted feature-based model and a *discriminative* learning based technique.

As a proof-of-concept, we have fused our saliency-based model with two, state-of-the-art network architectures, the U-Net [7] and the WT-Net [8]. The U-Net introduces a convolutional network for end-to-end image segmentation, resulting in a segmentation map. The first part of the network is a contractive part, highlighting the image information, while the second part is creating a high-resolution segmentation map.

The U-Net was very successful, when processing medical image data.

In [8] a cascade of CNNs were introduced to segment brain tumor subregions sequentially. The complex segmentation problem is divided into 3 binary segmentation problems: WNet segments the whole tumor, its output is a bounding box, which is used as input of the second network, called as TNet, to segment the tumor

core. Finally, its output bounding box is applied as input for ENet to detect enhancing tumor core. As in our case we only concentrate on the whole tumor, and we use the implementation of WNet/TNet, called WT-Net, from the NiftyNet [11] platform.

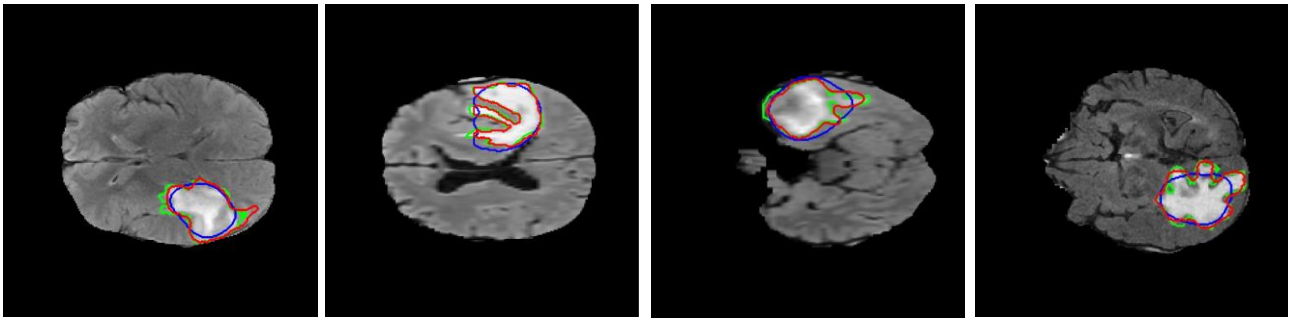

Fig. 1. Tumor contour detection using the Chan-Vese method; blue is the thresholded, binary tumor estimation of the color-spatial saliency map, red is the improved result of the active contour step, green is the ground truth tumor outline.

To exploit the benefits of both approaches, the proposed S saliency map (Eq. 6) is fused with the prediction map, calculated by the neural network (denoted by P_U and P_{WT} for U-Net and WT-Net respectively). As a shallow convolution, the two maps are fused with a weighting function:

$$S\{_{U,WT\}} = \delta \times S + (1 - \delta) \times P_{\{U,WT\}}, \qquad (8)$$

where $\delta = 0.5$ was applied for U-Net, and $\delta = 0.5$ and $\delta = 0.25$ were tested for WT-Net. According to our experiences, while saliency based algorithms have high precision value and lower recall, neural networks behave inversely with higher recall than precision. Moreover, the performance of neural networks with good generalization skill can be further improved for unseen, special cases by fusing them with handcrafted features.

The examples in Fig. 2 illustrate the performance, the first two samples are generated by U-Net, third and fourth samples by WT-Net. In the first sample, the U-Net separates the tumor into 2 parts, while the saliency-based method gives a more homogeneous estimation, therefore their combination detects the whole tumor in one piece; in the second sample, both the U-Net and the saliency-based approach detect only one blob, thus their fusion is able to localize both areas. WT-Net achieves high accuracy values (see Table I in the Experimental evaluation), still its performance can be slightly increased by combining it with the saliency-based method, i.e. tumors with complex shape (third row). The fourth example shows that sometimes the estimation is quite similar for both the neural network and the saliency map, therefore their combination will also propagate the falsely detected blobs. Although the marked areas look suspicious even on the *FLAIR* image scan, according to the ground truth, only one tumor is present on this slice. Nevertheless, the hybrid model estimates the real tumor's shape more accurately.

Experimental evaluation

We performed the evaluations on the BRATS2015 dataset [2], which includes altogether 220 HGG volumes and 54 LGG volumes (HGG and LGG stand for high-grade and low-grade glioma respectively) with *T1*, *T1c*, *T2* and *FLAIR* sequences. Each volume has the size of 240×240×155 voxels with pixel-wise ground truth. During the evaluation we used the axial view, i.e., 155 slices with a size of 240 ×240 pixels for each volume.

In our evaluation, we used a publicly available implementation of the U-Net. All available sequences (*T1*, *T1c*, *T2* and *FLAIR*) were used for training with 16-bit slice images and 8-bit ground truth labels. The 90% of all BRATS2015 image volumes was randomly selected for training; the remaining 10% was used for testing. In the training part, 10 epochs were performed, the learning rate was set to $1e-4$, the loss type was binary cross entropy. From the training set 20% was randomly selected for validation. Two training runs were performed for the U-Net with two randomly partitioned training/test sets (Test set I and II). The performance was quantitatively evaluated for the randomly selected 22 HGG volumes. For comparison, the same volumes were evaluated for the original saliency-based method [9], the WT-Net based network [8] and for the proposed method as well.

We also evaluated the Test set I using the NiftyNet [11] implementation of the WT-Net. Similarly to the U-Net, WT-Net was also trained with 90% of the available sequences, learning rate was set to $1e{-}4$, the applied loss type was Dice, and the training was performed in 20000 epochs. Again, 20% of the training volumes were randomly separated for validation.

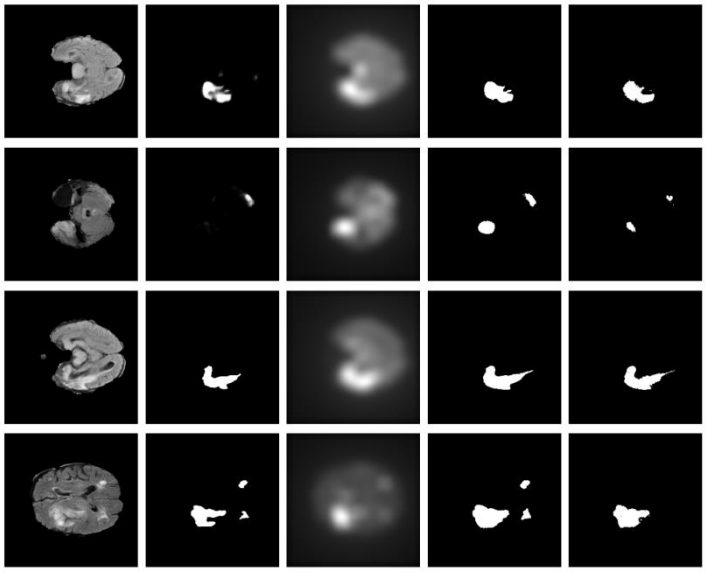

Fig. 2. Fusion of neural networks and saliency-based features, row 1-2: UNet; row 3-4: WT-Net; (a) *FLAIR* image slice; (b) result of the neural network based segmentation; (c) calculated saliency map; (d) binary segmentation result achieved by the 0.5−0.5 weighted combination (Eq. 8); (e) the binary ground truth for the whole tumor from BRATS2015.

Altogether, in one test set 3410 slices were evaluated for the WT-Net and its combined version with the saliency, and 6820 slices in two test sets were used for testing the original method, the proposed method, the U-Net based network and the U-Net – saliency combination.

At the end a 3D representation with Gauss- smoothing was made to see the separated brain tumors together, instead of slice by slice. Besides the proposed method and the ground truth, U-Net, WT-Net and U-Net + Proposed have been visualized (Fig. 3).

We have calculated different quantitative measures: Precision, Recall, F_β (β=0.3) and True Negative Ratio (TNR).

Quantitative results are given in Table I. As it can be seen, the proposed method outperforms the original approach by receiving higher precision and recall values. Out of the neural networks, WT-Net achieves higher performance than U-Net, however it should be mentioned, and that WT-Net was designed specifically for such brain tumor detection tasks (targeting the BRATS2017 dataset).

As for the fusion of U-Net and saliency-based methods, we have also tested 1/3 – 2/3 and 2/3 – 1/3 weightings, however, the results were just slightly worse than the performance of 0.5 – 0.5 weighting, therefore we only included the numbers for the weighting with the highest performance. Moreover, by fusing the calculated saliency map with the prediction map of the selected neural networks, higher precision, F_β and TNR can be achieved. Please note, that the proposed method usually performs with lower recall and higher precision, which means that usually it gives smaller, but more precise estimations.

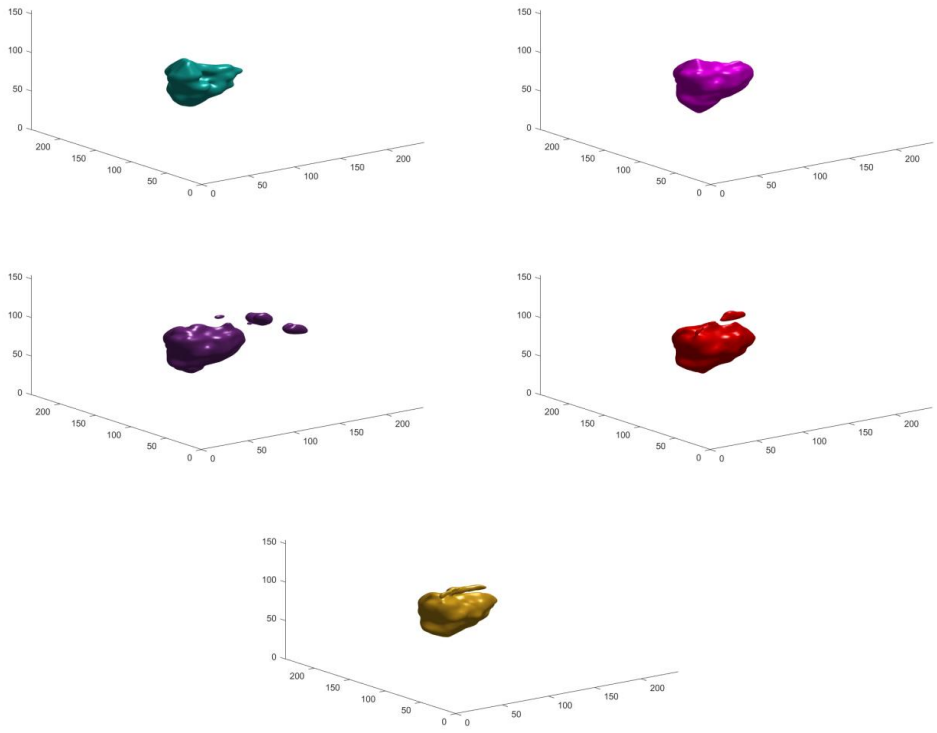

Fig. 3. 3D representation of a brain tumor with the different approaches; row 1: Proposed (turquoise) and Proposed + U-Net (magenta); row 2: U-Net (purple) and WT-Net (red); row 3: Ground Truth with yellow.

Two sample images are shown in Fig. 3 for the compared original and proposed methods, with 0.5 – 0.5 weighting for the hybrid models. The tumors are well localized by every algorithm; however their complex shapes are most accurately segmented by the fusion models.

To summarize the discussion, the results show that the combination of trained networks and handcrafted feature based techniques gives promising segmentation results; the fusion achieves higher precision and F_β values than the performance of the network alone.

Table 1.
QUANTITATIVE RESULTS ON BRATS2015 DATASET FOR THE ORIGINAL ALGORITHM, THE PROPOSED METHOD, U-NET, WT-NET AND THEIR WEIGHTED COMBINATION WITH THE PROPOSED APPROACH. BOTH TEST SETS CONSIST OF 22 HGG VOLUMES.

Algorithm	Test set I				Test set II			
	Precision	Recall	F_β	TNR	Precision	Recall	F_β	TNR
Original [9]	0.5949	0.2497	0.5340	0.8547	0.5766	0.2072	0.5026	0.8520
Proposed	0.8535	0.5328	0.8131	0.9738	0.8636	0.5093	0.8167	0.9756
U-Net [7]	0.6884	0.8812	0.7010	0.9593	0.6917	0.8844	0.7044	0.9674
U-Net + Proposed (0.5 – 0.5)	0.7356	0.8233	0.7422	0.9442	0.7461	0.8161	0.7514	0.9536
WT-Net [11]	0.8205	0.8569	0.8234	0.9748	0.8226	0.8559	0.8253	0.9753
WT-Net + Proposed (0.5 – 0.5)	0.8370	0.8115	0.8348	0.9783	0.7894	0.8626	0.7950	0.9743
WT-Net + Proposed (0.25 – 0.75)	0.8735	0.6443	0.8486	0.9851	0.8656	0.6195	0.8381	0.9890

Conclusion

In this paper, a novel, saliency-based algorithm has been introduced for tumor segmentation in brain MRI image volumes. The proposed method is based on a state-of-the-art approach; however novel features have been introduced for higher segmentation performance. A new pseudo-color model has been proposed, by building a healthy mean image template for *FLAIR* and *T2* scans to highlight tumors as salient image regions. To detect salient regions, the connectivity of neighboring slices was incorporated into the final saliency map besides color and spatial features. To detect the outline of the localized tumor, region-based active contour was applied.

The proposed model was also combined with two different, state-of-the-art convolutional neural networks (U-Net and WTNet), by introducing a weighting function for the saliency map and the networks prediction maps. The combined map integrates the networks' abstraction and the handcrafted features' ability to also handle special, unseen cases more efficiently. Quantitative tests on the BRATS2015 dataset confirmed that the proposed model is quite efficient by itself, however by combining it with neural networks, the segmentation accuracy can further be increased.

In the future, we plan to create a more sophisticated fusion model of training-based methods and handcrafted features, by designing a deep convolutional network that incorporates the saliency features into the training process itself.

Acknowledgment

This work was partially funded by the Hungarian National Research, Development and Innovation Fund (NKFIA) grant nr. KH-126688 and the Hungarian Government, Ministry for National Economy (NGM), grant nr. GINOP-2.2.1-15-201700083.

REFERENCES

[1] Eric C Holland, "Progenitor cells and glioma formation," *Current opinion in neurology*, vol. 14, no. 6, pp. 683–688, 2001.

[2] Bjoern H Menze, Andras Jakab, Stefan Bauer, Jayashree KalpathyCramer, Keyvan Farahani, Justin Kirby, Yuliya Burren, Nicole Porz, Johannes Slotboom, Roland Wiest, et al., "The multimodal brain tumor image segmentation benchmark (BRATS)," *IEEE Transactions on medical imaging*, vol. 34, no. 10, pp. 1993–2024, 2015.

[3] Marcel Prastawa, Elizabeth Bullitt, Sean Ho, and Guido Gerig, "A brain tumor segmentation framework based on outlier detection," *Medical Image Analysis*, vol. 8, no. 3, pp. 275–283, 2004.

[4] Mikael Agn, Oula Puonti, Ian Law, PM af Rosenschöld and K van Leemput, "Brain tumor segmentation by a generative model with a prior on tumor shape", *Proceeding of the Multimodal Brain Tumor Image Segmentation Challenge*, pp. 1-4, 2015.

[5] Stefan Bauer, Lutz-P Nolte, and Mauricio Reyes, "Fully automatic segmentation of brain tumor images using support vector machine classification in combination with hierarchical conditional random field regularization," in *International Conference on Medical Image Computing and Computer-Assisted Intervention*, 2011, pp. 354–361.

[6] Wei Wu, Albert YC Chen, Liang Zhao, and Jason J Corso, "Brain tumor detection and segmentation in a CRF (conditional random fields) framework with pixel-pairwise affinity and superpixel-level features," *International Journal of Computer Assisted Radiology and Surgery*, vol. 9, no. 2, pp. 241–253, 2014.

[7] Olaf Ronneberger, Philipp Fischer, and Thomas Brox, "U-net: Convolutional networks for biomedical image segmentation," in *International Conference on Medical image computing and computer-assisted intervention*. Springer, 2015, pp. 234–241.

[8] Wang Guotai, Li Wenqi, Ourselin Sebastien, and Vercauteren Tom, "Automatic brain tumor segmentation using cascaded anisotropic convolutional neural networks," in *Brainlesion: Glioma, Multiple Sclerosis, Stroke and Traumatic Brain Injuries*. Springer, 2018, pp. 179–190.

[9] Subhashis Banerjee, Sushmita Mitra, B Uma Shankar, and Yoichi Hayashi, "A novel GBM saliency detection model using multi-channel MRI," *PloS one*, vol. 11, no. 1, pp. e0146388, 2016.

[10] Tony F. Chan and Luminita A. Vese, "Active contours without edges," *IEEE Trans. on Image Processing*, vol. 10, no. 2, pp. 266–277, 2001.

[11] Eli Gibson, Wenqi Li, Carole Sudre, Lucas Fidon, Dzhoshkun I. Shakir, Guotai Wang, Zach Eaton-Rosen, Robert Gray, Tom Doel, Yipeng Hu, Tom Whyntie, Parashkev Nachev, Marc Modat, Dean C. Barratt, Sbastien Ourselin, M. Jorge Cardoso, and Tom Vercauteren, "Niftynet: a deep-learning platform for medical imaging," *Computer Methods and Programs in Biomedicine*, vol. 158, pp. 113 – 122, 2018.

Volume Visualization - Challenges and Tasks (ABSTRACT ONLY)

Balázs Tukora*

* University of Pécs, Faculty of Engineering and Information Technology, Dept. of Information Technology, Pécs, Hungary

Keywords: Direct volume rendering, ray casting, 3D texture mapping.

Abstract: During the development of medical visualization solutions several challenges arise. Recently such new platforms, like the mobile and standalone VR headsets, have become targeted with special characteristics and requirements. The traditional volume visualization techniques that show good performance in desktop environment are prone to underachieve on these devices. On the other hand, the users have become accustomed to the highest graphic quality, and don't want to lose this experience. New ways have to be found to provide high graphics quality with interactive frame rates on a wide range of platforms with different capacity.

Fully automatic 3D liver segmentation with U-Net Convolutional Neural Network

Bence Németh, Istvan Ervin Haber

Zinemath Zrt., zMed project, Pécs, Hungary
University of Pecs, Faculty of Engineering and IT

Index Terms:
fully automatic liver segmentation, convolutional neural network, U-Net, 3D medical image processing, deep learning

Abstract:
One way of understanding any human organ is to process medical images into 3D volumes. It can be used to visualize the structure of healthy anatomical organs and use the models for further processing in surgical planning or in education. They give the opportunity to measure, modify, annotate the medical image based 3d models and use also in complex treatment methods. Among other processes like traditional image processing in algorithmic way, Neural Networks can be trained to recognize organ shapes in case they can be feed with an adequate number of training data. The solution presented in this paper is a fully automatic liver segmentation approach to segment the liver from various CT scans. It utilizes convolutional neural network with U-Net architecture. The proposed method is trained on an annotated dataset of 220 CT volumes with various different scanning protocols. This approach reached the best performance so far among our all developed segmentation algorithms not only in terms of accuracy but also in speed. The trained model can be applied to create initial 3D liver segmentation to facilitate the radiotherapy planning workflow.

Introduction

Automatic liver segmentation in 3D medical images is essential in many clinical applications, such as pathological diagnosis of hepatic diseases, surgical planning, radiation therapy planning and postoperative assessment. However, it is still a very challenging task due to the fuzzy boundary, complex background and various appearance of the liver. Several methods have been proposed for automatic liver segmentation based on convolutional neural networks. Dou, et al. proposed a fully convolutional (FCN) solution where the output is refined with a conditional random field approach (CRF) [1]. Similarly, Christ et al. used FCN with CRF in cascaded U-Net architectures [2]. Graph-cut based refinement was applied in the approach proposed by Lu, et, al. [3]. Dong, et, al. approached the problem with Generative Adversarial Network (GAN). While GAN generator attempts to produce output that is close to the real samples, discriminator tries to distinguish between generated and real images. They proposed a deep image-to-image network (DI2IN) as a generator producing the liver segmentations [4].

Methods

The network used in this project is built in a U-Net architecture proposed by Ronneberger et al [5]. As preprocessing, windowing, histogram equalization and isovolumetric resampling were carried out. Values were windowed in the range [-200, 500] to keep only those voxels that intensities are near to liver's. After windowing, histogram equalization helps to increase the contrast of the soft tissue in the windowed range. Isovolumetric resampling change every voxel in the dataset to 1x1x1 mm.

Our dataset consists of CT scans from the publicly accessible LITS (Liver Tumor Segmentation Challenge) and also a dataset received from the University of Pecs PACS database, with manual segmentation made by the Radiology Clinic (about 60 pieces), in frame of a cooperation project. Rotation and shifting transformations were applied during training phase as data augmentation. An important step, class balancing was performed according to the pixel-wise frequency of the liver and background class. Due to the relative small number of liver voxel, imbalanced classes could cause a accuracy paradox or inappropriate training. To address this problem, a weighting factor was introduced in the cross entropy loss function.

The model was trained with transfer learning using pretrained neural network model. The trained network can be used as initialization of the model to train on liver segmentation task instead of using initial random

weights. We used pretrained U-Net models provided by Ronnenberger et al. [5] that was trained on cell image segmentation task.

Results

The results can be correctly shown on exported pictures (Fig. 1. & 2.) and validate by radiology or anatomy specialist medical doctors. In this case a manual segmentation was available, and a qualitative algorithmic comparison process performed.

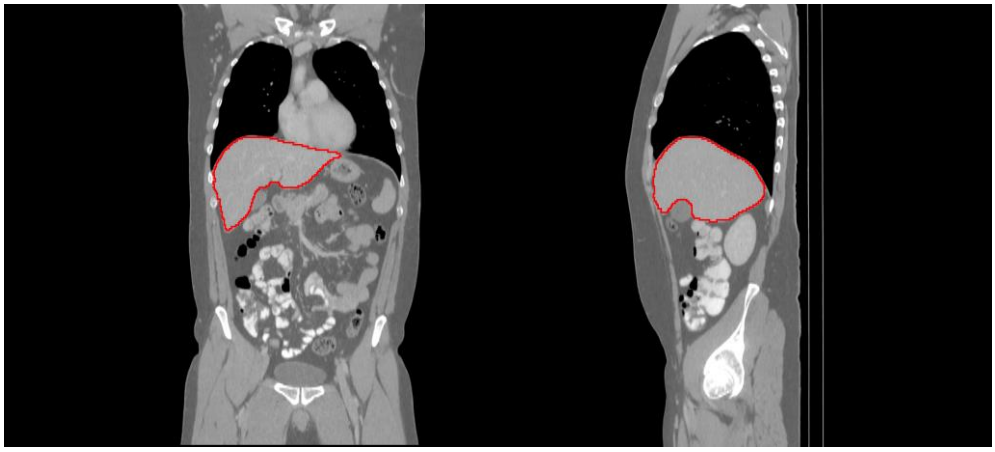

Fig. 1. Coronal (left) and sagittal (right) view of the border of the automatic segmentation's result

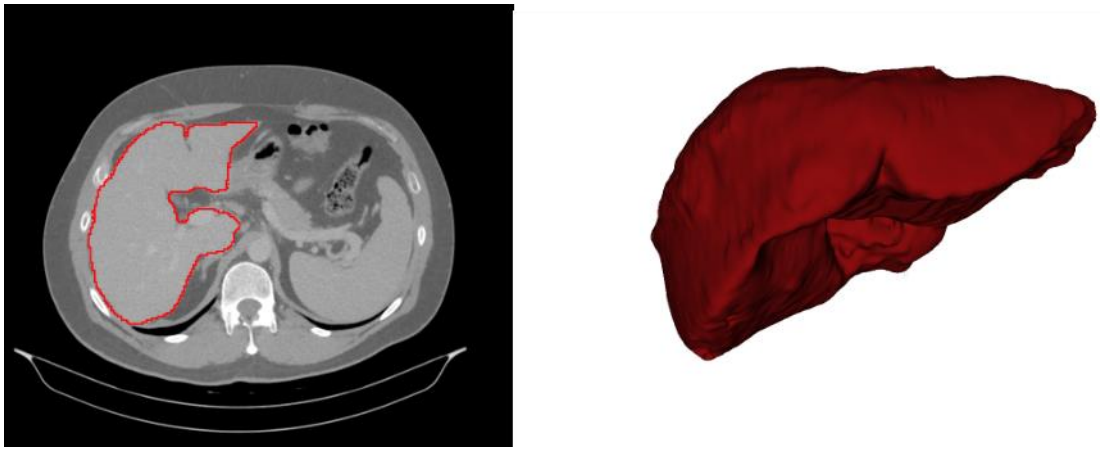

Fig. 2. Horizontal view (left) of the border of the automatic segmentation and the generated mesh of the segmented mask

The quality of a segmentation can be evaluated in many different ways, but it depends on the segmentation tasks. There are different common evaluation metrics and most papers on segmentation report results in terms of more of them. An overview and the detailed description of metrics are given in [4]. One of the mostly used metrics is the DICE coefficient. The evaluation samples are 18 manually segmented CT volumes with various size, slice thickness and resolution. We have evaluated different metrics shown in the table below.

Table 1. Results of trained model tested on 20 different abdominal CT volume

Metric	Average	STD
Dice Coefficient	0,898	0,078
Jaccard Coefficient	0,822	0,118
Area under ROC Curve	0,984	0,016
Cohen Kappa	0,895	0,080
Rand Index	0,988	0,012
Adjusted Rand Index	0,890	0,085
Interclass Correlation	0,898	0,078
Volumetric Similarity Coefficient	0,921	0,080
Mutual Information	0,136	0,026
Coefficitent of Variation	0,973	0,033
Specificity	0,994	0,006
Precision	0,843	0,122
F-Measue	0,898	0,078
Accuracy	0,994	0,006
Fallout (false positive rate)	0,006	0,006

Results show that the trained model with U-Net architecture achieves good segmentation quality as well as fast processing speed and robustness. More training, more data in the training database or bigger network may improve further the performance.

Conclusions

We have shown that utilizing the U-net architecture can be an accurate and fast solution to automatically segment liver from CT scan. That can be used to doctors to create liver masks faster as surgical or radiation therapy planning.

This project was funded in frame of the GINOP-2.2.1-15-2017-00083 project.

REFERENCES

[1] Dou, Qi, et al. "3D deeply supervised network for automatic liver segmentation from CT volumes." International Conference on Medical Image Computing and Computer-Assisted Intervention. Springer, Cham, 2016.

[2] Christ, Patrick Ferdinand, et al. "Automatic liver and lesion segmentation in CT using cascaded fully convolutional neural networks and 3D conditional random fields." International Conference on Medical Image Computing and Computer-Assisted Intervention. Springer, Cham, 2016.

[3] Lu, Fang, et al. "Automatic 3D liver location and segmentation via convolutional neural network and graph cut." International journal of computer assisted radiology and surgery 12.2 (2017): 171-182.

[4] Yang, Dong, et al. "Automatic liver segmentation using an adversarial image-to-image network." International Conference on Medical Image Computing and Computer-Assisted Intervention. Springer, Cham, 2017.

[5] Ronneberger, Olaf, Philipp Fischer, and Thomas Brox. "U-net: Convolutional networks for biomedical image segmentation." *International Conference on Medical image computing and computer-assisted intervention*. Springer, Cham, 2015.

[6] Taha, Abdel Aziz, and Allan Hanbury. "Metrics for evaluating 3D medical image segmentation: analysis, selection, and tool." BMC medical imaging 15.1 (2015): 29.

Proceedings and Abstracts of the 2nd Day (October 6th Saturday)

The Use of 3D Technologies and Tools in Humanities (ABSTRACT ONLY)

Máté Deák *

* University of Pécs, Faculty of Humanities, Institute of Public Relations, Department of Political Science and International Studies, Pécs, Hungary

Keywords: digital humanities, 3D, archeology, LiDAR, Pazirik, MozaWeb, VR technologies, Oculus Rift, museology

Abstract: 3D technologies and their use are more and more known in science and the fields of their presence are growing. However these technologies and the popular imagination of their use are strongly connected to engineering and life sciences – it is a propably lesser known fact that digitization and 3D is used in history, archeology, arts and several other fields of humanities also as a part of the transformation and modernization of the mentioned sciences.

The presentation will highlight the most important methodologies (best practice) and projects from all around the World of 3D technologies in humanities such as a new approach of teaching – „educate while playing" (Pazirik Ltd., MozaWeb) or lead projects as „LiDAR" (archeological discoveries in Central America). These new tools are able to recreate ancient forts, cities even battles – and the viewer can be one of the citizens lived in the city or a soldier who fought in the battle with realistic arms! The presentation also focuses on newly utilized virtual viewers (VR technologies, Oculus Rift) and their role in exhibitions, libraries and museums as a tool of scientific entertainment. Experimental archeology and digital maps are the best examples where 3D technologies (such as 3D printing) can develop research methodology to a new level.

These brand new tools and practices are the future of researching, demonstrating and teaching humanities. However these technologies are not affordable for all institutions and research groups in Hungary. The lack of transdisciplinary and interdisciplinary researches – please note that there are great projects exist already and their number are increasing – still means a problem. The field of humanities still need skilled researchers able to work with these tools and methodologies and also able to cooperate with experts from other scientific fields such as engineers and 3D experts.

With these developing and new universe education and research received a fascinating tool, and it slowly appears in the every day practice of the field of humanities. The importance of this can be easily shown: amongst others there are conferences all around the World as the one held in Warsaw at the Cardinal Stefan Wyszyński University with the title of „3D Technologies for Archeology and Museology".

The Moiré Method and its Application in Scoliosis

Csaba Bogdán
University of Pécs – Faculty of Engineering and Information Technology
Department of Mechanical Engineering
Pécs, Hungary

Keywords: moiré method, shadow moiré, projection moiré, digital moiré, KAMAL-method, scoliosis

Abstract:

The diagnostic study of spinal deformities has long been a focus of medical science. For a clear condition assessment of scoliotic patients X-ray images are used. Disadvantages of X-ray inspections, however, make methodological research, which can lead to fast and cost-efficient examinations without harmful radiation, reasonable.

HISTORY: In 1874, after LORD RAYLEIGH had studied the resultant pattern, the so-called moiré fringes of two overlapping grids, he concluded that the phenomenon could be useful for measurement purposes. Beyond industrial applications further research, about a hundred years later, proposed moiré topography for measurement of the human body.

AIMS AND METHODS: The aim of this publication, based on thorough study of resources, is to present the basic theory of the moiré method and its application in scoliosis. The two main methods − the shadow and projection moiré − of moiré technique are described in detail. Moreover, the paper presents KAMAL's algorithm suggesting to calculate the plane angle of curvature in single-curve scoliosis cases and proposes directions for further research and developments.

RESULTS: The significant advantages of the moiré method are that it is fast, non-invasive, portable, cost-efficient and has no harmful radiation. A moiré technique chosen and algorithmized well can be convenient for substitution or as a complement of X-ray images in scoliosis. However, it is a limitation that a methodological standard which could lead to generally reliable results has not been created yet. Furthermore, the amount of labour required for the evaluation of moiré images is not inconsiderable. To achieve further success of the moiré method a dedicated partnership of engineers and physicians, respectively the application of technical-biomedical knowledge is needed.

Introduction

In 1874, after LORD RAYLEIGH had studied the resultant pattern, the so-called moiré fringes of two overlapping grids, he concluded that the phenomenon could be useful for measurement purposes [1]. Beyond industrial applications further research, about a hundred years later, proposed moiré topography for measurement of the human body [2].

The phenomenon of moiré is already known by mankind from deep antiquity. In ancient China, moiré was used to visualize dynamic patterns on silk fabrics. The word moiré [mwaʁe] can be traced back to the Arabic mukhayyar *'cloth made from the wool of the Angora goat'* < lit. '*select, choose'* which the English mohair derives from [3, 4]. The word 'mohair' was pronounced *moiré* by French silk weavers in the 17th century but instead of the name of the fabric it was understood as the wavy stripes (moiré phenomenon) produced by glossy fabric fibres [3, 4, 5]. Therefore, moiré refers to an irregular wavy surface the pattern of which changes in accordance with its movement [4, 6].

The moiré phenomenon becomes visible, for instance, if two (or more) structures with similar geometry overlap. In these cases, a resultant pattern of light and dark fringes can be seen (Fig. 1). In general, the dark fringes are called moiré stripes [7, 8]. Classic everyday examples of moiré are the wavy folds of lace curtains and pictures of people wearing striped patterned clothes. In the first case the small net structures are the ones that overlap, while in the second case stripes and camera sensors or screen pixels interfere with each other.

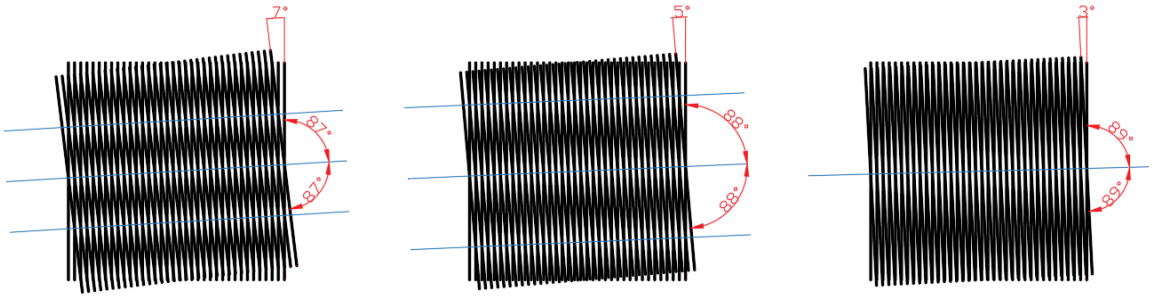

Fig. 1. Moiré fringes of identical grids with different angle deviations

Shadow and projection moiré techniques

Moiré techniques, based on the physical phenomenon of moiré, are procedures usually used for surface and shape mapping or deformation measurement purposes [7, 9]. The main concept of the moiré measurement is to associate a basic structure with the state of the examined body and another structure with its (deformed) state to be measured. From the moiré pattern created by these interacting structures we can conclude the differences between the two states of the body.

Moiré techniques differ in regards to the different ways the moiré patterns are created and processed [7]. There are several moiré techniques, but here only the two main geometrical approaches, namely the shadow and projection moiré methods are going to be discussed. In the shadow moiré technique, the moiré phenomenon is created by the overlapping of a single reference grating and its shadow projected on the surface (Fig. 2).

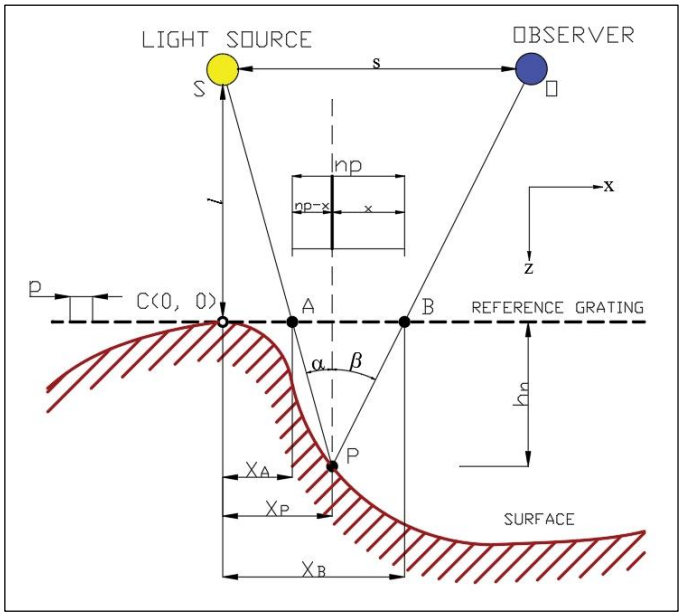

Fig. 2. Optical arrangement of the shadow moiré technique

The reference grating positioned in front of the examined surface area is illuminated with a perpendicular point light source (*S*). Therefore, a shadow grating is produced that becomes distorted in correspondence with the surface characteristic. For the observer (*O*) that is *s* distance from, and parallel to, the light source, the moiré phenomenon which is the result of the grid and its own shadow on the surface, becomes visible. The projection moiré technique, especially in regards to examinations of posture defects, appears in scientific papers more frequently from the 2000s. This is explained by the development of image processing which makes moiré topography on delicate and complex surface areas of the human body successful [7]. In the projection moiré technique two identical grids are used: one for projection and another for reference (Fig. 3). By the optical system, the projection grid is projected to the examined surface, creating a linear base grid. Then the detector takes a picture through the reference grating of the object's surface and the base grid on it. To the observer the

moiré phenomenon becomes visible as the resultant pattern of the reference grid and the distorted base grid on the object's surface.

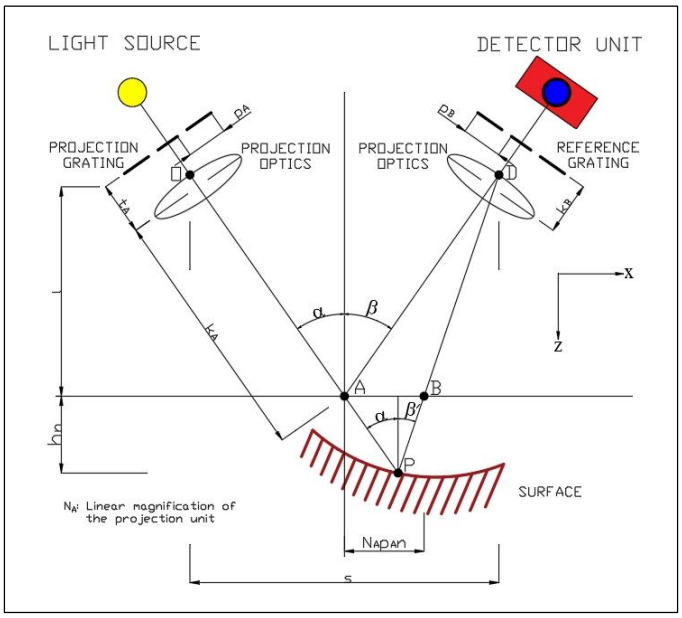

Fig. 3. Optical arrangement of projection moiré technique

The main advantages of the moiré technique are that it is fast, non-invasive, portable, relative cheap and has no harmful radiation. The relatively fast data collection and processing makes real time examinations and automated processes possible [10]. There are, however, some disadvantages to the technique. ANTAL highlights [11] that although the resolution of the moiré pictures can be changed, it has its own technological limitations in that changes in the resolution could be to the detriment of other relevant measurement factors. An accurate surface analysis demands serious considerations regarding approach and algorithm and data analytical post-processing. The proper projection of a high contrast on images can also serve as a challenge. The geometrical arrangement of the moiré equipment has a strong effect on the moiré pattern. Therefore, to handle the resultant deviation it is necessary to have a thorough analysis in measurement technological adaptability and error correction. The analysis of slanting surfaces can also be problematic [11].

Moiré method in scoliosis

The different types of spinal deformities have been in the focus of medical attention for thousands of years. We can find references and medical advice to the treatment of scoliosis in ancient Hindu religious texts (3500-3000 B.C.) and Egyptian injury care guides (2600-2200 B.C.) [12]. The Hippocratic Corpus (lat. Corpus Hippocraticum) mentions the lateral curvature of the spine, and terms like scoliosis, kyphosis, lordosis created by GALEN (129-216?) show the all-time validity of our topic. Referring to the importance of the treatment in scoliosis, the French physician NICOLAS ANDRY (1658-1742) on a title page of his famous work *Orthopaedia: or the art of correcting and preventing deformities in children* proposed a picture of a crooked tree tied to a stake [13] as the symbol of the orthopaedic profession.

The traditional diagnostic of scoliosis is performed by orthopaedists in a painless examination called forward bending test [14]. This method, however, beyond the fact that it may produce too subjective results, is not reproductive and time consuming [14]. It is also common that physicians perform examinations manually based on radiographs but these evaluations are also time-consuming and in case of a larger group (e.g. in school screenings) they may be inaccurate [15]. Depending on the medical practice of a given region, for an accurate diagnosis it is important to provide X-ray images with front and back views of the spine in standing and in forward bending position and with a lateral view [15, 16].

In the diagnostics of scoliosis, the so-called Cobb angle measured on radiographs (Fig. 4) is considered the golden standard [17].

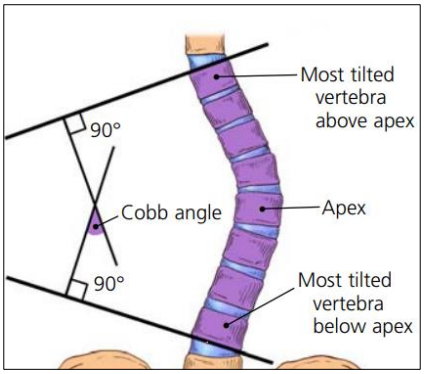

Fig. 1. Measurement of Cobb angle [18]

To the Cobb angle, the angle value of spinal curvature measured on moiré images can be approximated. For the evaluation of moiré pictures different measurement approaches can be used. A digital (projection) moiré technique (Fig. 5) presented by ANTAL et al. [16], for instance, used KAMAL's method for evaluating moiré images of scoliotic patients aged 9-17 years.

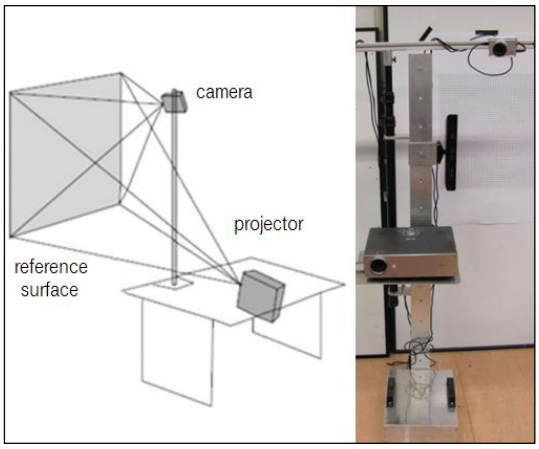

Fig. 5. Digital moiré equipment: scheme and realization (transl. by auth) [16]

For measuring the two-dimensional curve angle of a single-curve scoliotic spine, KAMAL's approach [19, 20] considers points describing the most asymmetries on the back (Fig. 6). In the moiré image of a healthy back the number of moiré stripes on the two sides of the spine within the same distance are equal. The scoliotic spine does not have this symmetry [20].

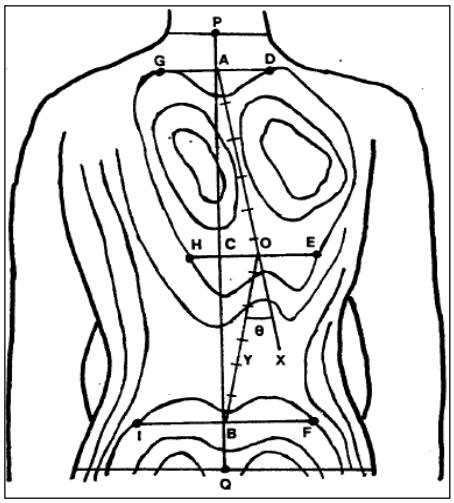

$$Y_1 = \tan^{-1}\left(\frac{|d_1 - d_2|}{AC}\right) \qquad Y_2 = \tan^{-1}\left(\frac{|d_1 - d_3|}{BC}\right)$$

$$d_1 = \frac{1}{2}(CH + CE)$$

$$d_2 = \frac{1}{2}(AD + AG)$$

$$d_3 = \frac{1}{2}(BF + BI)$$

$$\theta = \tan^{-1}\left(\frac{|d_1 - d_2|}{AC}\right) + \tan^{-1}\left(\frac{|d_1 - d_3|}{BC}\right)$$

Fig. 6. Measuring points and mathematical relationships of KAMAL's method [19]

ANTAL et al.'s results of the evaluated moiré images (e.g. Fig. 7) of the trial group showed that the Cobb angle was well approximated in case of patients with thoracic curvature. Differences from the Cobb values, however, in upper thoracic curvatures and lumbar curvatures were significant (10°-15°). The reason for this is down to the general characteristic of the scapula and the trunk's thick bundles of muscle covering the spine [16].

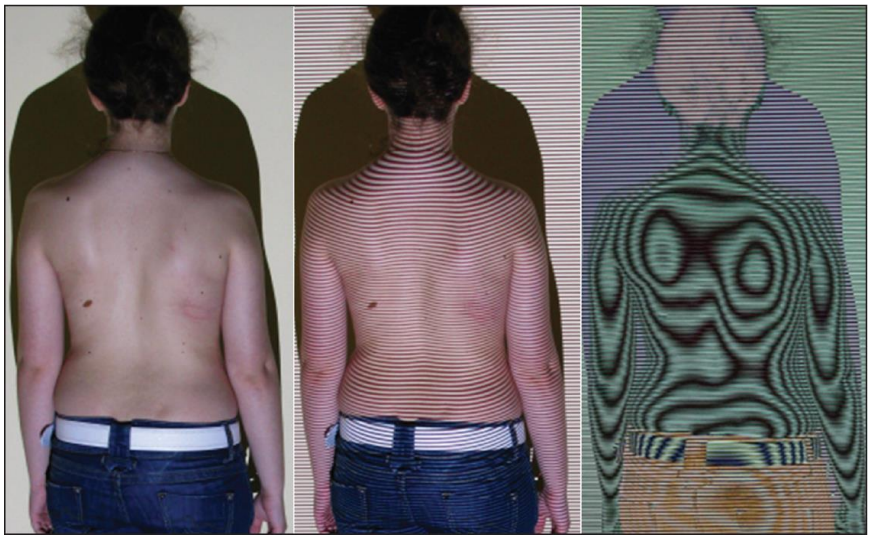

Fig. 7. Phases of producing digital moiré images [16]
From the left: normal image of the back; distorted image of the linear grating; software generated moiré image

Fig. 8. Moiré and X-ray images of the same person [14]

Proposed directions for further research and development

Regarding development of the moiré technique in scoliosis we can find more directions in scientific works (e.g. detect deformities in the elderly, using an automatic algorithm for scoliosis detection) [7, 11, 22]. Based on insights partially getting from different papers I consider the following 4 points vital to a well worked moiré technique and equipment in scoliosis.

1. Starting a dialogue for creating a methodological standard in diagnostics of scoliosis:

For a more precise interpretation of surface topographical methods, it is important to create a standard body posture during examinations [17]. Although we know a few body posture protocols [7, 16, 23] applied during moiré examinations, we cannot speak about a concrete methodology that could lead to generally reliable results. A methodological standard could help the better interpretation of moiré images of scoliotic patients with distorted trunk where the results can be false [7, 16, 17]. In other respects, as well, we can find hints to the lack of standardization when three surface topographical methods (moiré technique, Scoliometer® and BCD 'back-contour device') are compared. PEARSALL et al. [24] concluded that these three techniques cannot be used interchangeably in clinical recording if the posture is not standardized. Therefore, the standardized posture is a problem that needs to be resolved [7, 25].

2. Refine the algorithm for measuring scoliotic spine curvature:
It can be done by rethinking or enhancing the mathematical-geometrical approach of KAMAL in order to get more accurate spinal curvature angle values, especially in cases of upper thoracic and lumbar curvatures. For a generally reliable algorithm a standardised posture during diagnostics is also imperative.

3. Detailed introduction of a well worked moiré equipment with how-to steps:
The purpose is to bring the medical and engineer knowledge closer and encourage moiré research in medical (orthopaedic) circles. Several orthopaedists could have a positive approach towards the moiré technique and, therefore, it is important to provide more practical information.

4. Improving communication between technical-biomedical experts and physicians:
For the successful development and application of the moiré technique, it is vital to have clear and unambiguous communication processes within interdisciplinary research groups. To achieve this goal a dedicated partnership of engineers and physicians, respectively the application of technical-biomedical knowledge is necessary. There have been cases where the careless use of the moiré technique resulted in false calibrations and interpretations [26]. Beyond, but in parallel to the technical-biomedical and medical knowledge, the continuous and conscious presence of the human factor plays a key role which has a particularly great influence on communication processes among interdisciplinary research groups.

Conclusion

The significant advantages of the moiré method are that it is fast, non-invasive, portable, cost-efficient and has no harmful radiation. A moiré technique chosen and algorithmized well can be convenient to substitute or complement X-ray images in scoliosis. However, its limitation is that a methodological standard which could lead to generally reliable results has not been created yet. Therefore, although the moiré topography provides information about the shape of the surface examined, it is a major drawback that the conclusion drawn will not be without ambiguity. Furthermore, the amount of labour required for the evaluation of moiré images is not inconsiderable [7, 11]. To achieve further success of the moiré method a dedicated partnership of engineers and physicians, respectively the application of a joint technical-biomedical knowledge is needed.

REFERENCES

[1] LORD RAYLEIGH *On the manufacture and theory of diffraction gratings*, Philosophical Magazine 47 (1874), 81-93; 193-205.

[2] TAKASAKI, H. *Moiré topography*. Applied Optics 1970;9(6):1467–72.

[3] Merriam-Webster, Inc. Webster's ninth new collegiate dictionary, Springfield, Mass.: Merriam-Webster, 1987, 763. (vid. mohair and moiré)

[4] CONWAY, A. *Moiré fringes on the factory floor*, New Scientist, 1972.06.22., 54:801, 692.

[5] HOAD, T.F. *Oxford Concise Dictionary of English Etymology*, Shanghai Foreign Language Press, 2000, 298.

[6] AMIDROR, I. *The Theory of the Moiré Phenomenon Volume I: Periodic Layers*, Second Edition, Springer, 2009, 1.

[7] PORTO, F.; GURGEL, J. L.; RUSSOMANO, T.; FARINATTI, P. T.V. *Moiré Topography: From Takasaki Till Present Day* In: Theodoros B. Grivas (ed): Recent advances in scoliosis, Intech, 2012, 103-118.

[8] RÖSSLER, T.; HRABOVSKÝ, M.; POCHMON, M.; (2006). *Moiré methods for measurement for displacement and topography*, Czech J Phys, 2006, Vol 56(2), 101-216.

[9] LINO, A.C.L.; FABBRO, I.M.D.; (2004). *Fruit profilometry based on shadow Moiré techniques*, Ciênc Agrotec, 2004, Vol 28(1), 119-125.

[10] PATORSKI K. AND KUJAWINSKA M. *Handbook of the Moire Fringe Technique*, Elsevier, Amsterdam, 1993.

[11] ANTAL, Á. *Optikai úton generált Moiréfelületek hibaanalízise és identifikálása méréstechnikai alkalmazásokkal*, Doktori (PhD) disszertáció, 2009, 25-26

[12] MOLNÁR, S.; SKAPINYECZ, J.; CSERNÁTONY, Z. *A gerincdeformitás kezelése Nicolas Andry előtt*, Biomechanica Hungarica 2011; IV(1): 61-66.

[13] ILLÉS, T.; LAKATOS, J.; VARGA, P. P. *A gerinc betegségei* In: Szendrői Miklós (szerk.) Ortopédia, második kiadás, Semmelweis, 2009, 213-271.

[14] KIM, H.; TAN, J.K.; ISHIKAWA, S.; SHINOMIYA, T. *Automatic detection of spinal deformity based on statistical features from the moire topographic images*, International Journal of Computing, 2009, Vol. 8(1), 72-78.

[15] JANUMALA, T.; RAMESH, K. B. *A review of different analysing methods to detect spinal deformity*, International Journal of Advanced Research in Computer and Communication Engineering, Vol. 4(8), 2015/08, 352-355.

[16] ANTAL, Á.; BALLA, P.; PROMMER, K. *Digitális moiré képek vizsgálata gerincferdüléses betegek nyomon követésére*, Biomechanica Hungarica VII: (1), 50-60.

[17] PATIAS, P.; GRIVAS T.B.; KASPIRIS, A.; AGGOURIS, C.; DRAKOUTOS, E. *A review of the trunk surface metrics used as Scoliosis and other deformities evaluation indices*, Scoliosis, 2010, 5:12.

[18] GREINER, K. (2002). *Adolescent idiopathic scoliosis: Radiologic decision-making*, American family physician, 2002, 65, 1817-22.

[19] KAMAL, S. (1982). *Measurement of Angle of Spinal Curvature by Moiré Topographs*, Journal of Islamic Medical Association (USA). 14., 145-149.

[20] KAMAL, S. *Determination of degree of correction of spinal deformity by moiré topographs*, *Moiré fringe topography and spinal deformity*. In: Drerup, B.; Frobin, W.; Hierholzer, E. (eds) *Proceedings of the 2nd. International Symposium. Sep. 12-15*, 1982 Münster, West Germany, Stuttgart: Gustav Fischer Verlag; 1983, 117–26.

[21] EL-SAYYAD, M. *Comparison of Roentgenography and Moiré Topography for Quantifying Spinal Curvature*, Physical Therapy, Vol. 66(7), 1986.07.01, 1078–1082.

[22] AMEZQUITA R., SARMIENTO W. J., ROMERO E.: *Development of an automatic algorithm for scoliosis detection using Moiré topography*. III Iberian Latin American and Caribbean congress of Medical Physics, ALFIM 2004. Rio de Janeiro, Brazil.

[23] ADAIR I.V., VAN WIJK, M.C., ARMSTRONG, G.W. *Moire topography in scoliosis screening*, Clin Orthop Relat Res, 1977.11-12; (129):165–71.

[24] PEARSALL, D. J.; REID, J.G.; HEDDEN, D. M. *Comparison of three noninvasive methods for measuring scoliosis*, Phys Ther, 1992, Vol 72(9), 648-657.

[25] IKEDA, T.; TERADA, H. *Development of the moiré method with special reference to its application to biostereometrics*, Opt. Laser Technol., 12, 1981, 302-306.

[26] TAKASAKI, H. Guest editorial: *Moiré Topography in Japan*, Optics and Lasers in Engineering, Volume 3(1), 1982, 1.

Designing Measuring Instrument for Validation of City Simulations

Gergely Bencsik[*], István Ervin Háber, PhD[**]
[*] Szent István University, Gödöllő, Hungary
[**] University of Pécs, Pécs, Hungary

Keywords: Artificial Intelligence, Machine Learning, Validation, Modelling, Prediction, Renewable energy

Abstract: It is common to use machine learning and deep learning to make a real-time simulation of a system to predict it's parameters and to make prognosis about the interrelationship between the measured and predicted outcomes. In case of a city additional examination aspects come into scope like three dimensional simulation technologies e.g. Computational Fluid Dynamics (CFD). On the other hand it is necessary to decompose and evaluate data into multiscale aspects to get conclusions by variable space extent and time intervals of the observed dynamics of simulated physical or virtual subject matters. These fields complement each other. Validation of a city simulation is about making an adaptive methodology to fine the prediction models and the data preparation for all of the used simulations.

Introduction

A city simulation may include many different fields of aspect. For the first survey the relevant data set seemingly it holds independent information. It is impossible to discuss about a city's interactions as fully independent, non-overlapping dynamics behind. It's a premise that all the dynamics related to climate, traffic, infrastructural composition and even economics (etc.) of a technically well closured structure like a city has several over-lappings in their actual and future (short and long term) parameters. Making predictions for these fields independently may work but avoiding the discussed interactions between them makes it less accurate forecasting. After the whole simulation model's fields of interests been identified the next step is to validate the independent predictions and find a way to use the different data sets in other forecasting models. This paper describes an overall methodology of designing measuring instrument for validation of city simulations with climatic and energetic data in focus.

Validation

Validation of city simulations stands on two main pillars. Firs it should validate the initial data driven simulations' conclusions. Without initial data sets and some kind of virtual representation of the given city it's nearly impossible to make a real-time prediction system. All the test aspects have to get these points to be done. It gives a clear understanding how these fields overlaps when the relevant representations has been identified. We will discuss about the representation types in the next section. After the initial data driven simulations have made the given results in a short term, have to be compared to measured data in the future. After the comparison there will be a set of error values that can be used to set up regression models by getting an initial hypothesis function for each set. By long term comparisons it's going to be able to fine the hypothesis function but it's necessary to keep in mind that in a complex measurement system there will be corrupted or missed data by various interval of time. These cases are also need to be handled with data preparation. These cases can easily corrupt the hypothesis functions and makes inaccurate forecasting. Once a validated, adaptive model with a well fined validation is ready it has to guarantee a continuous accuracy for climate changing tendency of the years of operation.

On the other hand validation have to be used to understand the deeper interactions between the inspected fields like infrastructural head-emission and the efficiency of photo-voltaic (PV) energy production modules. Vehicle traffic and particle emission can also make effect on air mas (AM) that changes the efficiency of PV modules quantum efficiency by modulating the solar radiation spectral permeability of the air.

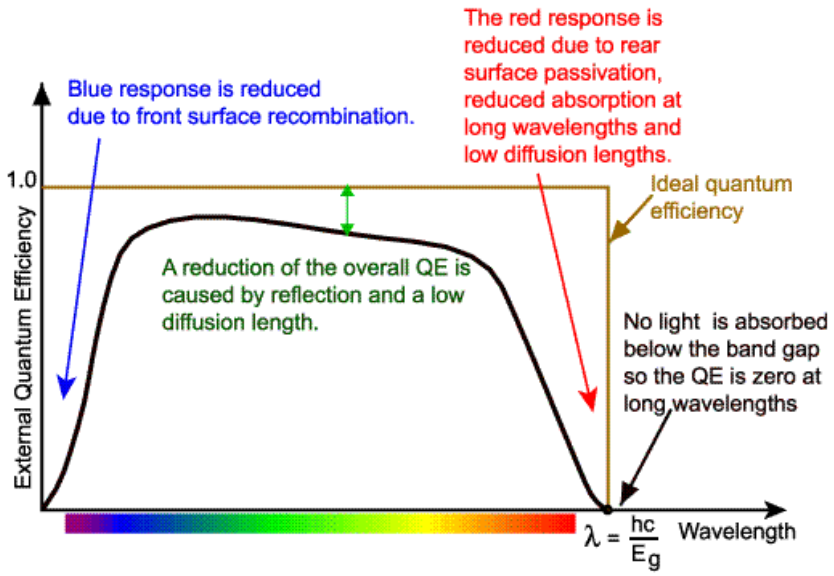

Fig. 1. Quantum efficiency curve of PV modules (source: http://pvcdrom.pveducation.org)

As it can be seen, a city simulation's complexity based on the various types of data that has to be used and the connections between them. There are another key-point to make an accurate forecasting and a well tuned validation. All the regression models have to get their data prepared and filtered their special way. There are many problems to solve with a technically closed structure's complex simulation. It stands on the fact that several aspects of the system's inspection interacts with each other in a very complex way. Both measured and predicted data are critical in their quality related to the prediction models. Some connections are not obvious because of their bias depends on other features of the area. Geographical scaling makes this ambiguity deeper. To handle these cases some method form deep learning (DL) can be used. Classifying interactions as various time interval based effects with a bias value can be useful in discover connections between measured data and features can make a prediction model more accurate. It also able to show if a data set makes a model instable in it's accuracy. In practice a classifier model has to make test cases and/or use a regression analysis like least absolute shrinkage and selection operator (LASSO) to select features to use or not to use in a prediction. The reason to make an independent model for classifying is that a city simulation got many different types of data to handle and many different regression models with their own preparation criterion. An independent classifier's job is to fine the regression models, to fine data preparations and to modulate data routing between regression models. (Fig. 3.)

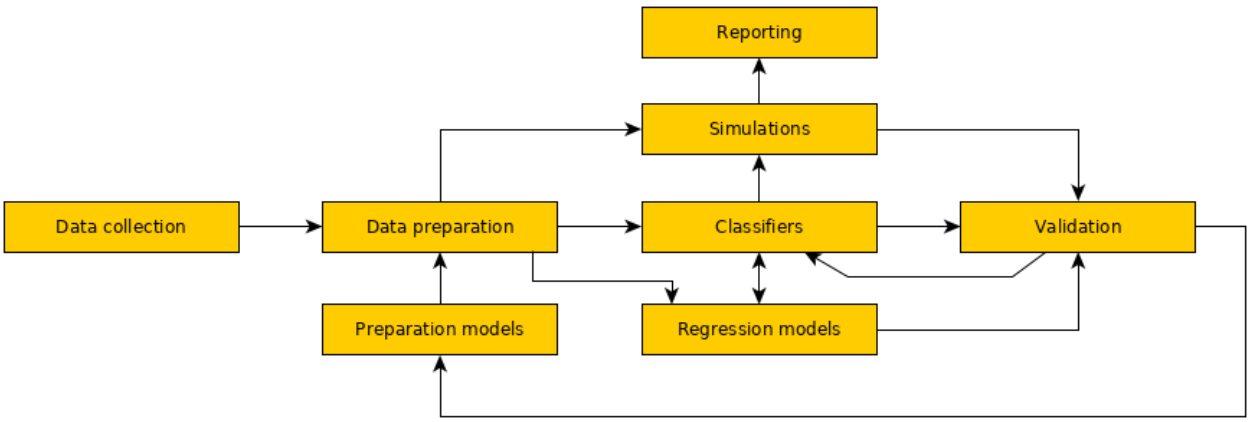

Fig. 2. Adaptive model for validating city simulations

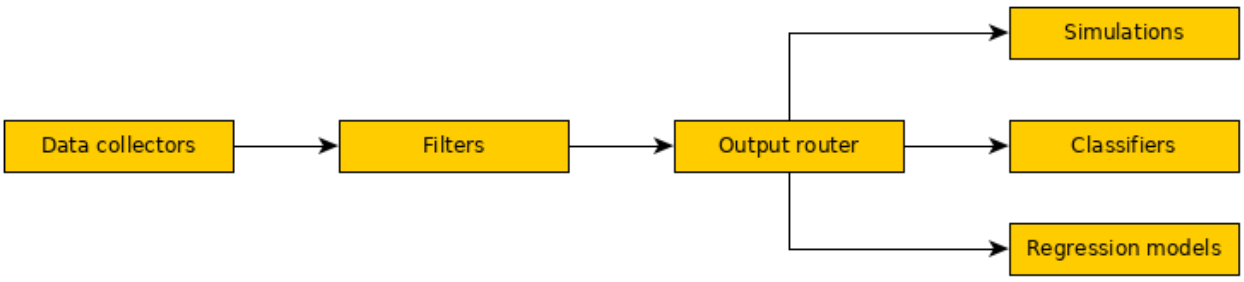

Fig. 3. Data flow

Representation of a city

There are two ways of representing a city for a simulation model. The virtual representation includes only the data sources and filtering nodes in a graph. In Fig. 4. we can see a simplified virtual representation of a city's electrical and climate model. It only represents the relevant data sets and the connection between them. These connections (the edges of the graph) should represent the data-flow and filtering processes. In case of a finalized virtual representation we can combine Markov Chain (MC), Hopfield Network (HN) and Boltzmann Machine (BM) types of neural networks according to the simulation prediction goals and data sources distribution of the model. All of the given nodes represents data sources and/or meta-data to predict.

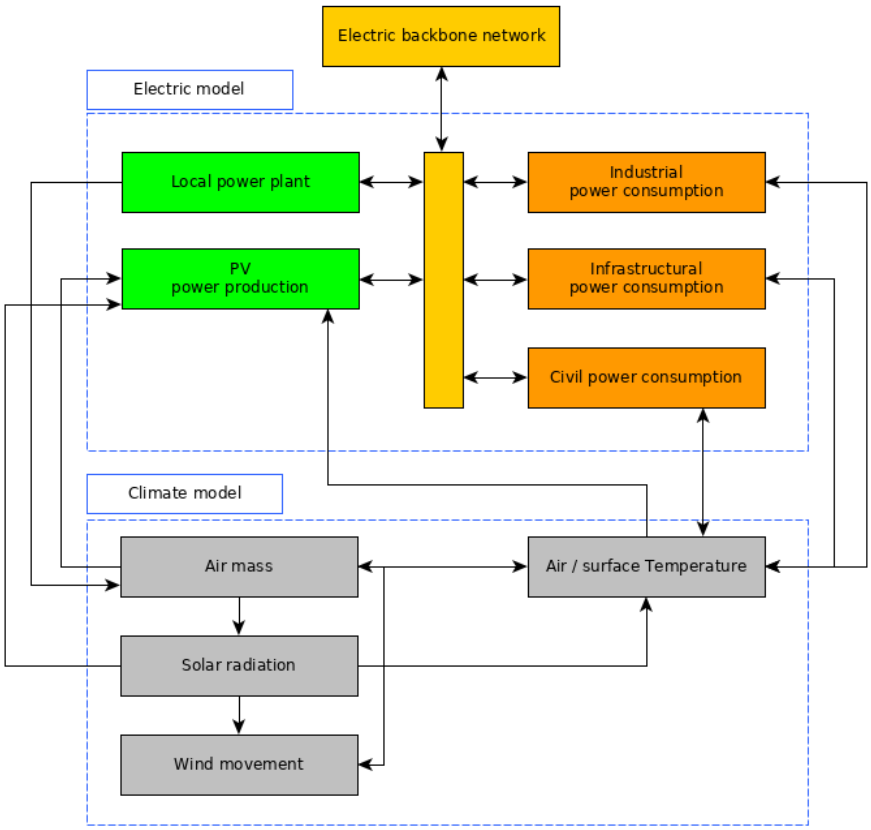

Fig. 4. Simplified virtual representation of a city's electrical and climate model

The other form representation is physical. It also enables to segment a city e.g. microclimate, urban climate and mesoclimate scales for a climate model. For an energetic model it also useful to segment power consumption and production scales from "global" to independent households, but it needs an energetic grid model. Combined physical representations like this, known as geographic information systems (GIS). In this case the energetic grid model itself a virtual model. Connecting a virtual model to a physical can also make the simulation more accurate. (i.e.: see the connection between power consumption nodes and air/surface

temperature node in Fig. 4. Power consumption of buildings has a known connection with their heat emission.) It is not possible to say that temperature measured in microclimatic scale differs from the mesoclimatic value only by the heat emission. In this case heat emission is a value that has to be predicted. It also a problem to identify the ratio of buildings', vehicles and neutral heat emission of the given area. With combining virtual models with physical it's possible to give an approximate ratio.

Physical representation

A physical model holds the opportunity to represent data in geographical space. A physical model can include modifiers like textures for albedo. With data for vehicle traffic it is also possible to aid a statistical data source for carbon and heat emission of city traffic.

2D maps and 3D models can be used as a physical representation. The second one is difficult to make, but adds many possibilities compared to a simple map, including CFD or a particle movement simulation (PMS).

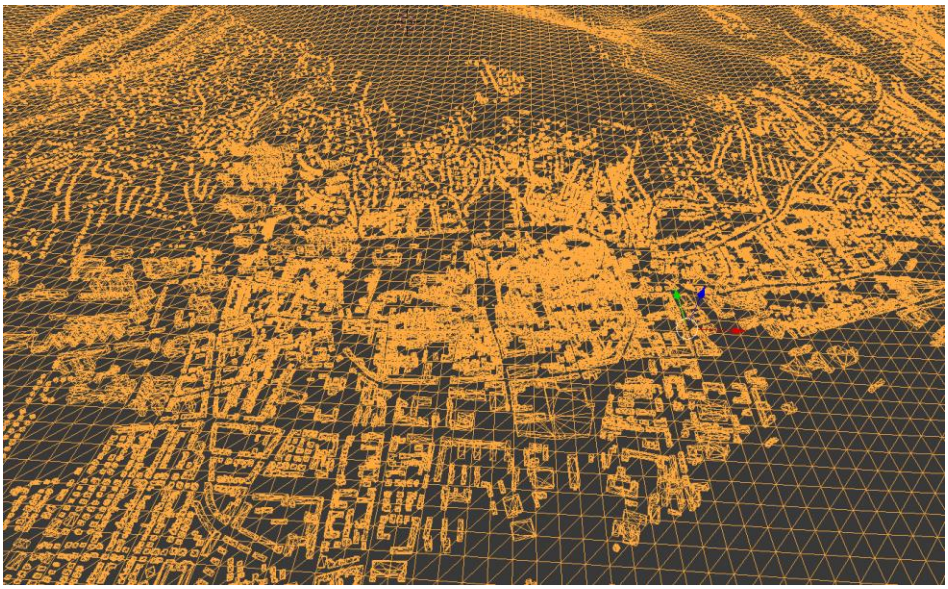

Fig. 5. Prepared 3D model of Pécs

It is important to prepare the 3D model according to the CFD or PMS simulation's preferences. Overlapping faces and holes on the mesh model makes it has to be avoided. 3D city models can be produced from geological data and building layout but there are other, more accurate methods to make a nearly usable model. Light Detection and Ranging (LIDAR) or stereoscopic scanning adds texture for the surfaces. With a textured model it's also possible to calculate an approximate albedo for the different regions.

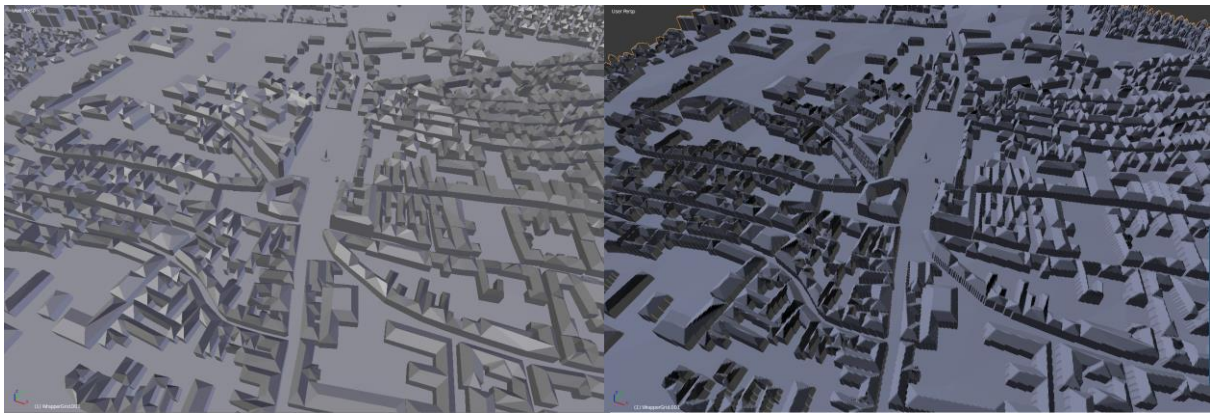

Fig. 6. Overlapping and incomplete 3D city model (left) and a prepared, CFD-ready version (right).

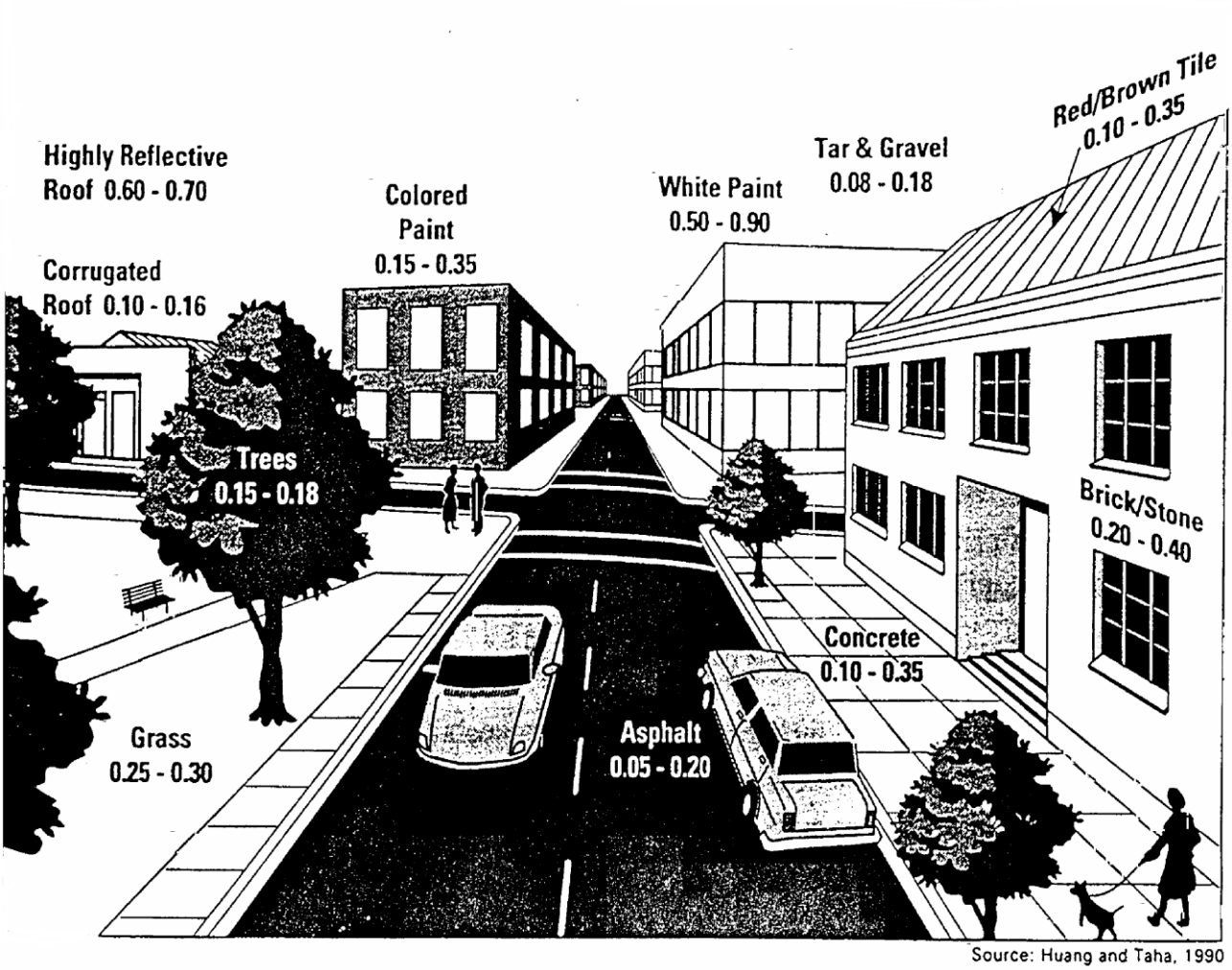

Fig. 7. Albedo values of different surfaces in urban environment. (source: Huang and Taha, 1990)

Conclusions

During the last decade, the vast improvement in machine and deep learning gave us new possibilities in simulations. The new principle of data science includes a large variety of methodologies to handle big amount of different types of data sets. It's more easier to set up an adaptive model for a complex simulation system by using these new technologies. With this adaptivity the system can be supplemented with new data sources over the operation without re-implementing the software backend.

By the validation of the real time simulation and regression models the data preparation and the prediction accuracy can be managed automatically giving a possibility to discover connections between measured and predicted data by a deep learning aided classifier.

REFERENCES

CAADRIA '98 : Proceedings of The Third Conference on Computer Aided Architectural Design Research in Asia. eds. T. Sasada, S. Yamaguchi, M. Morozumi, A. Kaga, and R. Homma April 22-24, 1998. Osaka University, Osaka, Japan. pp. 183-192.

István Háber, "Fotovillamos és fotovillamos - termikus rendszerek energetikai modellezése", 2016.

Anders, P.: (1997, Cybrids: Integrating Cognitive and Physical Space in Architecture, in: Jordan, J.P., Mehnert, B. and Harfmann, A. (eds), Representation and Design, Proc. ACADIA'97, The Association for Computer-Aided Design in Architecture, Cincinnati, pp. 17-34.

Aniceto Zaragoza Ramírez and César Bartolomé Muñoz (2012). Albedo Effect and Energy Efficiency of Cities, Sustainable Development - Energy, Engineering and Technologies - Manufacturing and Environment, Prof. Chaouki Ghenai (Ed.), ISBN: 978-953-51-0165-9, InTech, Available from:http://www.intechopen.com/books/sustainable-development-energy-engineering-and-technologies-manufacturing-and-environment/albedo-effect-and-energy-efficiency-of-buildings

Y.Toparlar, B.Blocken, B.Maiheu, G.J.F.van Heijst: A review on the CFD analysis of urban microclimate, Renewable and Sustainable Energy Reviews Volume 80, December 2017, pp. 1613-1640.

Sugawara, H. & Takamura, T. Boundary-Layer Meteorol (2014) 153: 539. https://doi.org/10.1007/s10546-014-9952-0

Abrar, Muhammad & Tze Hiang Sim, Alex & Shah, Dilawar & Khusro, Shah & , Abdusalam. (2014). Weather Prediction using Classification. Science International. 26. 2217-2223.

Automatic Shaping of Orthopedic Braces Using 3D Technology

Balázs Tukora*

* University of Pécs, Faculty of Engineering and Information Technology, Dept. of Information Technology, Pécs, Hungary

Keywords: 3D scanning, CAD, Blender, 3D printing, medical assistive devices.

Abstract: A research project that has been running since one and a half years in our institute, is addressed to examine the possibilities of the modern 3D technology, including 3D scanning, CAD modelling and 3D printing, in the creation of medical assistive devices, through the example of the manufacturing of orthopedic braces made for children to correct foot deformities.
We have developed a procedure that results in a pair of 3D printed leg braces, automatically shaped by 3D modelling scripts that use the 3D scanned model of the patients' feet. The introduced procedure is still a case study not to be directly applied in practice, but it is suitable to show the way of using widely available 3D technologies in the manufacturing of custom medical assistive devices.

Introduction

The aim of our project, initiated at the Faculty of Engineering and Information Technology at the University of Pécs, is examining how the newly available advanced but cheap technologies can be involved into the manufacturing process of the custom medical assistive devices. We try the processes of image and shape capturing, data processing and shape forming join in one single mobile device equipped with a 3D camera, low-power but fast computational units and hi-resolution display. We place confidence in the 3D printing technology hoping it becomes widely available at an acceptable price for the masses soon. Though the methods, such the multi-material printing we intend to apply during our project still require expensive devices, their impact on the medical assistive device industry is so strong that it would be a mistake excluding them from the examination.

For the objective of the study the design and manufacturing process of custom orthopedic braces has been chosen, which are made for children to correct congenital food deformity. First we searched for an appropriate 3D scanning application that can be used on low-cost tablets to be able to create the 3D model of the patient's feet on-site, at the visiting of the technician at the medical institute. Next we imported the model into Blender, a freely accessible 3D modelling application, and wrote some scripts in it, that help us to create the braces the fit the patient's feet. The scripts guide the technician to take some reference points on the model that are used for the calculations. Using a reference model of the braces, made by Catia, an industrial CAD designer tool, the final form of the braces are shaped by the scripts in a couple of seconds. At last the final model becomes exported in stl format and 3D printed.

Medical background: toe walking in childhood

Toe walking is a condition where a person or a child walks on the toes or the ball of the foot [1]. Toe walking is commonly seen in children who are just learning to walk. Many of the children outgrow the habit of toe walking. Children who continue toe walking, even after crossing their toddler years, usually do so out of their habit. If the child's growth and development is normal, then toe walking alone is not a cause for concern. Usually, toe walking is a habit, which a child develops when he/she learns to walk. In some cases, toe walking can occur due to some underlying medical conditions, such as cerebral palsy, short Achilles tendon, autism or muscular dystrophy.

Cerebral palsy is a disorder of movement, posture or muscle tone, which occurs as a result of injury or abnormal development in certain areas of the undeveloped brain, which is responsible for controlling the muscle function; due to which cerebral palsy can cause toe walking.

Achilles tendon connects the muscles of the lower leg to the back of the heel bone. If the Achilles tendon is very short, it may prevent the heel from touching the ground.

Autism is a condition consisting of complex array of disorders, which affects a child's ability to communicate and interact with others. Toe walking has also been associated with autism.

Muscular dystrophy is a genetic disease where the fibers of the muscles become very susceptible to damage and become weakened over time. Toe walking can sometimes occur in muscular dystrophy. Toe walking due to muscular dystrophy is more likely if the child has initially walked normally before starting to toe walk.

Fig. 2. Toe-walking [2]

Treatment for toe walking is not needed if the child is toe walking out of habit, as the child is likely to outgrow this habit. In such cases, the doctor will monitor the child's gait during office visits. If there is a physical problem, which is contributing to toe walking, then treatment comprises of:

- Leg braces or splints to the leg help in promoting a normal gait.
- Physical therapy consisting of gentle stretching of the muscles of the leg and foot also help in improving a child's gait.
- Serial casting. If the above treatment options, such as leg braces or physical therapy are not beneficial, then a series of below-the-knee casts are recommended, which progressively improve the ability of bringing the toes toward the shin.
- Surgery for toe walking is done if all the above conservative measures fail. Surgery is done to lengthen the tendons or muscles at the back of the lower leg.
- If the toe walking is caused due to medical conditions, such as autism, cerebral palsy or other health problems, then treatment is done according to the particular underlying medical condition.

During our investigation we focus to the treatments where custom braces are used for correcting foot deformity.

Fig. 3. Orthopedic braces [3]

The procedure of automated shaping leg braces

The aim of our project is creating a method that reduces the costs and facilitates the technician's work. This can be achieved by giving the technician cheap hardware and easy-to-use software tools to produce the braces, without unnecessarily using up expensive materials for the modelling. Keeping this in mind the following manufacturing process has been proposed to be investigated in terms of feasibility, cost and efficiency:

- At first the technician scans the lower leg and foot by means of a 3D camera attached to his/her mobile computer. The scanned point cloud gets converted to a 3D mesh, which then gets imported into a freely downloadable 3D modeling program, such as Blender.
- In the modeling program scripts are used to determine the parameters of the foot and lower leg that are necessary to automatically generate a 3D model of the brace. This is done with the help of the technician, who marks some reference points on the foot mesh that are then used up for the calculations.
- A script generates the 3D model of the brace according to the gained parameters. The technician has the possibility of some basic modifications on the generated model too.
- The final form of the brace is printed out with 3D printing technology.
- The technician mounts the non-printed parts, such as belts and joints, onto the brace.

3D scanning

For the 3D scanning a low-cost two-in-one device that can be used a laptop as well as a tablet has been purchased. The 3D camera we tried is an Intel RealSense D415 depth sensor (Fig. 3.).

Fig. 4. RealSense D415 depth sensor

After trying several 3D scanner applications the RecFusion program was chosen which gave acceptable result with the RealSense sensor. Fig. 4. shows a screenshot from the program during the procedure of 3D scanning. The little patient stands on his own or with the help of an assistant person in more severe cases of toe walking, and the technician walks around him or her and does the scanning. After a whole turn, pointing the scanner to the feet, the scanning provides enough data for shaping the 3D model of the legs. As the model creation is done on the fly, the resulted mesh can be checked on the right part of the application window immediately. The program needs powerful hardware resources to do this calculations that are not available in some low-cost tablets. Fortunately there is an option to take and save only the footage without the calculations and do the mesh creation later on a more powerful computer.

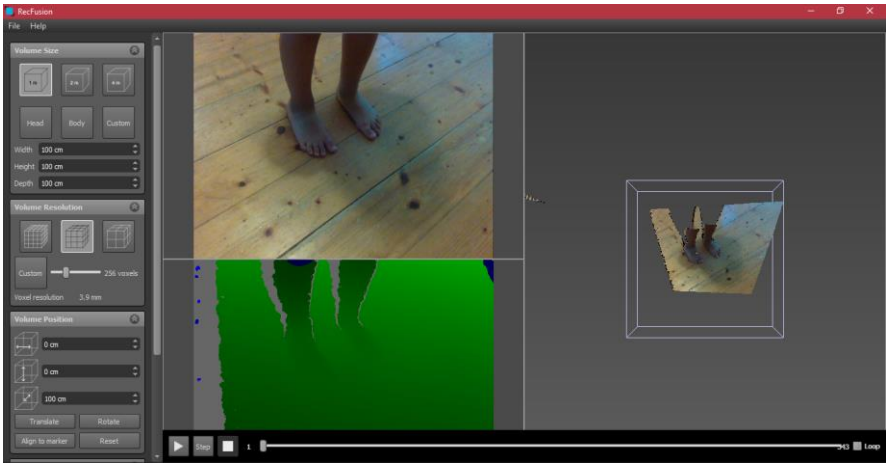

Fig. 5. Scanning with RecFusion

There is however another possibility for scanning even if a 3D scanner sensor is not available. The Autodesk ReCap Photo application uses plain photos, more than about 20 taken from the feet from different points of view, to create the 3D model. It uploads the photos on the cloud, and after the servers calculate the results, the 3D mesh can be downloaded and saved. In spite of the lack of 3D scanner sensor, the provided mesh has an excellent quality, though the process of taking many pictures from around the little, fidgeting patient isn't easy.

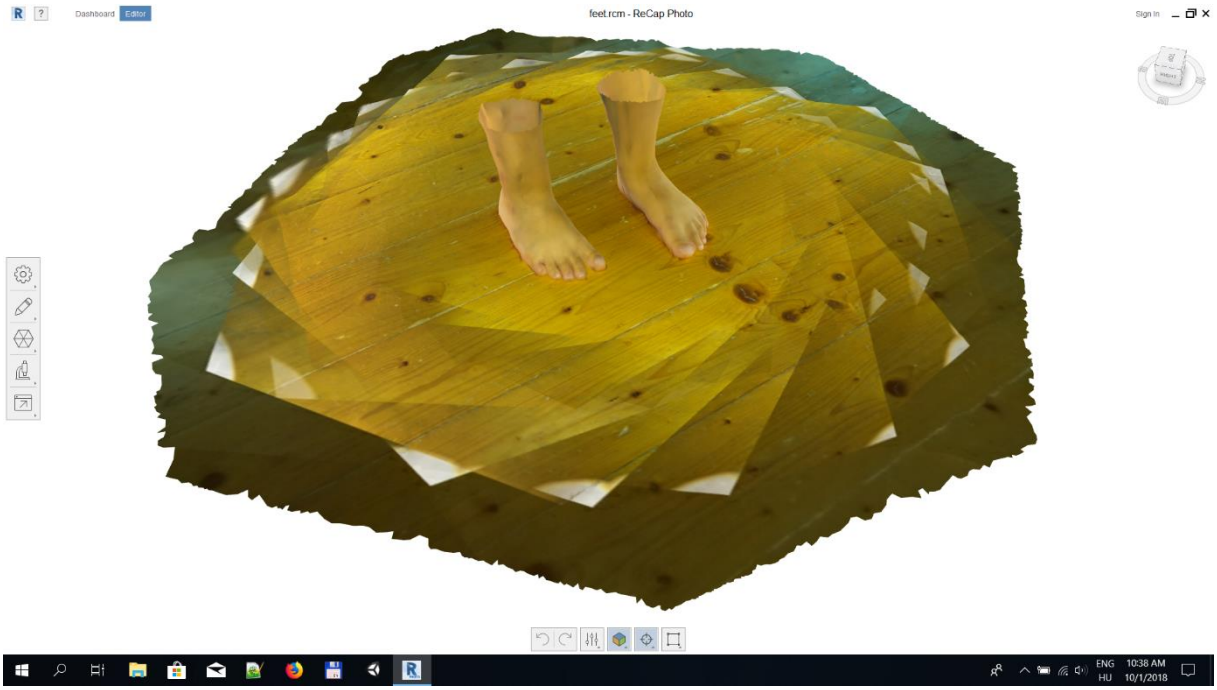

Fig. 6. Scanning results of Autodesk ReCap Photo

Automated creation of the Brace model

To create a pair of braces that fits the feet of the patient, a reference model has been shaped with Catia. This model is constructed in such a way that it can be easily adjusted to legs with different size and shape. According to the position of the inner and outer ankle parts and the length and width of the foot, the front, middle, back and upper parts of the brace can be scaled independently from each other, thus getting the final form of the brace model.

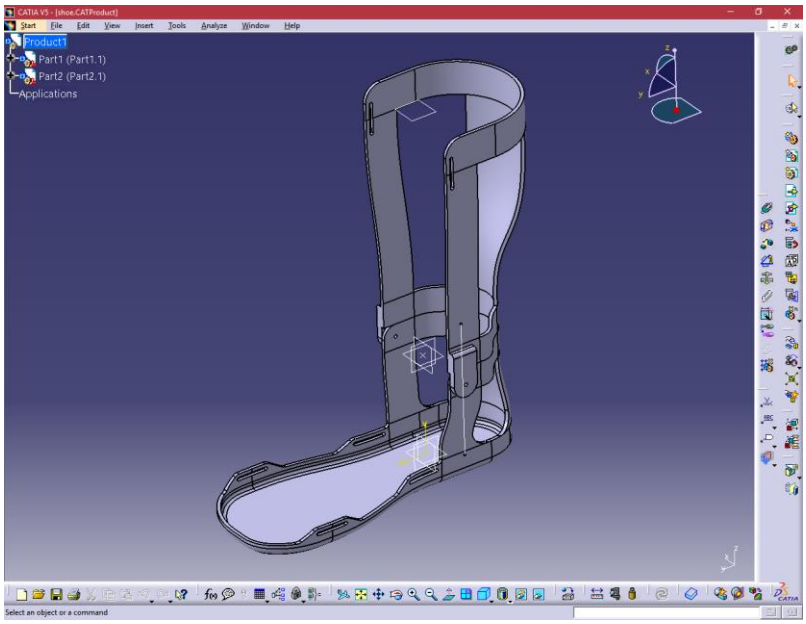

Fig. 7. The reference brace model in Catia

When we import the 3D model of the feet into Blender, two scripts guide us taking some reference points on the model that are required for the calculations, such as the inner and outer ankle parts, the heel, the toe tip, and the inner and outer points of the feet. Fig. 7. shows this process.

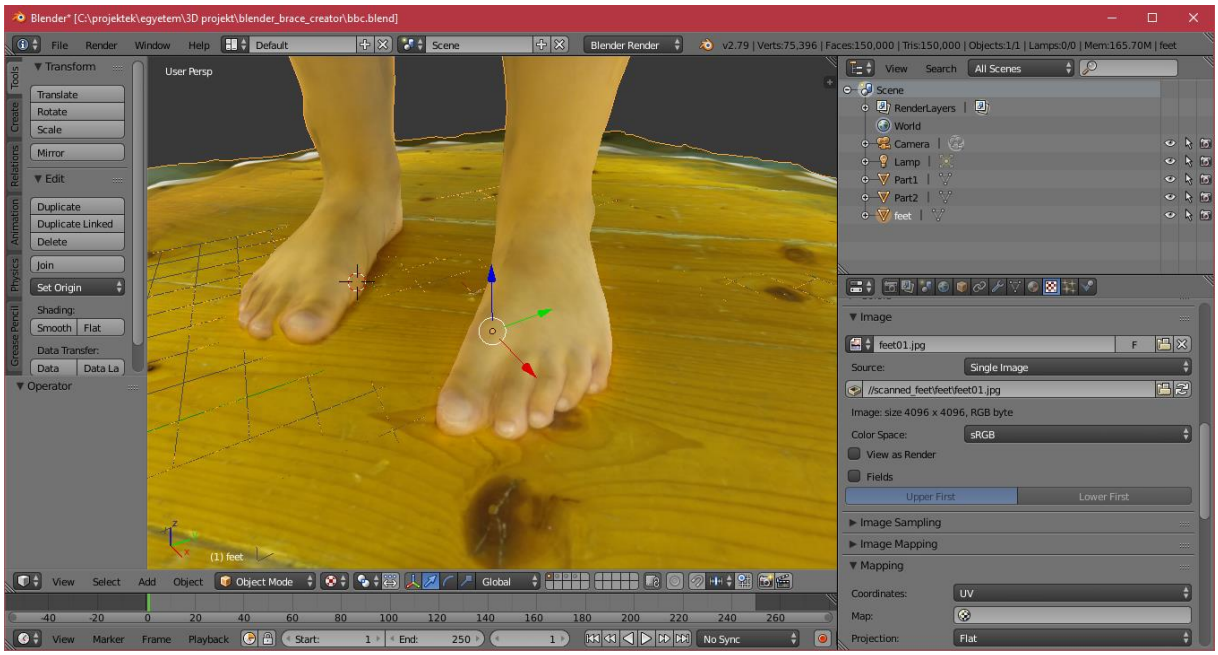

Fig. 8. Selecting the reference points in Blender

After taking all the points a script reshapes the reference model and the results, in the form of two independent models of the upper and lower parts of the brace, become available to be exported in stl format. At the time of submitting this paper the created brace models are being 3D printed, thus no pictures about them can be included here. Hopefully they can be already seen by the audience at the conference presentation.

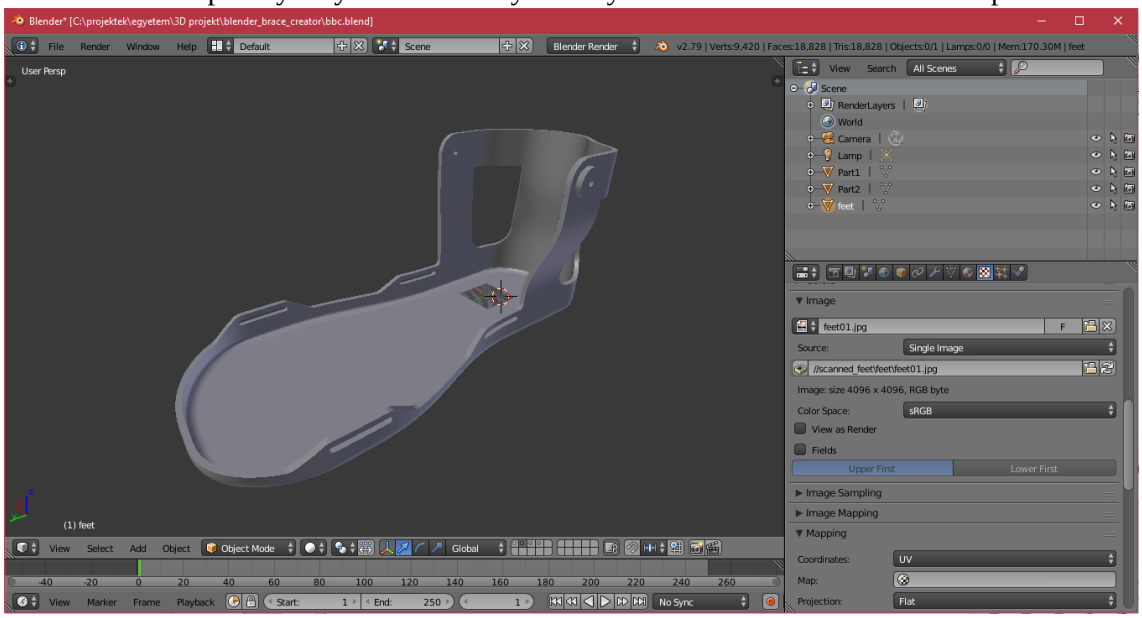

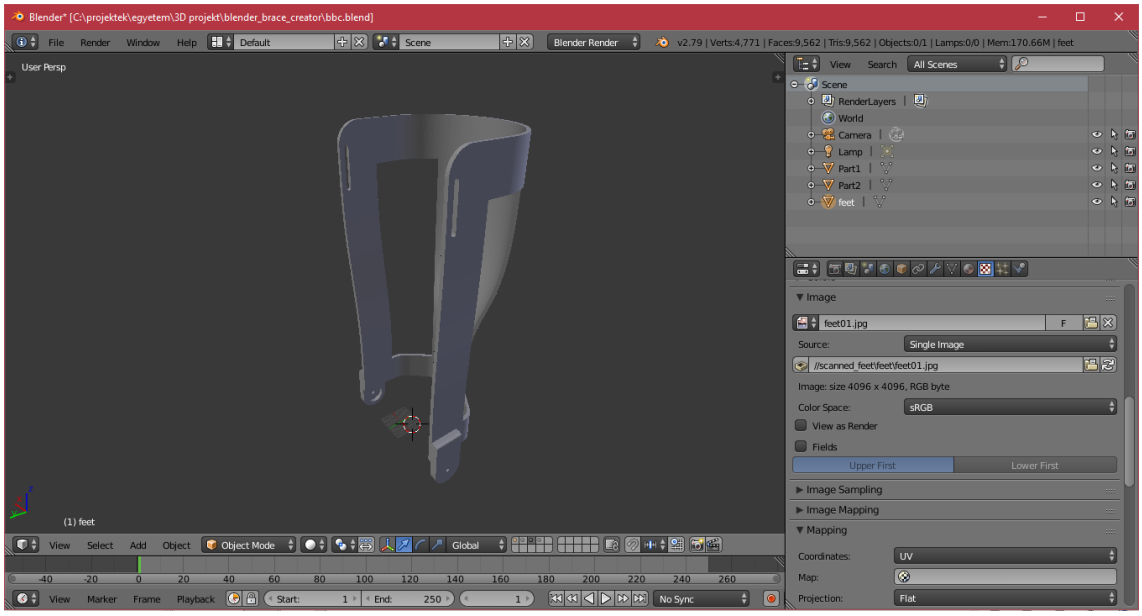

Fig. 9. The lower and upper parts of the reshaped brace model in Blender

Conclusions

To facilitate the work of technicians to make custom medical assistive devices, we are keeping to find the way of involving the latest 3D technologies. A procedure has been developed to help shaping orthopedic leg braces for children with toe walking. The procedure, though being still not ready for application in practice, shows how the available 3D technologies can replace the traditional steps in the creation of medical assistive devices, and constitutes the basis of further developments.

Acknowledgements

The project is sponsored by the GINOP 2.3.2-15-2016-00022 grant.

References

[1] Toe Walking: Causes, Treatment, Exercises, https://www.epainassist.com/joint-pain/foot-pain/toe-walking, accessed 9.18.2017

[2] Drobnjak L., Toe Walking: What causes it and how you can help your child, http://theinspiredtreehouse.com/child-development-toe-walking, accessed 9.18.2017

[3] Idiopathic toe-walking: Our Journey, http://www.oneprojectcloser.com/idiopathic-toe-walking-our-journey, accessed 9.18.2017

Additive Manufacturing of Metal Components by CMT Technology

Zoltán Meiszterics[1], Tamás Zsebe, Dávid Csonka, Roland Told and Gyula Vasvári
University of Pécs – Faculty of Engineering and Information Technology
Departent of Mechanical Engineering, Pécs, Hungary

Keywords: Additive manufacturing, CMT, Direct metal deposition, Metallic wire

Abstract: The aim of our project is to directly manufacture metal components with additive technology from alloyed AlMg4.5Mn7 wire by CMT technology. Our new welding equipment a Fronius TPS 320i C was used as a power source. First we weld beads on the plate with different parameters, investigating the effects of welding current and welding speed to the geometry of beads. From these results, we chose the proper parameters to the deposition of the multilayer beads. A thin wall was built from 55 rows and then we measured the geometry of it.

Introduction

Additive technologies were primarily known as rapid prototyping, but nowadays it is called 3D printing. This is a dynamically advancing area of manufacturing technology. Different versions of technologies use a wide range of materials for several applications. The novelty of additive technologies is the layer manufacturing which is enabled by the development of computers. This method widened the boundaries of designing and manufacturing technologies. Formerly hardly or not at all producible structures and parts can be easily made with this method. The base material could be fluid or solid - sheets, wire and grains. Heat source can be plasma, electron and laser beam or electrical arc. Our team had started a research project with a CO_2 laser power source in the field of wire additive manufacturing (WLAM), but because of high costs we have changed to Wire and Arc Additive Manufacturing (WAAM) when we got our new Fronius TPS 320i C welding equipment. Our aim is to produce metal parts in arbitrary shape within the capabilities of the technology.

Review of wire and arc additive manufacturing technologies

Wire feed additive manufacturing is a more environmentally friendly process than metal powder additive manufacturing technology, because it has higher material usage efficiency with up to 100% wire material deposited into the component and this process does not expose operators to the hazardous powder environment. Metal wires are lower in cost and more readily available than metal powders, having suitable attributes for additive manufacturing, making wire feed technology more cost-competitive [1].

Wire-feed additive manufacturing is a promising technology for producing larger components with moderate complexity, such as flanges or stiffened panels. However, there are a few challenges when using wire as the additive material, including residual stress and distortion from excessive heat input, relatively poor part accuracy caused by the “stair stepping” effect and poor surface finish of the produced parts. While depositing complex and large 2.5 D layers, the geometry-related process parameters (such as deposition width, layer thickness, wire diameter, wire feed rate and welding speed) must be carefully controlled to achieve required part dimension and surface finish. In addition, the residual stress-induced deformations are a major cause of loss in tolerance in wire-feed additive manufacturing of large components. The thermal history of the part during the deposition process is related to the process parameters (wire feed rate, welding speed and wire diameter) and the process planning (deposition pattern and sequences). [1].

Wire and arc additive manufacturing (WAAM) is another popular wire-feed AM technology. Several research groups have investigated the WAAM process using gas metal arc welding (GMAW), gas tungsten arc welding (GTAW) or plasma arc welding (PAW) as a heat source [1].

There are four primary methods of metal transfer in GMAW, called globular, short-circuiting, spray and pulsed-spray, each has distinct features. Besides, cold metal transfer (CMT), a modified GMAW variant based on controlled dip transfer mode mechanism, has also been widely implemented for AM processes, due to its high deposition rate with and low heat input [1].

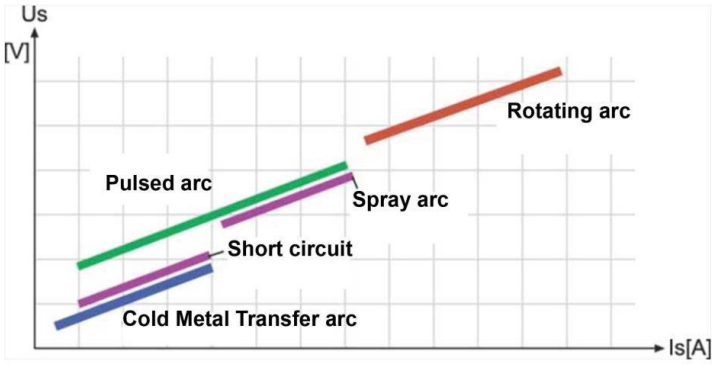

Fig. 10. Comparison of voltages and currents used in each metal transfer modes [6]

Whenever possible, MIG is the process of choice: the wire is the consumable electrode, and its coaxiality with the welding torch results in easier tool path. Tungsten inert gas, or plasma arc welding rely on external wire feeding; for deposition consistency, the wire must be fed always from the same direction, which requires rotation of the torch, thus complicating robot programming [3].

There are a few technical challenges yet to be resolved, including the residual stress and distortion from excessive heat input, relatively poor part accuracy caused by the "stair stepping" effect and poor surface finish. [1].

A plane of symmetry is identified within the volume of the component; the initial substrate will coincide with this plane. Using a part rotator, the deposition of the layers is alternated on the two sides of the substrate; the layer deposited on one side produces stresses, which balance those produced on the other side. Whenever a plane of symmetry cannot be identified, the substrate will be aligned to the plane, which separates the two resulting volumes in the most balanced way [3].

Among the various arc processes that can be used for wire melting, the cold metal transfer (CMT) process seems to be one of the more suited for WAAM, thanks to its controlled current waveform and filler wire feeding that allow to obtain regular deposited weld bead [2].

Different CMT variants on the porosity in the WAAM aluminium thin wall structure, adding a pulsing cycle to the standard CMT helps the control of porosity [4].

Additive manufacturing of metals has been made with a non-expensive system based on the integration of CMT welding technology and CNC milling machine. It's a smart cost solution for developing and testing new components in comparison with only machining process, laser or electron beam technologies [5].

Designing and manufacturing of torch holder

During the design of the torch holder we have taken into consideration the next aspects: stable, strict holding, quick, simple adjusting and the use of standard components, if possible. Some parts of our construction was made with Fused Deposition Modelling (FDM) process by our 3D printing device. The production of the parts was done in the workshops of the University.

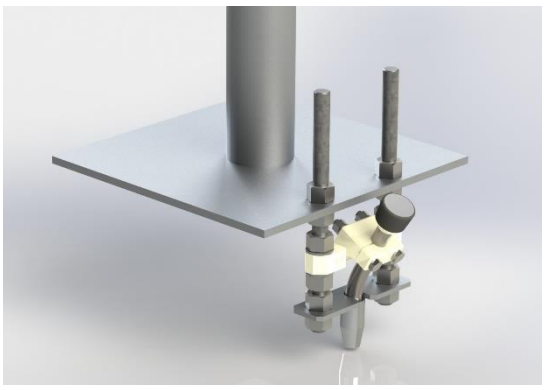

Fig. 11. CAD model of torch holder

Parts of the setup

The basis of our setup is a Fronius TPS 320i C welding machine. The welding torch was fixed on the laser cutting machine, beside the cutting head, above the two-saddled milling machine table. Under the printing process the table actuates the substrate in the direction of X and Y axis, while in the direction of Z axis the torch keeps a constant distance from the surface of the part. At our request, the supplier built in a control cable, which enables the automatic start and stop of the printing process. We connected the welding machine with the controller of the laser. We programmed the motions of the table into this controller and when it starts moving, the controller sends the beginning sign to the welding equipment.

Fig. 12. 3D printing device

The material of the 5 mm thick plates was AlMg4.5Mn7 alloy. Under the printing process, the layers of beads were built on these substrates. This material is a medium strength, non-heat treatable aluminum alloy with excellent corrosion properties and relatively low formability. We used the same quality, 1.2 mm diameter welding wire for the deposition.

The main mechanical properties of the wire: R_m>275 MPa, $R_{p0.2}$>125, E=70 GPa, A_5>17%.

Cold Metal Transfer technology

This new process, derived from the conventional gas metal arc welding (GMAW) process, has been initially developed for minimizing the welding heat input. The CMT process couples a specific electrical current waveform, which allows to form a molten metal drop at the filler wire tip and to control its growth, to an alternating feeding of the filler wire, which allows the deposit of the metal drop with a minimal heat input [2].

The low heat input made this technology the most suitable for the 3D metal printing process among the arc welding methods.

Fig. 13. Metal drop at the filler wire tip

This configuration requires, however, the combined choice of 15 main parameters to control the melting of the filler wire tip and its deposit on the form of molten drops. These parameters can be classified into three classes, the first ones relative to the ignition phase, the second to the deposit phase, and the last ones to the end phase of the deposit [2].

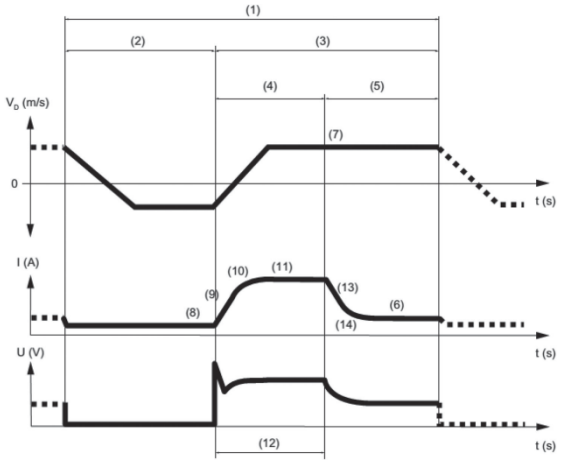

Fig. 14. Schematic representation of feeding rate, current and voltage waveform [2]

The first phase, the Arcing phase (4), is characterized by an increase in voltage and a significant increase in welding current. In this phase a molten droplet is formed on the end of the wire electrode and a weld pool is created. After a set duration of time, the welding current decreases (5). This dropping in the welding current prevents the globular transfer mode to occur. This value of current is maintained until the short circuit begins. Finally, in the short circuit phase (2), the wire electrode is fed forward contacting the weld pool and the voltage drops to zero. In this moment, in conventional MIG/MAG, the current rises and the electrical pinching forces separate the electrode from the weld pool. Contrary, in CMT process, the current stays at low levels and the wire is sent in a backward motion and a force is transmitted that separates the electrode from the welding pool. The arc is then reignited and the cycle repeats [6].

Single bead tests

The purpose of making single beads was to map the effect of changing major technology parameters on bead geometry. 56 beads were deposited with different welding parameters. We measured width, height and the area of cross sections of each welt. The shape of cross section was approximated with ellipse. The main parameters are: welding current, arc voltage, wire feeding rate and traverse speed of substrate.

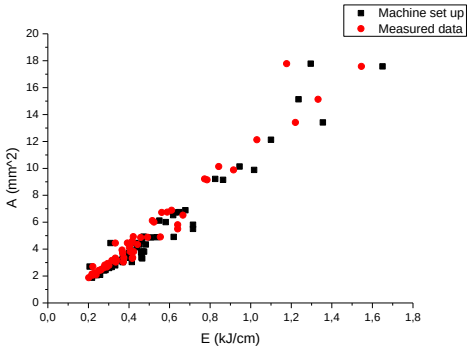

Fig. 15. Cross sections of bead on plates in function of heat input

When we have made probes, one serious problem has occurred: the size of the beginning and ending point of the seam. At the beginning and ending points, the cross section of the bead has to be near equal to the rest of the seam. If it isn't equal in size, we couldn't print complex 3D forms properly, because the different geometry in several layers may cause cumulated errors.

Multilayer bead tests

There are some different options of using multilayer deposition: these thin walls can be deposited vertically or angularly. Solid blocks can be built up from partially overlapped rows in several layers.

Table 1. Process parameters of deposited beads

rows	I [A]	U [V]	v_w [m/min]	Q [kJ]	v_{tr} [m/min]	E [kJ/cm]
1.	126-128	13-13.4	4.8-5	8.7-9	1.8	0.738
2.	79-80	12.8-13.1	6-6.1	5.4-5.6	1.8	0.458
3-55.	64-66	13.1-14	7.3-7.6	4.4-4.6	1.8	0.375

We started or multilayer experiments with deposition of thin walls. We used increased heat input in case of the first row, because the seam will be contacted to a cold substrate which cools down it immediately. The second one needs less heat input and we decrease it further for the third, but the parameters, including heat input remain the same after that.

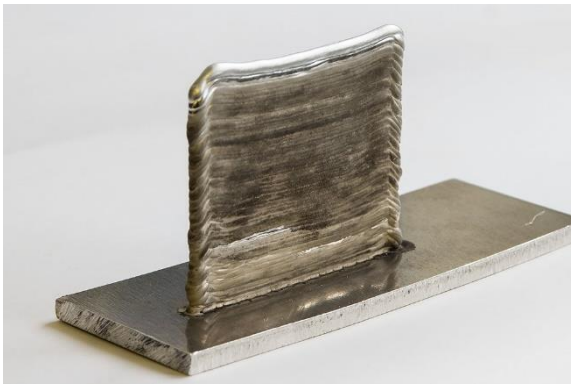

Fig. 16. Thin wall from 55 deposited layers

We built a thin wall of 55 layers successfully, and also built 3 samples with longer rows of 30 layers with the same technology for tensile test.

Table 2. Dimensions of deposited walls

Layers No.	Wall height H [mm]	Wall width B [mm]	Average layer height h [mm]
55	58.1	3.2	1.06
30	31.2	3.2	1.04
30	31	3.25	1.03
30	30.6	3.35	1.02

Tensile tests

We made 3 tensile test specimens from the 30 layer samples parallel with the direction of the rows. The results of the strength and strain properties have been compared with the parameters of the welding wire.

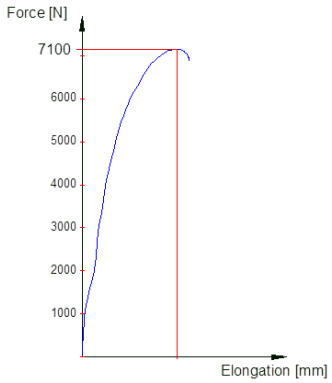

Fig. 17. Force elongation diagram of specimen 3

Table 3. Results of tensile tests

Specimen No.	F [N]	ΔL [mm]	A_5 [%]	Z [%]	R_m [MPa]
1.	6950	6.4	19.9	23.8	217
2.	7130	7.4	23	25	219.4
3.	7100	7.1	22.1	24.3	216.3

The tensile strength was around 80 percent of the wire's strength and the strain exceeded the minimal requirements.

Conclusions

The experimental setup has been successfully put into operation. We connected the welding machine with the controller of the laser and when it started moving, the controller sent the beginning sign to the welding equipment. We built a 55 layer wall with success. We performed tensile tests on the samples we built with this technology. The tensile strength was almost identical to the wire's strength and the strain exceeded the minimal requirements. It turned out from these experiments, that we have to deal with the setup of the starting and the ending points of the beads in the future.

Future plans

Our aim with this project is to manufacture parts with any geometry and also to build more complex objects with better accuracy. For this, we need to solve some minor problems with the technology. One of our most important task is the problem of the starting, ending and restarting. We have to find a way to make these points reach the same size as the seam.

To fully understand the printing process, we need to measure the current and the voltage in high resolution in real time with an oscilloscope. We need to measure the wire feed rate, too.

Optical observation would be a great help with the analysis of the process. Firstly, we could use a camera with proper timing, but on the long run, a high-speed camera would be better. Both methods need a light source, a diode laser, which is able to properly illuminate the process. Furthermore, we can use it in the observation of arc and laser welding.

We would like to combine the CMT technology with the laser beam technology. This could be a possible solution for the starting point problems and the fusion of the layers could have been done with less heat input. We could also use the two technologies separately in the manufacturing process of one part. We could build the simpler and bigger parts with the CMT technology and the more complex ones with laser. To achieve this, we need to build a new wire feeder.

Acknowledgement

Special thanks to all member of our team for their work.

Supporting companies during implementation:

- MATRO Kft.
- Spizer Silo Kft
- Weldotherm Hőtechnikai és Kereskedelmi Kft

REFERENCES

[1] Donhong Ding, Zenxi Pan, Dominic Cuiuri, Huijun Li, "Wire feed additive manufacturing of metal components: technologies, developments and future interests," *International Journal of Advanced Technology* May 2015 DOI 10.1007/s00170-015-7077-3

[2] A. Gomez Ortega, L. Corona Galvan, F. Deschaux-Beaume, B. Mezrag and S. Rouquette, "Effect of process parameters on the quality of aluminium alloy Al5Si deposits in wire and arc additive manufacturing using a cold metal transfer process," *LMGC, Univ. Montpellier, CNRS, Montpellier, France*

[3] S. W. Williams, F. Martina*, A. C. Addison, J. Ding, G. Pardal and P. Colegrove, "Wire and Arc Additive Manufacturing," *Materials Science and Technology* Vol. 32, Iss. 7, pp. 641-647

[4] Baoqiang Cong, Zewu Qi, Bojin Qi, Hongye Sun, Gang Zhao and Jialuo Ding, "A Comparative Study of Additively Manufactured Thin Wall and Block Structure with Al-6.3%Cu Alloy Using Cold Metal Transfer Process," *Appl. Sci. 2017, 7, 275.*

[5] J. Gonzáleza, I. Rodríguezb, J-L. Prado-Cerqueirac, J.L. Diéguezd, A. Pereira "Additive manufacturing with GMAW welding and CMT technology" *Procedia Manufacturing 13 (2017) 840–847*

[6] Inês Planas Meunier Santos Pinto "Additive Manufacturing of Nickel components using CMT process" *MSC thesis in Mechanical Engineering, May 2015*

From Parchment to 3D to HTML: The Use of the 3D and the Web in Architectural History Research (a case study)

Zoltán Bereczki, PhD[1]
University of Debrecen, Faculty of Engineering, Debrecen, Hungary

Keywords: architectural history, Middle Ages, Gothic, construction, Vienna, GitHub, Jekyll, WebGL, Rhinoceros 3D, open source.

Abstract: The construction of Gothic church towers with carved stone spires and often with significant height required the most advanced technology and financial support of their age, and the application of advanced machines was also inevitable for it. In my PhD thesis defended in 2017 I attempted to reconstruct the process of a 15th-century tower construction, including the main auxiliary structures: scaffoldings and machinery, on the example of the unrealised north tower of the St. Stephen's church in Vienna, with the use of mostly contemporary sources. [1] While creating the images for the final version of the thesis I faced the problem that the paper as a medium is only able to communicate fragments of the information contained by the 3D model. This project is the result of this realisation, so it serves as an extension of the printed thesis: I created an online visualisation of the model with animations, embedded models, and links to the most important and online available drawn sources.

Introduction

One of the main questions of the research of the mediæval technical drawings is whether they served as a modern blueprint or not; so was their main purpose to make possible the realisation of a structure (machine, building), or something else (education, representation, etc). [2] [3] [4] The most reassuring way to answer this question would be conducting a lifesize experiment: to construct the structures relying only on the drawings representing them. Since there is hardly an opportunity to achieve this, 3D-modelling emerges as a solution.

It is important to emphasise – as it is discussed in several papers written by Norbert Nußbaum of the University of Cologne –, that the Gothic construction praxis cannot be generalised. While the forms could spread on paper or parchment, the technical details, solutions could not. [5] So not only I do not state that a particular tower was constructed this way, but I also do not state that Gothic towers were generally constructed this way: my 3D model and the resulting drawing series and website illustrate a possible solution, based almost exclusively on contemporary sources. As far as I know a similar representation of a Gothic tower's construction – illustrating not only the tower, but also the auxiliary structures, based on historic sources – wasn't published in the literature yet. "Fig. 1."

Fig. 18. The five main phases of a Gothic tower's construction. Drawing by author.

The 3D reconstruction

During my research I modelled the partially realised north tower of the St. Stephan's church in Vienna using exclusively its contemporary (15th-century) plans. I choose wittingly an unrealised tower, as I wanted to avoid any possible misunderstanding. I do not want to introduce how a particular tower was built (this would be impossible), but how a tower could have been constructed using the instruments in the discussed sources.

For the construction of a tower the scaffolding and machinery are the most important auxiliary structures. Accordingly, my model about the construction consists of three main parts: the tower itself, the scaffoldings, and the machines. The detailed description of the non-written sources used extends beyond the scope of this abstract, so here I merely list the most important ones.

The two most complete plans of the Viennese north tower are in the collection of the Wien Museum Karlsplatz: the drawing no. 105.064 (a floor plan) and the drawing no. 105.067 (an elevation). [6] I used these two drawings for my model. The two are mostly coherent. Where conflict emerged, I considered the floor plan relevant. Since my goal was to reconstruct a structure based solely on original designs, I used only the drawings for the model; photos of the realised parts of the tower were used only for the interpretation of the drawings. Thus, the parts that are not visible on the drawings and can not be deduced (mostly the east and west facades of the ground floor) are only schematic.

Discussing the machines, the mediæval machine drawings survived almost only in warfare-themed manuscripts. Notable exception is the portfolio of the Strasbourg master Hans Hammer, where many machine drawings can be found, likely in connection with the tower plans of the master. [4] I used mainly this manuscript for the reconstruction of the machines.

The survived contemporary drawings about scaffoldings are almost exclusively book illuminations and paintings, these were my main sources for the modelling of the scaffolding. [7] An additional source available from the Modern Age, but before the age of industrialisation is the detailed drawing and description of the scaffolding used during the early 19th-century reconstruction of the top of the south spire at the St. Stephen’s church. [8] Further important sources of information were the surviving or reconstructable scaffoldings inside of Gothic towers and the related literature. [9] [10] [11]

My modelling software of choice was Rhinoceros 3D. The modelling of the tower was carried out by drawing the outlines of the different storeys on the floor plan from one level to another, starting from the outside. It was possible because of a unique characteristic of the Gothic floor plans: they represent the different levels (every storey) of the whole structure on one drawing. When the contour of one level was ready, I determined the height of the contour on the elevation drawing and raised up the contour line to the corresponding height; then I filled up the space between the contours with the 3D structure, also based on the elevation drawing. "Fig. 2."

Fig. 1. The outlines of the different storeys at their appropriate height. Drawing by author.

During the modelling of the tower I of course applied simplifications: I modelled only the geometrical forms of the intricate stone carvings (finials, foliage), just like in Matthäus Roriczer's contemporary book on construction a pinnacle [12]; and I did not display any tracery and vaults. "Fig. 3."

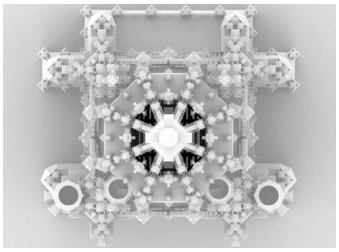

Fig. 2. Orthographic top view of the model. Drawing by author.

I have modelled the construction in five main stages. In the first stage the lower, quadratic levels of the tower are finished; in the second stage the belfry is under construction; the third displays the construction of the octagon, the fourth the construction of the openwork spire, and the last one displays the placement of the top finial. "Fig. 1."

For each phase, at first I modelled the tower to the desired height, using the mediaeval drawings (floor plan, elevation); then I designed a possible solution for the scaffolding, based on the discussed sources; finally I put Hans Hammer's machines to the appropriate places. "Fig. 4."

Fig. 3. The scaffoldings of the model. Drawing by author.

The online representation

In my thesis I illustrate the construction with five phases. Consequently, the on-line presentation consists of five subpages.

The structure of the pages is the following:

- a short animation about the discussed phase
- embedded models
    - the entire structure (building, machinery, scaffoldings)
    - separate windows for each machine used in this phase
- the sources of archive drawings and plans used (in the case of the online available drawings with link)
- references

The main content of each site is the embedded WebGL-window with the model of that phase.

Regarding the technical implementation the following aspects were important for me: plugin-free operation; the possibility of simple, offline editing; and version tracking. Accordingly, the embedded models use WebGL, the site is written in Markdown using a simple text editor, and is hosted on GitHub Pages.

WebGL is developed by the Khronos Group. According to the official definition, "WebGL is a cross-platform, royalty-free web standard for a low-level 3D graphics API based on OpenGL ES, exposed to ECMAScript via the HTML5 Canvas element." [13] According to Wikipedia, "WebGL evolved out of the Canvas 3D experiments started by Vladimir Vukićević at Mozilla. Vukićević first demonstrated a Canvas 3D prototype in 2006. […] In early 2009, the non-profit technology consortium Khronos Group started the WebGL Working Group, with initial participation from Apple, Google, Mozilla, Opera, and others. Version 1.0 of the WebGL specification was released March 2011." [14] It is supported by modern web browsers (such as Apple Safari, Google Chrome, Mozilla Firefox, Opera) without installing any plug-ins, just like the most popular mobile browsers (Safari, Chrome, Firefox). The Khronos Group also maintains a simple test page where it's easy to check if a browser is WebGL-compatible: https://get.webgl.org. If so, a rotating cube can be seen.

To export the Rhino model in WebGL format, I used the Iris plugin for Rhino developed by Luis E. Fraguada. The plugin generates JSON data from a Rhino model that is parseable and viewable through WebGL in a modern web browser, and can be downloaded from the following URL: https://mcneel.github.io/Iris. JSON (http://json.org) is an open-source format derived from JavaScript. Iris depends on the following libraries:

- Three.js
- Bootstrap
- Tween.js
- jQuery

- JSON.net

Iris is able to export a so-called Web Archive from the model, which is a local folder with the following content:

- Archive (Named during export)
    - index.html (the html page for the Iris Scene)
    - app
        - iris.min.js (the Iris WebApp Javascript Code)
    - data
        - data.json (the exported model in Three.js json format)
    - ui (this is the default UI template that ships with Iris)
        - css
            - styles.min.css (the css required by the ui)
    - js
        - ui.min.js (the javascript required for the ui)

Embedding the index.html into a webpage as an iframe results in a 3D window, containing a User Interface (UI) in the corner with a number of buttons. The model loads from the *data* folder, and the UI is loaded from the *ui* and *js* folders. "Fig. 5."

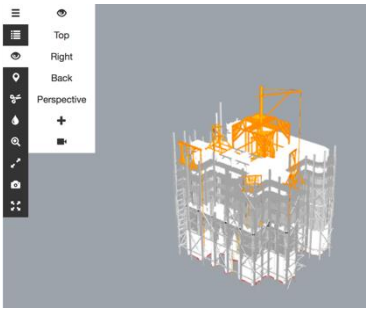

Fig. 4. The WebGL window of the first phase with the Iris UI.

The version number of the plugin is currently 0.6.0.2, so its operation is not perfect. The UI can not be edited, so it contains a number of (for me) unnecessary items (for example Planes, Materials, or Positions). To avoid the visitors to lose focus I have included a small manual next to the main 3D window discussing most important UI elements. These are the following:

- Zoom Extents
- Views, including the pre-saved views I consider important

The most important shortcuts for navigation are also included:

- Left mouse button: pan around the scene
- Right mouse button: orbits the scene camera
- Middle mouse wheel: zooms
- Zooming extents - ‘z’
- Zooming selected - ‘s’

The custom views displayed in the 'Views' menu can be defined in Rhinocheros itself, using the NamedView command. For each of my embedded models I defined views that point to some important detail. The Iris UI displays the standard views too (Top, Left, etc.).

I used Jekyll and Github Pages to create the online site. The main workflow of this technique is the following. At first, the content of the entire website is created on the local computer with a plain text editor, using Markdown. According to its official website, "Markdown is a text-to-HTML conversion tool for web writers." [15] By now, Markdown is much more than this: it has become a de-facto standard, and the documents written in Markdown can be exported to almost any text format with the open source application called Pandoc. Pandoc is developed by John MacFarlane, Professor of Philosophy at the University of California, Berkeley; and can be downloaded from the following URL: https://pandoc.org.

The site created in Markdown is translated into html by Jekyll (https://jekyllrb.com), an open-source server-side application. The result is a lightweight static website that does not require any database. For Jekyll to be able to do its job, the page structure and the markdown files themselves has to be created according to the Jekyll conventions (that means the proper folder system, the corresponding filenames, and the creation of the corresponding YAML headers for each markdown file).

Besides the simple, local editing and the static website generation Jekyll has another important advantage: it is used by GitHub Pages, the web hosting solution of GitHub. The workflow of the online publication is the following. At first, a local Git repository has to be created with the content of the local files of the website. Git is an open source, de-facto standard version control system, and it can be installed on every major desktop operating system. When the local edits are finished, the changes have to be committed to the local Git repository, then synced to the respective online GitHub repository. When the appropriate switch is turned on in the repository's settings on the online GitHub interface, the website is generated by Jekyll running on the GitHub server. The site will still be edited and updated locally: the Markdown files and the folder structure can be edited on the local computer, and when the edits are done, the repository has to be again synced to GitHub where Jekyll monitors the changes and generates the updated static website. This way the version controlling occurs almost unnoticed, because Git (and GitHub) is basically a version-controlling system. Actually, each synchronisation is a commit to the main online repository.

The resulting website is a detailed online interpretation of the 3D model, where the intricate spatial structure can be observed interactively, in detail.

Here is the URL of the website:
https://zbereczki.github.io/gothic-construction/,
and the URL of the underlying GitHub repository:
https://github.com/zBereczki/gothic-construction.

Conclusions

The modelling based on contemporary sources has shown that with the exceptions of some contradictions and hidden parts, the contemporary plans of the north tower in Vienna carried enough information to build up the structure in 3D. Around and inside the 3D-model, based on historic representations and survived structures I could construct a scaffolding the way it would be constructible using technology available in the Middle Ages. With this scaffolding the construction of the tower would be possible. By placing Hans Hammer’s machines, as well as the clever ladders of the portfolio on the model I was able to clarify their possible application modes.

The mediæval drawings used for the project are definitely workshop drawings, "blueprints": relying on them and only them it was possible to build up in 3D both the complex building and the elaborate machines. For the presentation the Web as a medium was much more appropriate than printing. In the printed version of my dissertation I could only include images in a limited number and size, and they (obviously) depict the model only from a certain angle, in a certain size. The web-based representation, on the other hand, can be rotated and zoomed; and I could define the important views with Rhino and display them with the Iris UI.

For the whole picture it has to be mentioned, that the technology does not work smoothly yet. On one hand there are errors in the operation of Iris. Probably the most annoying is that it often does not load the predefined view, so either an empty window is displayed, or only a part of the model is visible. So I had to include on every page the warning "if the models are not visible or not centered, press *Z*". In addition, the complete, very complex model requires powerful hardware to render. I cannot tell the exact hardware requirements, just the results of some testing. A 2017 MacBook Pro (Intel Iris Plus Graphics 640 1536 MB) was able to render the site without any problem. A much older and weaker 2013 Macbook Air (Intel HD Graphics 5000 1536 MB) could also do the job. I did some mobile testing also, with worse results. The iPhone SE was the most powerful phone available for testing, but it could only display the models of the machines, not the tower model.

REFERENCES

[1] Z. Bereczki, “Gótikus tornyok építésének kérdéséhez. Mit mondanak a megvalósult épületek a tervezésről, mit mondanak a tervek a megvalósulásról?” (In English: “Addressing the question of the construction of Gothic towers. What do realised buildings tell us about design, what do designs tell us about realisation?”) Ph.D. thesis, University of Pécs, Faculty of Engineering and Information Technology, Breuer Marcell Doctoral School of Architecture, 2017. Unpublished.

[2] F. Bucher, “Design in Gothic Architecture: A Preliminary Assessment,” *Journal of the Society of Architectural Historians*, vol. 27, no. 1, pp. 49–71, 1968.

[3] W. Lefèvre, Ed., *Picturing machines 1400–1700*. Cambridge, Mass.: MIT Press, 2004.

[4] Z. Bereczki, “The machine drawings of Hans Hammer in the context of the contemporary machine representations,” *Pollack Periodica*, vol. 10, no. 3, pp. 165–174, Oct. 2015.

[5] N. Nussbaum, “Planning and Building without Writing: Questions of Communication in Gothic Masons’ Lodges,” in *Architecture, liturgy and identity: Liber amicorum Paul Crossley*, Turnhout: Brepols, 2011, pp. 137–145.

[6] M. Kronberger, Ed., *Der Dombau von St. Stephan. Die Originalpläne aus dem Mittelalter*. Wien: Metroverlag, 2011.

[7] G. Binding, *Der Mittelalterliche Baubetrieb in zeitgenössischen Darstellungen*. Darmstadt: Wissenschaftliche Buchgesellschaft, 2001.

[8] J. Trost, “Der Umbau der oberen Pyramide des Wiener Stephansthurmes,” *Allgemeine Bauzeitung*, vol. 8, pp. 5–17, 1843.

[9] T. Tatton-Brown, “Building the tower and spire of Salisbury Cathedral,” in *The engineering of medieval cathedrals*, Aldershot: Ashgate Variorum, 1997, pp. 327–349.

[10] A. R. Jones, “The Salisbury Spire Scaffold Debate,” *Avista Forum Journal*, vol. 15, no. 1, pp. 8–17, 2005.

[11] P. S. C. Caston, *Spätmittelalterliche Vierungstürme im deutschsprachigen Raum: Konstruktion und Baugeschichte*. Petersberg: Imhof, 1997.

[12] M. Roriczer, *Das Büchlein von der fialen Gerechtigkeit*, Faksz. Hürtgenwald: Pressler, 1999.

[13] The Khronos Group Inc, “WebGL Overview.” https://www.khronos.org/webgl/ 2018.

[14] Wikipedia, “WebGL.” https://en.wikipedia.org/wiki/WebGL 2018.

[15] J. Gruber, “Markdown.” https://daringfireball.net/projects/markdown/ 2004.

Poster Session

3D Geometry Editing for Numerical Modeling Based on Geosciences Data (in Hungarian language)

Gábor Szujó, Máté Farkas, Gábor Somodi
University of Pécs – Department of Geology and Meteorology, Pécs, Hungary

Földtudományi adatokon alapuló 3D geometria szerkesztés numerikus modellezés céljából

Szujó Gábor [1,2], Farkas Máté [2], Somodi Gábor [2]
[1]Pécsi Tudományegyetem, Földtani és Meteorológiai Tanszék, 7624 Pécs, Ifjúság u. 6; sujo21@gamma.ttk.pte.hu,
[2]Kőmérő Kft., 7633 Pécs, Esztergár Lajos u. 19; szujogabor@komero.hu, farkasmate@komero.hu, somodigabor@komero.hu

Bevezetés

A geológiában kiemelten fontos a földtani képződmények geometriai ismerete. Amennyiben elég adat áll rendelkezésünkre, úgy GIS (Geographical Information System) szoftverben 3D geometriákat hozhatunk létre. A numerikus modellezéshez a GIS-ből származó szabálytalan, bonyolult geometriák topológiáját újra kell értelmezni. A geometriák belső topológiájának szabályos kialakítása számos szakterületen komoly problémát jelent. A munkafolyamatot és a problémát, valamint egy lehetséges megoldást egy vetőfelszín és egy felszín alatti üreg példáján keresztül mutatja be jelen munka.

3D vetőfelszín

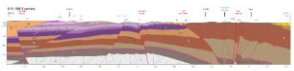

Földtani keresztszelvény

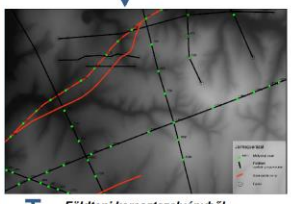

Földtani keresztszelvényből származó Z koordináták rögzítése

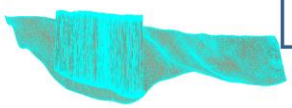

Interpolált vetőfelszín

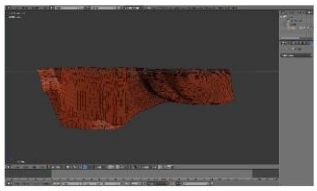

Geometria újraépítése CG programban

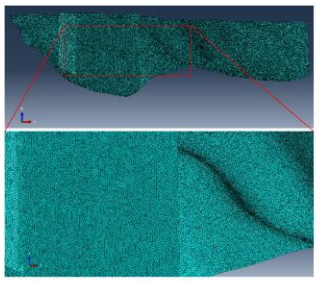

Numerikus modellező programban (ABAQUS) hálózott geometria

Térinformatikai forrásadatok

- Földtani térképek
- Geodéziai szelvények
- Földtani keresztszelvények (kutatófúrás és geofizikai szelvény alapján)
- Valós 3D fotogrammetriai felület modellek a vágathajtás előrehaladásához kötve

Adatelőkészítés

- Z értékek leolvasása és rögzítése X és Y koordinátákhoz a szelvény nyomvonalak mentén
- Töréspontok lekérése, összeolvasztása
- Adattisztítás

Adatfeldolgozás

- Spline típusú interpoláció a bevitt Z adatokon
- A tisztított pont adatsor háromdimenziós térben számított legkisebb kiterjedése, a pontokra illesztett térfogat kalkulációja
- Az eredményként kapott raszteres állomány konverziója polygonZ shapefile-ba

Geometria újraépítése

- A szabálytalan elrendeződésű poligonok újra topologizálása 3D CG (Computer Graphics) szoftverben, szabályosan elhelyezkedő poligonok illesztése a felszínre
- A test CG szoftverben történő újra topologizálása

VAGY

- Újrahálózási funkció, ami kissé megváltoztatja az alap geometriát

Hálózás modellező szoftverben

- CG szoftverből érkező geometria beolvasása az ABAQUS modellező programba, a pontatlan, hibás élek javítása
- Élek mentén a hálózás kiinduló csomópontjainak újraszámítása, hálósűrűség meghatározása
- A modellezési célnak megfelelő hálózási módszer kiválasztása

Konklúzió

A bemutatott szabálytalan geometriák felkészítése numerikus modellezésre számos egyéb szakterületen is hasznosítható módszer lehet. A részletgazdag geometriák pontosabb eredményt adnak a modellszámítás során.

Felszín alatti 3D üreg

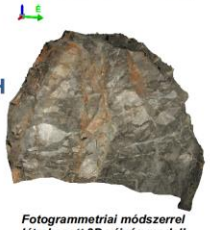

Fotogrammetriai módszerrel létrehozott 3D vájvég modell

A geodéziai szelvények és vájvég modellek egységesített töréspontjai

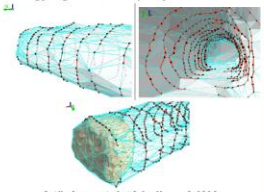

A töréspontok térbeli pozícióján alapuló test kalkulációja

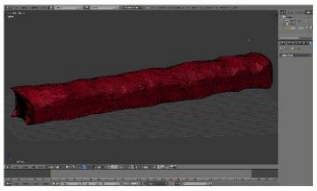

Geometria újraépítése CG programban

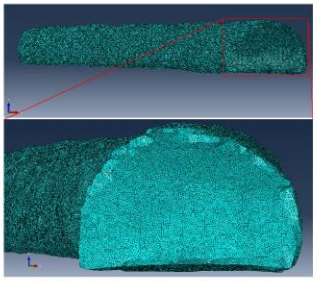

Numerikus modellező programban (ABAQUS) hálózott geometria

The Moiré Method and its Application in Scoliosis

Csaba Bogdán
University of Pécs – Faculty of Engineering and Information Technology, Pécs, Hungary

THE MOIRÉ METHOD AND ITS APPLICATION IN SCOLIOSIS

Csaba Bogdán

University of Pécs
Faculty of Engineering and Information Technology

Abstract

The diagnostic study of spinal deformities has long been a focus of medical science. For a clear condition assessment of scoliotic patients X-ray images are used. Disadvantages of X-ray inspections, however, make methodical research, which can lead to faster and cost-efficient examinations without the harmful radiation, reasonable.

HISTORY: In 1874, after LORD RAYLEIGH had studied the resultant pattern, the so-called moiré fringes of two overlapping grids, he concluded that the phenomenon could be useful for measurement purposes [1]. About a hundred years later further researches proposed moiré topography beyond industrial applications for measurement of the human body [2].

AIMS AND METHODS: The aim of this publication, based on thorough study of resources, is to present the basic theory of the moiré method and its application in scoliosis and to propose directions for further researches and developments.

The moiré phenomenon

The word moiré [mwaʁe] refers to an irregular, wavy surface whose pattern changes in accordance with its movement [3]. The moiré phenomenon becomes visible, for instance, if two structures with similar geometry overlap (e.g. wavy folds of lace curtain). In these cases a resultant pattern of light and dark fringes can be seen (Fig. 1). In general, the dark fringes are called moiré stripes [4, 5].

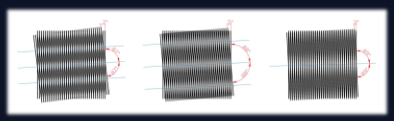

Fig. 1.
Moiré fringes of identical grids with different angle deviations

Shadow and projection moiré techniques

Moiré techniques, based on the physical phenomenon of moiré, are procedures usually used for surface and shape mapping or deformation measurement purposes [4, 6]. The main concept of moiré measurement is to associate a basic structure with the state of the examined body and another structure with its (deformed) state to be measured. From the moiré pattern created by these interacting structures we can conclude the differences between the two states of the body.

Moiré techniques differ in regards to the different ways the moiré pattern are created and processed. As for the shadow moiré technique, for example, the moiré phenomenon is created by the overlapping of a single reference grating and its own shadow projected onto the surface (Fig. 2). In the projection moiré technique two identical grids are used: one for projection and another for reference (Fig. 3).

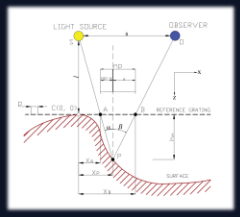

Fig. 2.
Optical arrangement of the shadow moiré technique

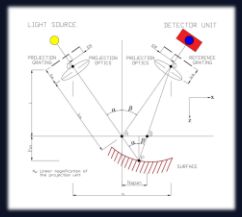

Fig. 3.
Optical arrangement of the projection moiré technique

Moiré method in scoliosis

In the diagnostics of scoliosis, the so-called Cobb angle measured on radiographs (Fig. 4) is considered the golden standard [7]. The angle value of spinal curvature measured on moiré images can be approximated to the Cobb angle. To evaluate moiré pictures, different measurement approaches can be used. A digital (projection) moiré technique presented by ANTAL et al. [8], for instance, used KAMAL's method to evaluate moiré images of scoliotic patients. To measure the two-dimensional curve angle of a single-curve scoliotic spine, KAMAL's approach [9, 10] considers points describing the most asymmetries on the back (Fig. 5).

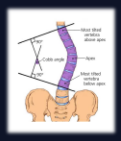

Fig. 4.
Measurement of Cobb angle [11]

$$\tan^{-1}\left(\frac{|d_1 - d_2|}{AC}\right) = \gamma_1 \qquad \tan^{-1}\left(\frac{|d_3 - d_4|}{BC}\right) = \gamma_2$$

$$d_1 = \frac{1}{2}(CH + CE) \qquad d_2 = \frac{1}{2}(AB + AG)$$

$$d_3 = \frac{1}{2}(BF + BI)$$

$$\theta = \tan^{-1}\left(\frac{|d_1 - d_2|}{AC}\right) + \tan^{-1}\left(\frac{|d_3 - d_4|}{BC}\right)$$

Fig. 5.
Measuring points and mathematical relationships of KAMAL's method [9]

The results of the evaluated moiré images of the trial group aged 9-17 years showed that the Cobb angle was well approximated in case of patients with thoracic curvature. Differences from Cobb values, however, in upper thoracic curvatures and lumbar curvatures were significant (10°-15°). The reason for this is down to the general characteristic of the scapula and the trunk's thick bundle of muscles covering the spine [8].

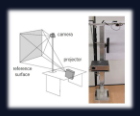

Fig. 6.
Digital moiré equipment: scheme and realization (transl. by auth.) [8]

Fig. 7.
Phases of producing digital moiré images [8]
From the left: normal image of the back - distorted image of the linear base grating - moiré image

Fig. 8.
Moiré and X-ray images of the same person [12]

Proposed directions for further research and development

1. Starting a dialogue for creating a methodological standard in diagnostics of scoliosis

For more precise interpretation of surface topographical methods, it is important to create a standard to body posture taken up during examinations [7].

2. Refine the algorithm for measuring scoliotic spine curvature

It can be done by rethinking or enhancing the mathematical-geometrical approach of KAMAL.

3. Detailed introducing of a well worked moiré equipment with how-to steps

The purpose is to bring the medical and engineer knowledge closer and encourage moiré researches in medical (orthopaedic) circles.

4. Improving communication between technical-biomedical experts and physicians

To the succesful application of moiré technique it is vital to have clear and unambiguous communication processes in interdisciplinary research groups.

Conclusion

The significant advantages of the moiré method are that it is fast, non-invasive, cost-efficient and has no harmful radiation. A moiré technique chosen and algorithmized well can be convenient to substitute or complement X-ray images in scoliosis. However, it is a significant limitation that a methodical standard which could lead to generally reliable results has been not created yet. Furthermore, the amount of labour required for the evaluation of moiré images is not inconsiderable [4, 13]. To achieve further success of the moiré method a dedicated partnership of engineers and physicians, respectively the application of technical-biomedical knowledge is needed.

References

[1] LORD RAYLEIGH *On the manufacture and theory of diffraction gratings*. Philosophical Magazine 47 (1874), 81-93, 193-205.
[2] TAKASAKI, H. *Moiré topography*. Applied Optics 1970;9(6):1467-72.
[3] CONWAY, A. *Moiré fringes on the factory floor*, New Scientist, 1972-06-22., 34.001, 692.
[4] POSTO, F.; GURGEL, J. L.; RUSSOMANO, T.; FARINATTI, P. T. V. *Moiré Topography: From Takasaki Till Present Day*. In: Theodoros B. Grivas (ed): *Recent advances in scoliosis*, Intech, 2012, 103-118.
[5] RÖSSLER, T.; HEJBOVSKÝ, M.; POCHMON, M. *Moiré methods for measurement for displacement and topography*. Czech J Phys, 2006, Vol 56(2), 101-216.
[6] LINO, A. C. L.; FABBRO, I. M. D. *Fruit profilometry based on shadow Moiré techniques*, Ciênc. Agrotec., 2004, Vol 28(1), 119-125.
[7] PATIAS, P.; GRIVAS, T. B.; KAPETIS, A.; AGGOURIS, C.; DEMAKOUTOS, E. *A review of the trunk surface metrics used as Scoliosis and other deformities evaluation indices*, Scoliosis, 2010, 5:12.
[8] ANTAL, A.; BALLA, P.; PECHMANN, K. *Digitális moiré képek szegélyes getinyfelületes hetegek egatom kimérésére*, Biomechanica Hungarica VII. (1), 50-60.
[9] KAMAL, S. *Measurement of Angle of Spinal Curvature by Moiré Topography*. Journal of Islamic Medical Association (USA), 1982, 14, 145-149.
[10] KAMAL, S. *Determination of degree of correction of spinal deformity by moiré topography. Moiré fringe topography and spinal deformity*, In: Deerup, B., Frobin, W., Hierholzer, E. (eds) *Proceedings of the 2nd. International Symposium. Sep. 12-15*, 1982 Münster, West Germany, Stuttgart: Gustav Fischer Verlag; 1983, 117-26.
[11] GREINER, K. *Adolescent idiopathic scoliosis: Radiologic decision-making*. American family physician, 2002, 65, 1817-22.
[12] KIM, H.; TAN, J.K.; ISHIKAWA, S.; SHINOMIYA, T. *Automatic detection of spinal deformity based on statistical features from the moire topographic images*, International Journal of Computing, 2009, Vol. 8(1), 72-78.
[13] ANTAL, A. *Optikai alon generált Moiréfelületek lokanalízise és identifikálása matematikai alkalmazásokkal*, PhD thesis, 2009, 25-26.

Bogdan.Csaba@mik.pte.hu

The First University in Hungary® 1367

ISBN 978-963-429-267-8

Pécs, 2018